國立臺灣大學工學院材料科學與工程學系暨研究所
碩士論文

Department of Materials Science and Engineering
College of Engineering
National Taiwan University
Master Thesis

運用ReaxFF力場模型探討原子尺度下鋰離子電池矽基負極鋰化動力學行為

Atomic-scale Modelling and Simulations of the Lithiation Behavior of the Si Anode in Li-ion Batteries using Reactive Force Field (ReaxFF)

潘立毅

Li-Yi Pan

指導教授：郭錦龍 博士

Advisor: Chin-Lung Kuo, Ph.D.

中華民國106年7月

July 2017

doi:10.6342/NTU201703940

doi:10.6342/NTU201703940

誌謝

本論文的撰寫，首先要感謝兩年間指導教授郭錦龍教授的指導，在思考問題上，常常能夠指出適當的方向，在學習解決問題的能力上讓我獲益良多。也感謝翰昕、鈺杰、奕廷、嘉澤等前輩們指導一些模擬條件上的修正，以及其他事務上的協助，使我能夠順利度過碩一的階段。在 7/24(一)交論文的前夕，感謝有仁願意一同修改論文到晚上 4 點半左右，一些論文英文表達上的問題在當時獲得修正。感謝子敬在這段時期的陪伴，稍微紓解了這段時間的壓力。在口試前一個禮拜的 7/21(一)~7/23(三)，也感謝張明揚、立揚與罔典犧牲休息時間的幫忙，特別是三天間張明揚的全力支援。本人由衷感謝這段時間實驗室同學們的幫助。希望同學們的研究，也能順利進行。

同時，也感謝這段時間內父母的支持，即使數據結果不理想，父母也告訴我盡力而為，不要有太大壓力，讓我能專心研究，在艱難的時刻，常常得到父母的鼓勵而能持續下去。也感謝口試委員趙聖德教授、許文東教授與郭哲來教授在 7/28(五)口試時，對論文的不足點上進行指正，使本論文能夠更臻完善。此外也感謝閒暇時刻朋友們聚會時的加油打氣，以及提供研究上的一些意見。儘管本次論文內容與結果不盡完美，也希望未來研究上能將之修正。最後謹在此對曾經獲得幫助的人，再次表達謝意。

doi:10.6342/NTU201703940

Contents

1 Introduction 13

1.1 Research Backgrounds 13

1.1.1 The Li-ion battery and the anode materials 13

1.1.2 The charging process of silicon anode in Li-ion battery 14

1.1.3 The silicon nanowire anode in Li-ion battery 15

1.2 Motivation and Objectives 15

2 Literature Review 17

2.1 The experimental observations 17

2.2 Kinetic and Thermodynamic issues 17

2.3 Studies about silicon lithiation issues by ReaxFF. 20

3 Methodology 31

3.1 Molecular Dynamics 31

3.2 Reactive Force Field (ReaxFF) 33

4 ReaxFF Parameter Validation 37

4.1 Computational Details 37

4.1.1 Structural Properties 37

4.1.2 Thermodynamic Properties 38

4.1.3 Mechanical Properties 39

4.1.4 Nudged Elastic Band Calculation of Li diffusion in crystalline Si 42

4.2 Structural Properties 44

4.3 Thermodynamical Properties 56

4.4 Mechanical Properties 62

4.5 Nudged Elastic Band calculation of lithium diffusion in crystalline silicon 64

4.6 Summary 65

5 Silicon lithiation rate comparison 67

5.1 Structure of silicon 67

5.2 Computational Details 69

5.3 Analysing Details 70

5.4 Results 72

5.4.1 Structural Observations in the Lithaition Mechanism 72

5.4.2 Lithiation Rates in Different Facets 77

5.4.3 Stress analysis in silicon slab 80

5.4.4 Lithiation Rates in Silicon Nanowires 80

5.4.5 Some Problems in this Study 86

5.4.6 Future Study 87

6 Conclusions 89

7 Appendix 91

7.1 Changes in order to make the energy volume curve smoother 91

7.2 The stress profile in the lithiation 92

8 References 99

doi:10.6342/NTU201703940

Figures

1.1 The schematics of rechargeabble Li-ion battery (adapted from Goodenough *et. al.*[2]) 13

2.1 The dumbbell-like shape formed in silicon nanowire lithaition (adopted from Liu *et al.*[5]) 22

2.2 The crack found in silicon nanowire lithaition (adopted from Liu *et al.*[5]) 22

2.3 The anisotropic expansion in silicon nanowire lithaition (adopted from Lee *et al.*[6]) 23

2.4 The phase boundary in silicon lithiation (adopted from Liu *et al.*[7]) 23

2.5 The ledge mechanism in silicon lithiation (adopted from Liu *et al.*[7]) 23

2.6 Chan *et al.*'s statement of the thermodynamic preference in silicon lithiation. The figure in the left shows the formation energy and the lithiation voltage. The figure in the right compares the lithation voltage. The lithiation voltage is prefered in Si(110) facet and therefore the more energy is released when lithiating the Si(110) facet than other facets. (adopted from Chan *et al.*[8]) 24

2.7 Jung *et al.*'s statement of the thermodynamic preference in silicon lithiation. The first figure shows the surface energy γ. The second figure shows the ratio of Li atoms to the interfacial Si(amorphous) atoms. The third figure shows the Li–Si(crystalline) bond to interfacial Si(amorphous)–Si(crystalline) bond ratio. The interface energy is prefered in Si(110) and therefore Si(110) is much stable than other facets. (adopted from Jung *et al.*[9]) 24

2.8 The energy barrier calculated by Cubuk *et al.*[10] 25

2.9 The kinetic Monte Carlo simulation of sililcon nanowire anisotropic expansion calculated by Cubuk *et al.*[10] 25
2.10 The shape of kinetic Monte Carlo simulation in sililcon nanowire anisotropic expansion calculated by Cubuk *et al.*[10] 26
2.11 The anisotropic lithiation mechanism by Rohrer *et al.*[11] 27
2.12 The slab lithaition performed by Kim *et al.* (adopted from Kim *et al.*[12]) 27
2.13 The ReaxFF nanowire lithaition in NVT 300 K. The anisotropy is reproduced. (adopted from Jung *et al.*[13]) 28
2.14 The stress analysis in ReaxFF nanowire lithaition (adopted from Jung *et al.*[13]) 28
2.15 The stress effect on the lithiation rate. (adopted from Ostadhossein *et al.*[14]) 29
2.16 The compressive stress effect on the Li diffusion energy barrier (adopted from Ding *et al.*[15]) 29
2.17 The vacancy effect on the lithiation rate (adopted from Kim *et al.*[16]) 30
3.1 The bond order function and the bond breaking behavior in ReaxFF 35
4.1 The illustration of the nudge elastic band method 43
4.2 The energy volume curve of c-Si 44
4.3 The energy volume curve of c-LiSi 44
4.4 The energy volume curve of c-Li$_{12}$Si$_7$ 45
4.5 The energy volume curve of c-Li$_{13}$Si$_4$ 45
4.6 The energy volume curve of c-Li$_{15}$Si$_4$ 46
4.7 The energy volume curve of c-Li$_{22}$Si$_5$ 46
4.8 The energy volume curve of c-Li 47

4.9 The radial distribution function of Li–Li in *a*-$Li_{32}Si_{32}$ 51

4.10 The radial distribution function of Li–Si in *a*-$Li_{32}Si_{32}$ 51

4.11 The radial distribution function of Si–Si in *a*-$Li_{32}Si_{32}$ 52

4.12 The radial distribution function of Li–Li in *a*-$Li_{40}Si_{24}$ 52

4.13 The radial distribution function of Li–Si in *a*-$Li_{40}Si_{24}$ 53

4.14 The radial distribution function of Si–Si in *a*-$Li_{40}Si_{24}$ 53

4.15 The radial distribution function of Li–Li in *a*-$Li_{50}Si_{14}$ 54

4.16 The radial distribution function of Li–Si in *a*-$Li_{50}Si_{14}$ 54

4.17 The radial distribution function of Si–Si in *a*-$Li_{50}Si_{14}$ 55

4.18 The pressure vs. volume curve comparison between ReaxFF and Stillinger Weber in NVT 1200 K 55

4.19 The formation energy of *c*-Li_xSi 57

4.20 The mixing energy of *c*-Li_xSi 58

4.21 The formation energy of *a*-Li_xSi 58

4.22 The mixing energy of *a*-Li_xSi 59

4.23 The formation energy comparison of amorphous and crystalline Li–Si alloys 59

4.24 The mixing energy comparison of amorphous and crystalline Li–Si alloys 60

4.25 The volume expansion of *a*-Li_xSi 60

4.26 The melting point of Si 61

4.27 The melting point of Li 61

4.28 The energy barrier of Li diffusion in Si by ReaxFF in this study 64

5.1 The silicon structure 67

5.2 The facets viewed along [110] 68

doi:10.6342/NTU201703940

5.3 The silicon and the lithium in all T_d site. The silicon is in ivory color while the lithium is in pink. The lithium should not be connected since there are no covalent bonding between them. The Li–Li connection is only used to show the duality of the silicon and lithium structure and the diffusion path of lithium in silicon. 68

5.4 The silicon with lithium slab used in this study 71

5.5 The lithiation in NVT 1000 K at 100 ps. 72

5.6 The RDF 800 K result 73

5.7 The RDF 1000 K result 74

5.8 The RDF 1200 K result 75

5.9 Kim's *et al.* result of RDF in lithiation 76

5.10 The temperature dependence on the lithiation rate difference 78

5.11 The anisotropy is reproduced in the Si[110] nanowire. The silicon is removed for clarity. The subfigure above shows the orignial settings while the subfigure below shows the nanowire after 72 ps. The anisotropy is reproduced. 82

5.12 The anisotropy is also reproduced in the Si[100] nanowire. The silicon is removed for clarity. The subfigure above shows the original settings while the subfigure below shows the nanowire after NVT 160 ps. The anisotropy is reproduced. 83

5.13 The Si[110] nanowire in NPT 600 K. The structure hardly lithiates. Si(110) has much larger phase boundary than other facets. 84

doi:10.6342/NTU201703940

5.14 The anisotropy is also reproduced in the Si[100] nanowire. The silicon is removed for clarity. The subfigure above shows the original settings while the subfigure below shows the nanowire after NPT 300 K 74.2 ps. with z-direction fixed and adding compressive stress on the *x*- and *y*-direction 85

7.1 The Si(100) maximum principal stress in NVT 800 K 93

7.2 The Si(110) maximum principal stress in NVT 800 K 93

7.3 The Si(111) maximum principal stress in NVT 800 K 94

7.4 The Si(112) maximum principal stress in NVT 800 K 94

7.5 The Si(100) maximum principal stress in NVT 1000K 95

7.6 The Si(110) maximum principal stress in NVT 1000K 95

7.7 The Si(111) maximum principal stress in NVT 1000K 96

7.8 The Si(112) maximum principal stress in NVT 1000K 96

7.9 The Si(100) maximum principal stress in NVT 1200K 97

7.10 The Si(110) maximum principal stress in NVT 1200K 97

7.11 The Si(111) maximum principal stress in NVT 1200K 98

7.12 The Si(112) maximum principal stress in NVT 1200K 98

doi:10.6342/NTU201703940

國立臺灣大學 · 愛國愛人 · 敦品勵學

doi:10.6342/NTU201703940

Tables

2.1 The thickness of phase boundary and the lithiation velocity in each facets 20

4.1 The lattice constant of Li, Si and their alloys 48

4.2 The comparison of ReaxFF and Bader charge of Li in crystalline Li–Si alloy (unit: e) 48

4.3 The comparison of ReaxFF and Bader charge of Li in amorphous Li–Si alloy (unit: e) 49

4.4 The cutoff radius used in the coordination number determiniation 49

4.5 The coordination number of a-$Li_{32}Si_{32}$, a-$Li_{40}Si_{24}$ and a-$Li_{50}Si_{14}$ 50

4.6 The comparison of ReaxFF formation energy with Fan *et al.*'s data and DFT data. (unt: kcal/mol) 56

4.7 The calculated stiffness tensor in silicon (unit: GPa) 62

4.8 The mechanical properties of *c*-Si (unit: GPa) 62

4.9 The mechanical properties of *c*-Li (unit: GPa) 63

4.10 The mechanical properties of *c*-LiSi (unit: GPa) 63

4.11 The mechanical properties of c-$Li_{15}Si_4$ (unit: GPa) 63

5.1 Dimensions of the Si slab used in this simulation (20 Å vacuum layer for surface structure simulation is excluded from the table) 69

5.2 Dimensions of the Li slab used in this simulation 69

5.3 The NVT lithation rate comparison (unit: Å/ns) 77

5.4 The NVT phase boundary thickness comparison (unit: Å) 78

doi:10.6342/NTU201703940

Abstract

Li-ion battery is important in energy storages application such as portable electronic devices or electric cars. In most of Li-ion batteries, the anode material is graphite. Some researchers have found that the Si anode has a specific capacity approximately 10-fold larger than graphite. Therefore, it is deemed as a promising anode material. However, it suffers from the fracture problem in charging, due to the anisotropic expansion. This will strongly hinders the performance and cyclability. In this thesis, we will study the lithiation mechanism of Si anode by Reactive Force Field (ReaxFF) molecular dynamics simulations. We have performed the silicon slab lithiation to observe the lithiation behavior at different temperature, and we have reproduced some anisotropy in this case. On the other hand, we have also performed the nanowire lithiation to show the anisotropic expansion. Our results show that the lithiation behavior is mainly kinetic controlled rather than thermodynamic controlled. We suggest that it is the lithium insertion preference in the Si(110) facets that leads to the anisotropic expansion. We have also analyzed the stress developed in the silicon. There are still some problems in the simulations, such as the energy discontinuity and the anomalous lattice constant at high temperature in ReaxFF, and some of which are still under investigation. In the future study, we will perform the simulation at lower temperature and higher lithium concentration to fully reproduce the anisotropic lithiation behavior.

摘要

鋰電池為現今重要的能量儲存裝置，並且被廣泛運用於可攜帶電子裝置、電動車等。目前大部分的商業用鋰電池負極材料使用的是石墨。然而，研究人員發現以矽作為負極材料的鋰電池擁有石墨電極約10倍的單位(重量)電容量。因此被視為鋰電池負極材料的明日之星。然而，矽負極的充電會造成矽的破裂，這主要是由矽負極的不等向膨脹所引起。矽的破裂將嚴重影響鋰電池的表現與可循環使用性。本研究將探討矽負極材料的鋰化機制，我們將使用 Reactive Force Field (ReaxFF)的分子動力學模擬探討此問題。我們計算並觀察矽的平板在不同溫度下的鋰化行為，我們部分複製了在實驗中觀察到的不等向膨脹。除此之外，我們也使用了奈米線鋰化並觀察到非等向膨脹。由計算結果我們認為是動力學主導了不等向膨脹的問題。我們認為鋰在Si(110)方向的高擴散速度是此不等向膨脹的主因。我們分析了在鋰化過程中矽所產生的應力。本次模擬仍有一些問題，包括了 ReaxFF 在能量上的斷點、以及在高溫下不尋常的晶格常數等問題，其中有部分我們仍舊需要找出癥結點。在未來研究中，我們將會在低溫且高鋰濃度下進行鋰化，以完整複製實驗結果觀察到的非等向膨脹。

CHAPTER 1 Introduction

1.1 Research Backgrounds

1.1.1 The Li-ion battery and the anode materials

Rechargeable Li-ion battery has been introduced in 1980[1] and it has been commercialized in 1991. It has been widely used in portable devices or electric cars. As in a normal battery system, it has 3 major parts: **anode**, **cathode** and **electrolytes**.

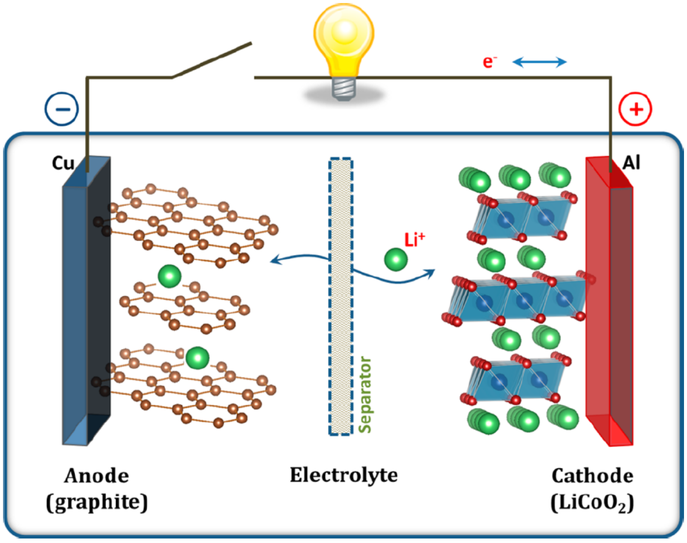

Figure 1.1 The schematics of rechargeabble Li-ion battery (adapted from Goodenough *et. al.*[2])

In Li-ion battery, the *anode* (*negative* electrode) material undergoes an *oxidation* reaction (loss electron) while the *cathode* (*positive* electrode) material undergoes an *reduction* reaction (gain electron) during *discharging* process. The *charging process* is its counter-reaction and the oxidation-reduction relation is reversed.

The modern rechargeable Li-ion battery utilizes a **graphite anode**, **lithium cobalt oxide cathode** and **$LiPF_6$ salt as electrolyte in ethylene carbonate** (**EC**) **solvent**. The chemical reaction during *charging* can be written as below:

doi:10.6342/NTU201703940

- Cathode

$$\mathrm{LiCoO_2} \rightarrow \mathrm{Li}_{1-x}\mathrm{CoO}_x + xe^- + x\mathrm{Li}^+$$

- Anode (Graphite) : intercalating reaction

$$\mathrm{C} + xe^- + x\mathrm{Li}^+ \rightarrow \mathrm{Li}_x\mathrm{C}$$

for $0 \leq x \leq 1/6$

However, it was found that the **silicon anode** can have a better capacity.[3] Its reaction can be written as below

- Anode (Silicon) : alloying reaction

$$\mathrm{Si} + xe^- + x\mathrm{Li}^+ \rightarrow \mathrm{Li}_x\mathrm{Si}$$

for $0 \leq x \leq 3.75$

One can calculate that the theoretical energy capacity of graphite anode is 372.24 mAh/g while it is 3579.80 mAh/g for silicon anode.[3] Therefore, silicon is a promising anode material in future Li-ion battery and has been widely researched. In this study, we will focus on the silicon anode and its properties during charging.

1.1.2 The charging process of silicon anode in Li-ion battery

The charging process of Li intercalation in graphite anode has been illustrated in figure **1.1**. The Li ion was inserted into the interspacing of graphite. The silicon anode does not store lithium by *intercalating* but *alloying* mechanism. The main difference is that the Si–Si bond will be broken during the charging process, while this is not the case for graphite anode. This process is called the *lithiation* of silicon anode.

The lithiation of silicon releases energy. The silicon will be lithiated to amorphous Li–Si alloy (a-$\mathrm{Li_xSi}$) and have a maximum $x = 3.75$. Despite its high specific capacity, the silicon battery suffers from serious volume expansion problem as 400% expansion during lithiation. This will make the silicon anode vulnerable to break and pulverize into smaller particle. This leads to the capacity fading in Li-ion battery.

1.1.3 The silicon nanowire anode in Li-ion battery

In order to solve the problem of volume expansion. Chan *et al.* have proposed the **silicon nanowire anode**[4] in Li-ion battery. They have achieved better cyclability than the thin-film or nanoparticle counterparts. However, some cracks are still found in the nanowire. This will be explained in the literature review part. The anisotropic expansion in silicon nanowire, particularly in Si[110] direction, makes the Li–Si alloy surface under large tensile stress and cracks the nanowire.

1.2 Motivation and Objectives

In this study, we want to characterize the reason why the silicon nanowire undergoes the anisotropic lithiation. We want to find out if it is the *thermodynamic* or *kinetic* issues that caused the anisotropy. We will use the Reactive Force Field (ReaxFF) in our study. We will compare the lithiation rate of different facets in silicon. The temperature contribution to the lithiation rate will be discussed. Besides, the anisotropic expansion of silicon nanowire will be illustrated.

doi:10.6342/NTU201703940

CHAPTER 2 Literature Review

2.1 The experimental observations

The anisotropic expansion in silicon nanowire lithiation has been observed experimentally by many groups. Liu *et al.* have observed dumbbell-shaped cross section (figure **2.1**) in silicon nanowire lithiation.[5] Besides, the crack is also observed in the center of the nanowire, shown in figure **2.2**.

Besides, Lee *et al.* have performed the lithiation of silicon nanopillars[6] with orientation of $\langle 100 \rangle$, $\langle 110 \rangle$ and $\langle 111 \rangle$ and observed that the Si(110) has much higher lithiation rate than Si(100) and Si(111). The result is shown in figure **2.3**. All of their observations shows a higher lithiation rate in Si(110) than other facets.

In addition, Liu *et al.* have conducted an *in situ* imaging[7] of the lithiation of silicon nanowire. In their study, they have reported a *comparable* lithiation rate between Si(110) facet and Si(112) facet. They have also observed the lithiation front (figure **2.4**) during an *in-situ* TEM obsrvation. The Si(112) facet have a clear reaction front while Si(110) 's is blur. It was shown in the supporting information of the paper. A ledge mechanism is proposed to explain the lithiation in Si(112) facet. These results are shown in figure **2.5**.

2.2 Kinetic and Thermodynamic issues

It has been a long debate for the lithiation anisotropy is a *thermodynamic* or *kinetic* driven process. In the following section, some of the points will be reviewed.

Thermodynamic issues about the lithiation anisotropy

Chan *et al.* have conducted an *ab initio* calculation[8] to check if the anisotropic expansion in silicon lithiation is a *thermodynamically driven* process. *i.e.* it is energetically favorable for lithiation in Si(110) facets than any other one. They performed a lithium insertion algorithm in the tetrahedral site of silicon and check for its changes. After that, they calculated the formation energy and the lithiation voltage (figure **2.6**) of the Li–Si alloy formed in Si(100), Si(110) and Si(111) and concluded that Si(110) has a higher voltage and therefore higher energy preference in lithiation.

Jung *et al.* have also conducted an *ab initio* calculation[9] for the *a*-Li_xSi/*c*-Si surface and calculated the interface energy for Si(100), Si(110) and Si(111). The surface energy is defined as

$$\gamma = (E_{tot} - E_{a-Li_xSi} - E_{c-Si})/(2A) \tag{2.1}$$

The surface energy and surface Li/Si concentration results are shown in figure **2.7**. They have arrived at 2 results:

1. The Si(110) has the lowest surface energy among all facets at $x = 3.4$ in *a*-Li_xSi.
2. The Li surface concentration is the highest in Si(110) facets.

Therefore the energy stability of the lithiation in Si(110) is confirmed. Besides, the high lithium concentration will also enhance the lithiation rate.

Kinetic issues about the lithiation anisotropy

Cubuk *et al.* have conducted another *ab initio* calculation[10] to check the orientation dependence on the energy barrier (figure **2.8**). After obtaining the energy barrier, they performed the kinetic Monte Carlo simulation to calculate the shape evolution. It is concluded that the Li will tend to concentrate in the *surface layer* in Si(110) facet, while Li will go into the *deeper layer* in Si(111) facet by comparing the energy barrier difference. The concentration and lithiation rate are shown in figure **2.9**. The anisotropy can be reproduced (figure **2.10**) and therefore the energy barrier dependence of the lithiation rate is confirmed.

doi:10.6342/NTU201703940

Rohrer *et al.* have also conducted an *ab initio* calculation on the lithiation process[11]. They have calculated the *energy preference* (shown as below, the higher the more energetically preferred) for *each lithiation step* in different facets.

- Li adsorption on c-Si: (100) < (111) < (110).
- Li (clean) penetration into c-Si: (100) < (110) < (111).
- Li (full-Li covered) penetration into *c*-Si: (111) $\doteqdot$ (100) < (110).
- Surface energy preference of *a*-Li_2Si/*c*-Si: (110) < (100) < (111).
- Energy barrier preference of Li (full-Li) diffuse into *c*-Si: isotropic.
- Energy barrier preference of Li (*a*-Li_2Si) diffuse into *c*-Si: isotropic.
- Nucleus formation (*a*-Li_xSi formation in Si) energy preference: (100) < (111) < (110).

In addition to the different concentration of Li–Si alloy (*a*-Li_2Si/c-Si) are used from Jung *et al.*'s paper(*a*-$Li_{3.57}Si$/c-Si). The paper have mentioned a complete different viewpoint about the surface energy preference with Jung's statement[9]. They argued that the facet with the *lowest* surface energy will be the most stable facet and will be *harder* to move. Therefore, when focusing on the nucleus formation preference term, the Si(110) has the highest nucleus formation energy. Thus the Si(110) is preferred than other facets. The illustration is shown in figure **2.11**.

Therefore, we want to clarify whether the thermodynamic issue, which is the energy preference of the *product* and the *reactant*, or kinetic issues, which is the energy barrier *between* the product and the reactant, are more important in the lithiation process. Understanding this lithiation mechanism will be helpful in further study to slow down the lithiation rate and therefore preventing from the cracking in *a*-Li_xSi shell.

2.3 Studies about silicon lithiation issues by ReaxFF.

Kim *et al.* have performed the molecular dynamic (MD) simulations[12] to check if the lithiation anisotropy can be reproduced. They used the reactive force field (ReaxFF) and Si(100), Si(110) and Si(111) slab with plenty of Li above it for lithiation. The simulation is carried out in **1200 K** and the results are shown in figure **2.12**. They have observed the phase boundary in the simulation and comfirmed its structure as *c*-LiSi (not exactly, however). The calculated velocity is also shown in table **2.1**. They multiplied the layer density and the lithiation rate and concluded that Si(110) has the highest lithiation rate. This weighted lithiation rate for Si(100), Si(110) and Si(111) are 1.0, 1.52 and 1.27 respectively in their study (normalized by Si(100)).

samples	thickness (nm)	velocity (nm/ps)	atom density (atoms/nm^2)
a-Si	-	15.5	-
Si(100)	1.61	8.8	6.87
Si(110)	1.23	9.47	9.59
Si(111)	0.59	9.7	7.83

Table 2.1 The thickness of phase boundary and the lithiation velocity in each facets

Jung *et al.* have performed another ReaxFF-MD simulation for the lithiation of silicon nanowire.[13] They used 2 nanowire with Si(100) and Si(110) facets and Li surrounded for lithiation. The lithiation is carried out in **NVT 300 K** and the anisotropy is reproduced (figure **2.13**). The anisotropy that they reproduced is more obvious than Kim *et al.*'s. They also performed the stress analysis (figure **2.14**) and confirmed that the phase boundary layer is under compressive stress and the lithiated silicon layer is under tensile stress. However,

doi:10.6342/NTU201703940

the stress is somehow very large and I suspected that the volume is not divided in the raw data of LAMMPS, which output stress in the unit of stress·volume.

Ostadhossein *et al.* have also performed an ReaxFF-MD simulation[14] to check the stress dependence of the lithiation rate. They used the Si(112) facet (the same as Liu *et al.* mentioned previously[7]) and performed the lithiation in **NVT 600 K**. The ledge mechanism of the Si peeling off as in Liu *et al.*'s study is again observed. Besides, They have also observed that a compressive stress is developed near the phase boundary and concluded that a compressive stress of 4.5 GPa can stop the lithiation. They have performed another NPT simulation with compressive stress of 1 to 3 GPa on Si(110) facet to show that a compressive stress can slow down the lithiation rate. (figure **2.15**)

Just recently, Ding *et al.* have performed an ReaxFF simulation[15] to check the stress dependence of the Li diffusion energy barrier. They used nudged elastic band (NEB) to show that the diffusion energy barrier can be harder to overcome due to the compressive stress (figure **2.16**).

While in terms of vacancy influence. Kim *et al.* have also performed ReaxFF-MD simulation[16] in **NVT 900–1500 K** to check the vacancy influence in the lithiation rate. They have concluded that the introducing of Si vacancy accelerates the lithiation rate (figure **2.17**). It therefore suggested that the breaking of Si–Si bond is the rate-limiting factor in the lithiation of silicon anode.

Summarizing the studies above, we have known that

- These studies are done in various temperature ranging from 300 K to 1200 K. The temperature dependence of the lithaition rate is another unsolved problem in the silicon lithiation.
- A lower temperature as in Jung *et al.*[13] NVT 300 K can reproduce the anisotropy better

doi:10.6342/NTU201703940

than 1200 K as in Kim *et al.*'s[12].

- Compressive stress can have a suppressing effect on the lithiation rate in 600 K as mentioned by Ostadhossein *et al.*[14]. It was further explained by calculating the Li diffusion barrier as in Ding *et al.*'s paper.[15]
- A different lithiation mechanism is observed in 900–1500 K by Kim *et al.*[16] which states that the Si–Si bond breaking is the rate-limiting factor.

Therefore, we want to characterize the effect of temperature in this study.

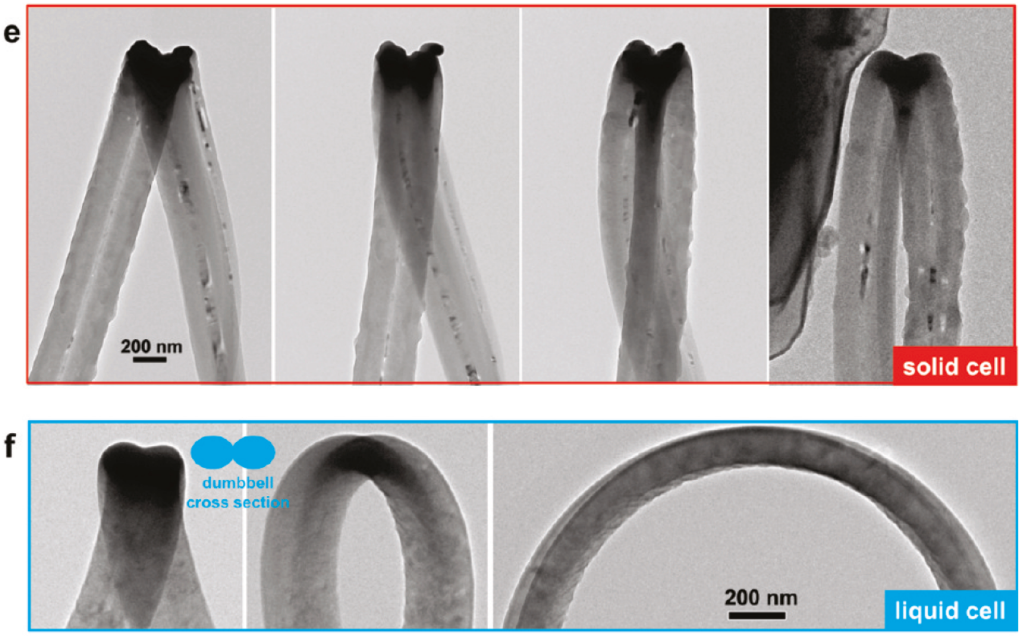
e
200 nm
solid cell
f
dumbbell
cross section
200 nm
liquid cell

Figure 2.1 The dumbbell-like shape formed in silicon nanowire lithaition (adopted from Liu *et al.*[5])

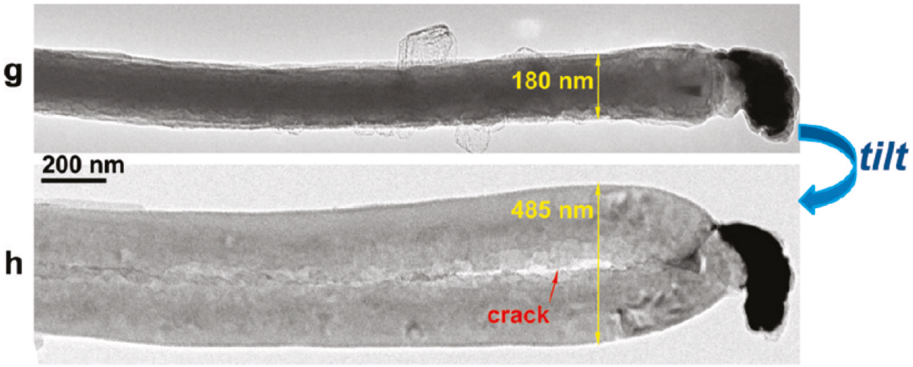
g
180 nm
200 nm
tilt
485 nm
h
crack

Figure 2.2 The crack found in silicon nanowire lithaition (adopted from Liu *et al.*[5])

doi:10.6342/NTU201703940

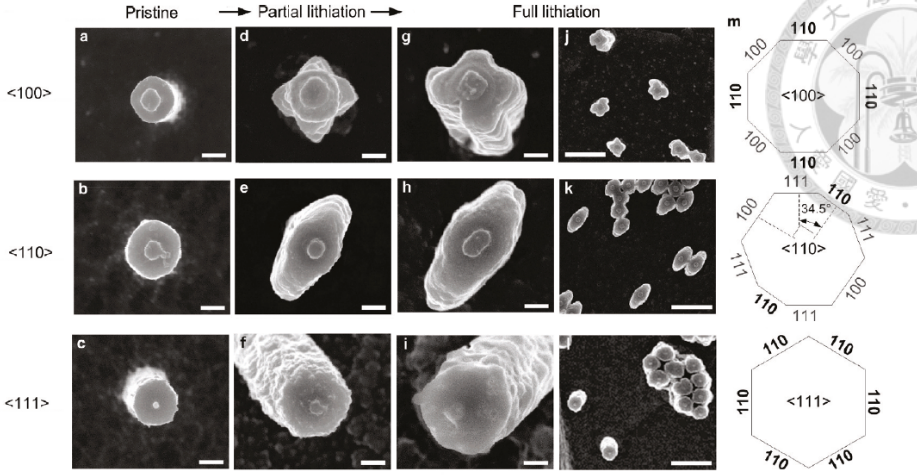
Pristine
Partial lithiation
Full lithiation
<100>
<110>
<111>
a
b
c
d
e
f
g
h
i
j
k
l
m
110
100
<100>
111
34.5°
<110>
<111>

Figure 2.3 The anisotropic expansion in silicon nanowire lithaition (adopted from Lee *et al.*[6])

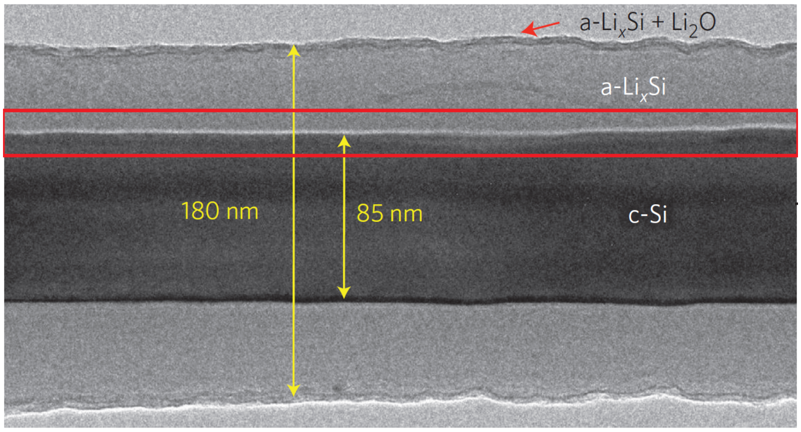
a-Li_xSi + Li_2O
a-Li_xSi
180 nm
85 nm
c-Si

Figure 2.4 The phase boundary in silicon lithiation (adopted from Liu *et al.*[7])

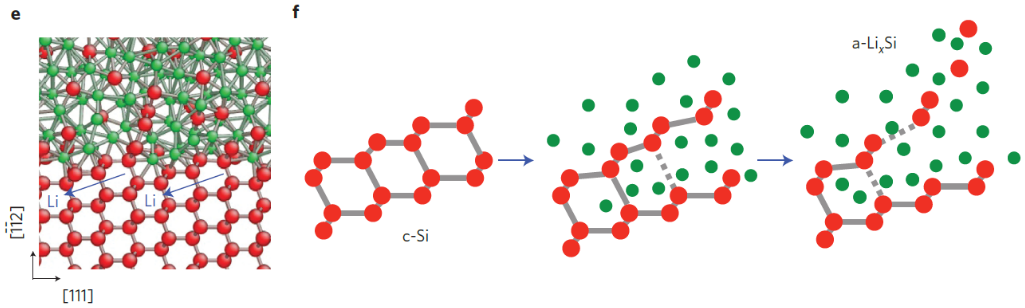
e
f
Li
Li
[$\bar{1}\bar{1}2$]
[111]
c-Si
a-Li_xSi

Figure 2.5 The ledge mechanism in silicon lithiation (adopted from Liu *et al.*[7])

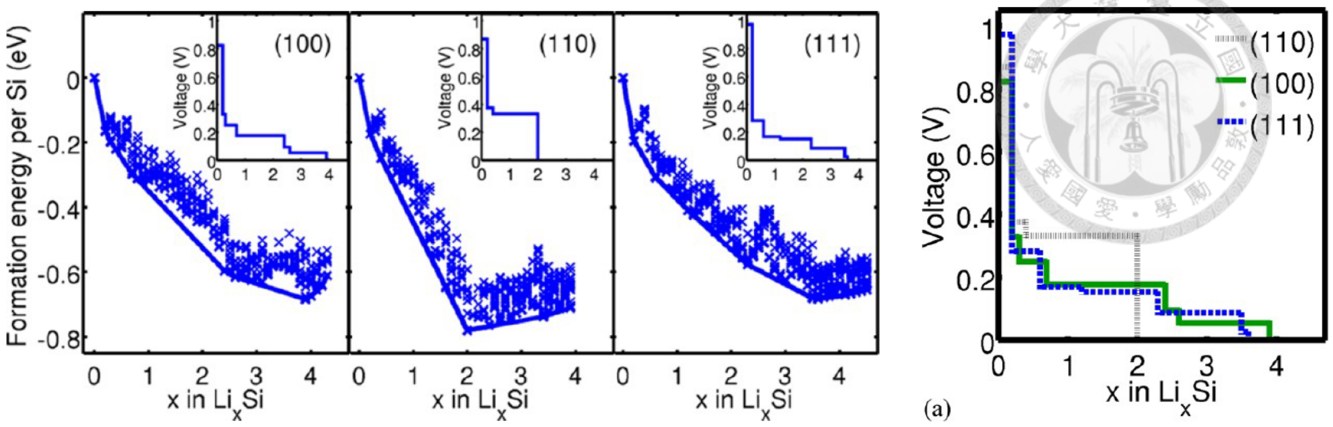

Figure 2.6 Chan *et al.*'s statement of the thermodynamic preference in silicon lithiation. The figure in the left shows the formation energy and the lithiation voltage. The figure in the right compares the lithation voltage. The lithiation voltage is prefered in Si(110) facet and therefore the more energy is released when lithiating the Si(110) facet than other facets. (adopted from Chan *et al.*[8])

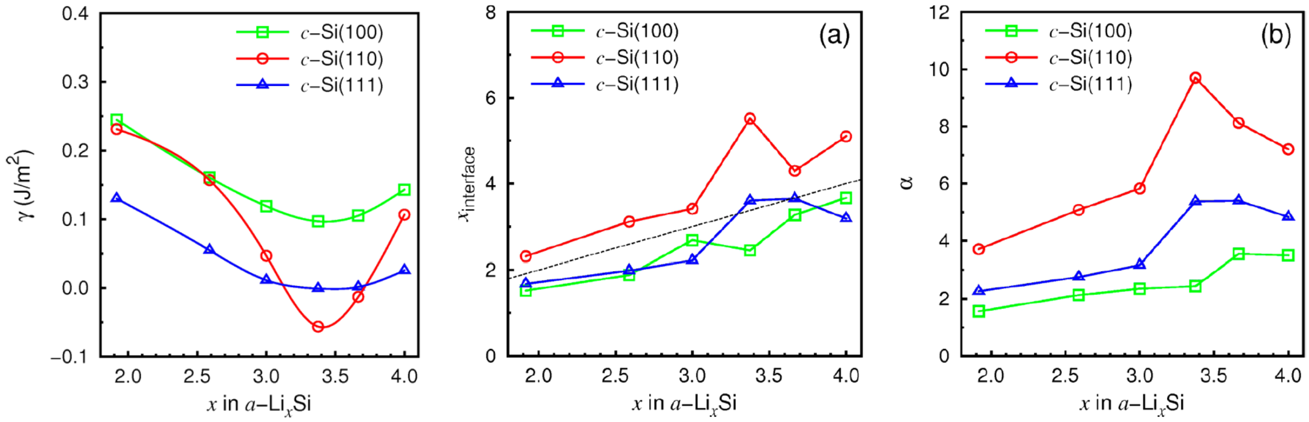

Figure 2.7 Jung *et al.*'s statement of the thermodynamic preference in silicon lithiation. The first figure shows the surface energy γ. The second figure shows the ratio of Li atoms to the interfacial Si(amorphous) atoms. The third figure shows the Li–Si(crystalline) bond to interfacial Si(amorphous)–Si(crystalline) bond ratio. The interface energy is prefered in Si(110) and therefore Si(110) is much stable than other facets. (adopted from Jung *et al.*[9])

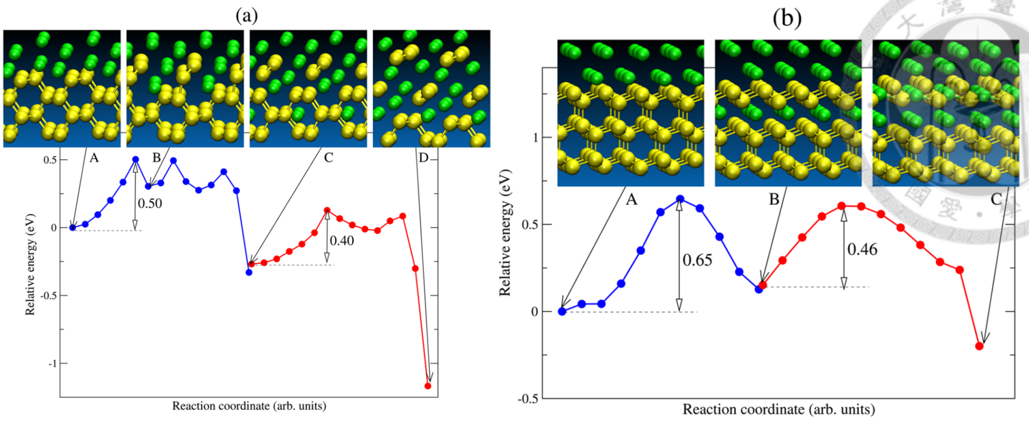

Figure 2.8 The energy barrier calculated by Cubuk *et al.*[10]

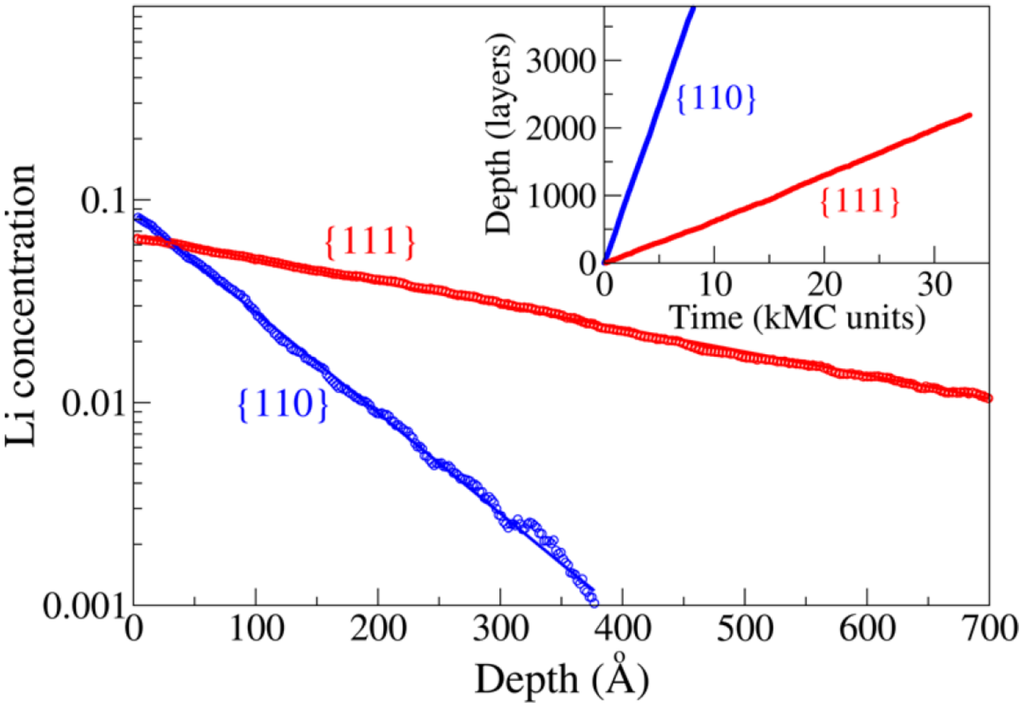

Figure 2.9 The kinetic Monte Carlo simulation of sililcon nanowire anisotropic expansion calculated by Cubuk *et al.*[10]

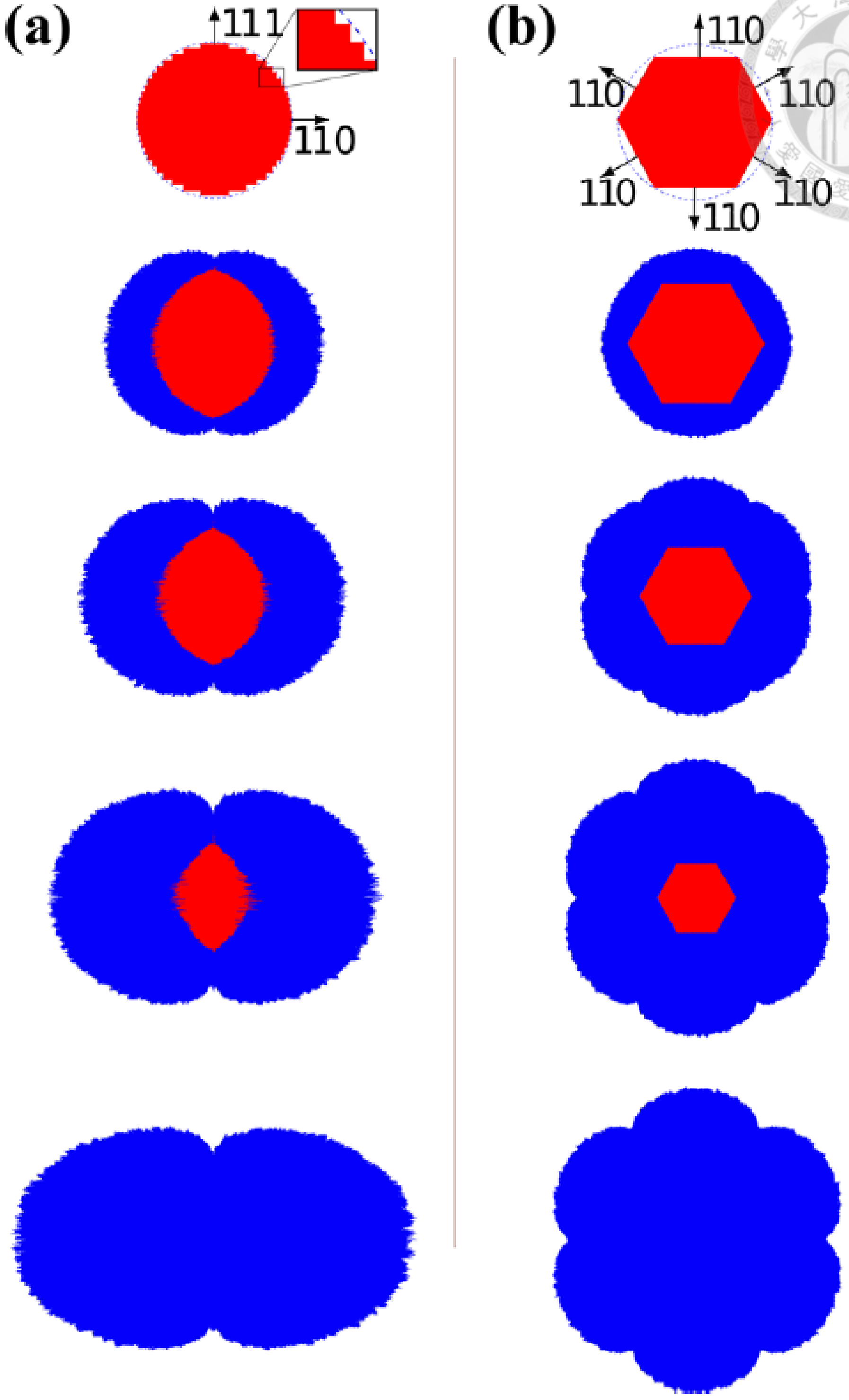
(a)
111
1̄10
(b)
110
110
110
1̄10
1̄10
110

Figure 2.10 The shape of kinetic Monte Carlo simulation in silicon nanowire anisotropic expansion calculated by Cubuk *et al.*[10]

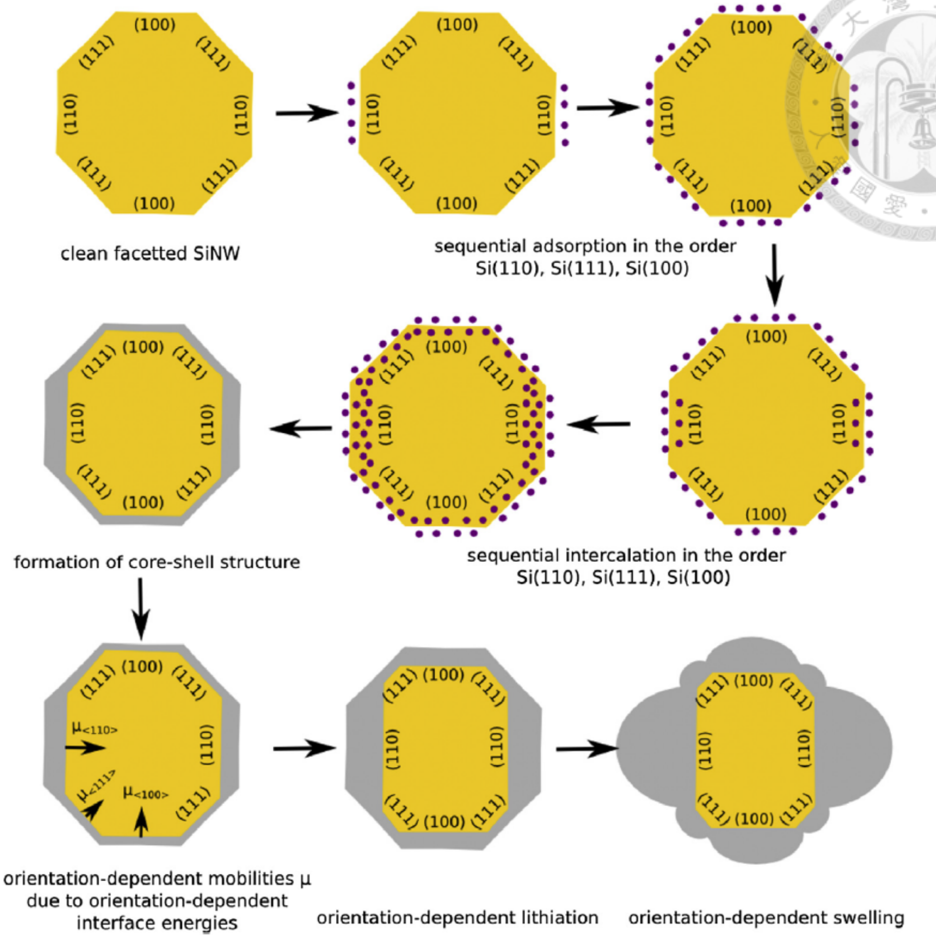
(100)
(111)
(110)
clean facetted SiNW
sequential adsorption in the order
Si(110), Si(111), Si(100)
formation of core-shell structure
sequential intercalation in the order
Si(110), Si(111), Si(100)
μ<110>
μ<111>
μ<100>
orientation-dependent mobilities μ
due to orientation-dependent
interface energies
orientation-dependent lithiation
orientation-dependent swelling

Figure 2.11 The anisotropic lithiation mechanism by Rohrer *et al.*[11]

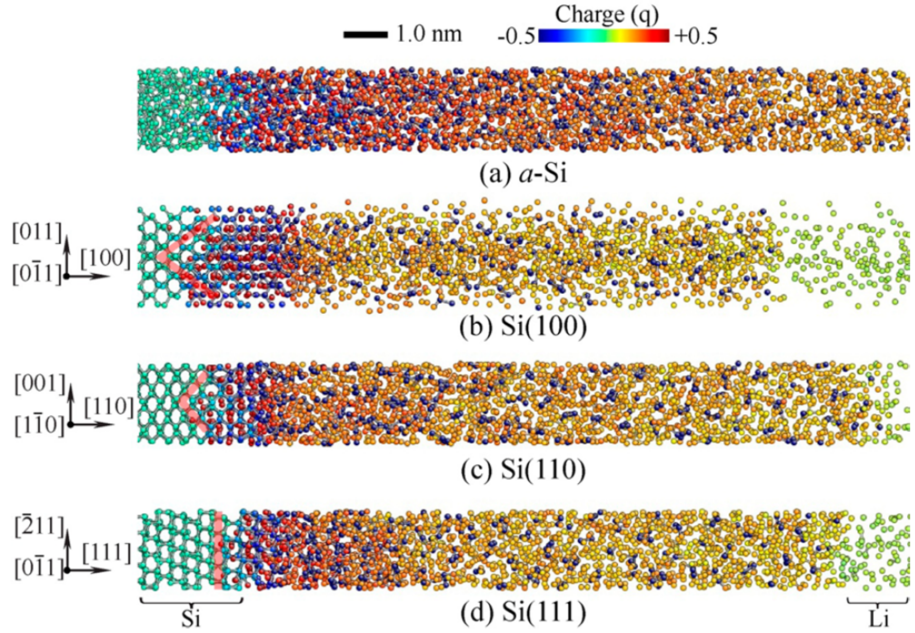
1.0 nm
Charge (q)
-0.5
+0.5
(a) a-Si
[011]
[0$\bar{1}$1]
[100]
(b) Si(100)
[001]
[1$\bar{1}$0]
[110]
(c) Si(110)
[$\bar{2}$11]
[0$\bar{1}$1]
[111]
(d) Si(111)
Si
Li

Figure 2.12 The slab lithaition performed by Kim *et al.* (adopted from Kim *et al.*[12])

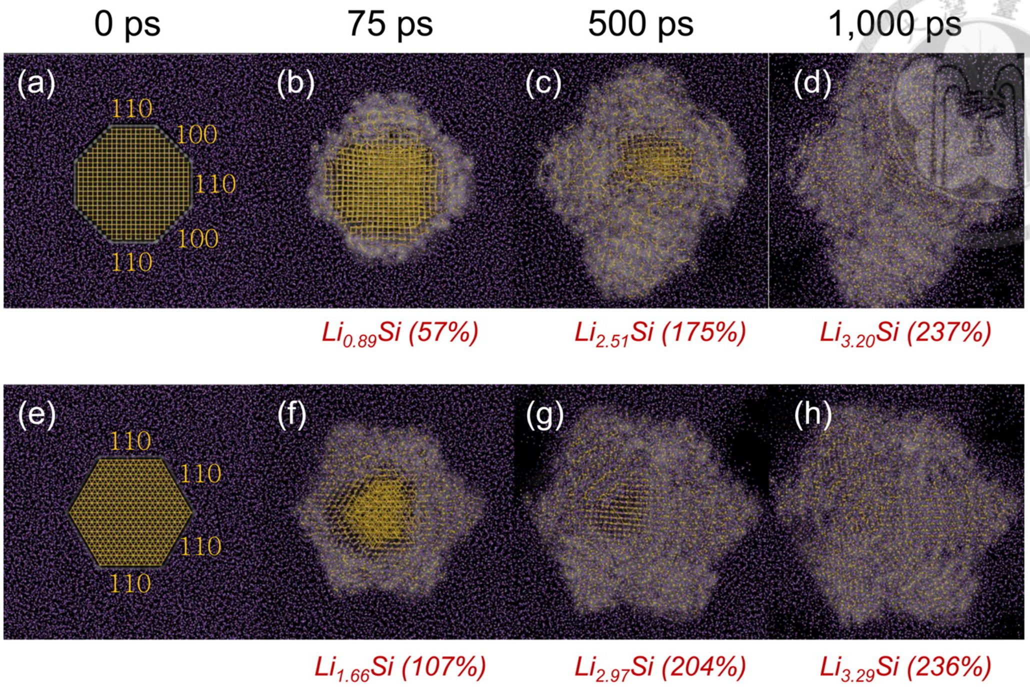
0 ps
75 ps
500 ps
1,000 ps
(a)
110
100
110
100
110
(b)
(c)
(d)
Li0.89Si (57%)
Li2.51Si (175%)
Li3.20Si (237%)
(e)
110
110
110
110
(f)
(g)
(h)
Li1.66Si (107%)
Li2.97Si (204%)
Li3.29Si (236%)

Figure 2.13 The ReaxFF nanowire lithaition in NVT 300 K.

The anisotropy is reproduced. (adopted from Jung *et al.*[13])

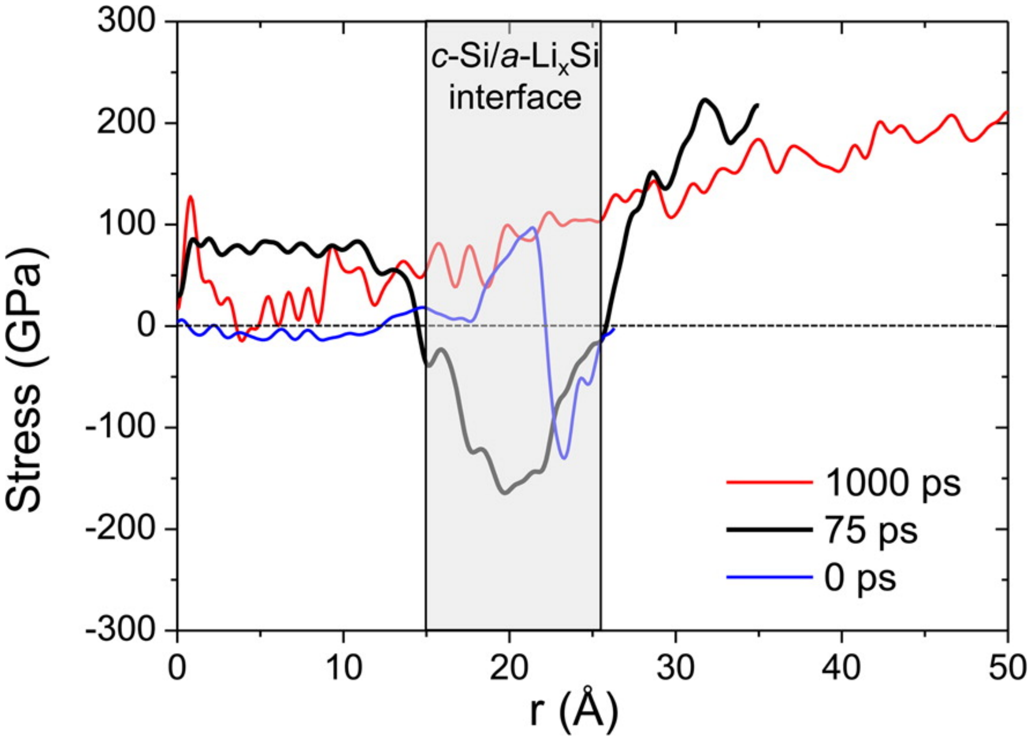

Figure 2.14 The stress analysis in ReaxFF nanowire lithaition (adopted from Jung *et al.*[13])

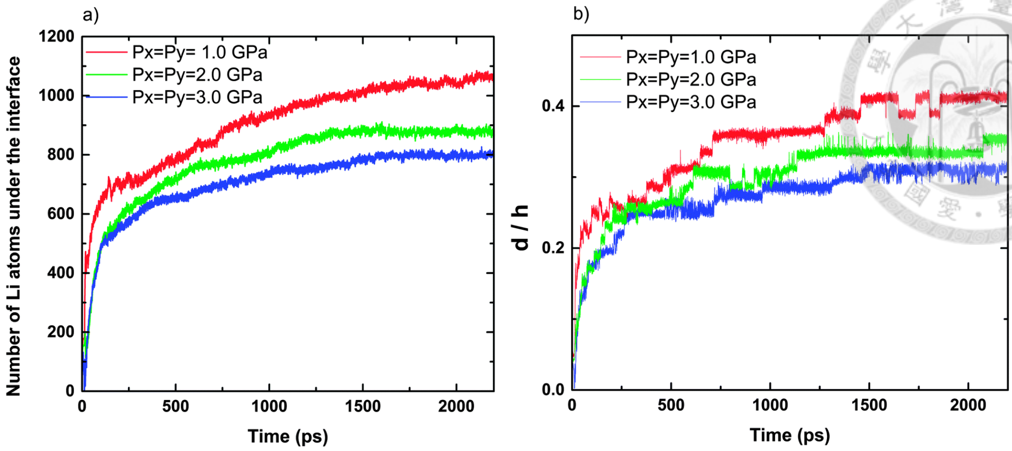

Figure 2.15 The stress effect on the lithiation rate. (adopted from Ostadhossein *et al.*[14])

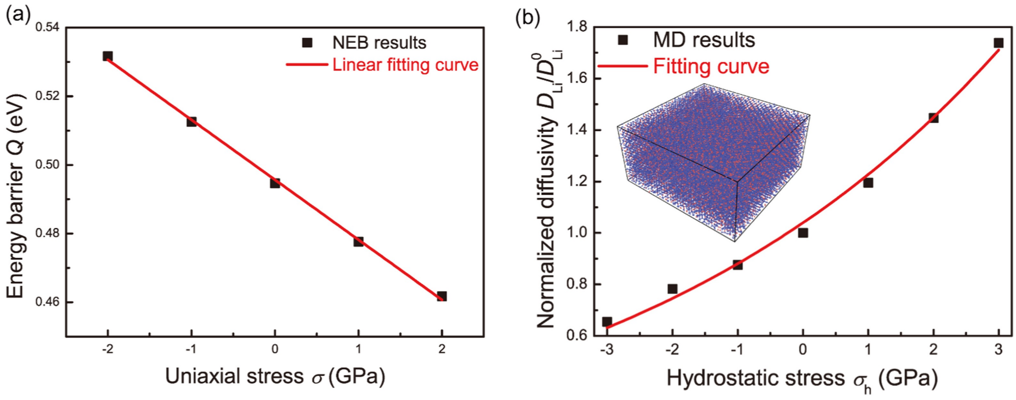

Figure 2.16 The compressive stress effect on the Li diffusion energy barrier (adopted from Ding *et al.*[15])

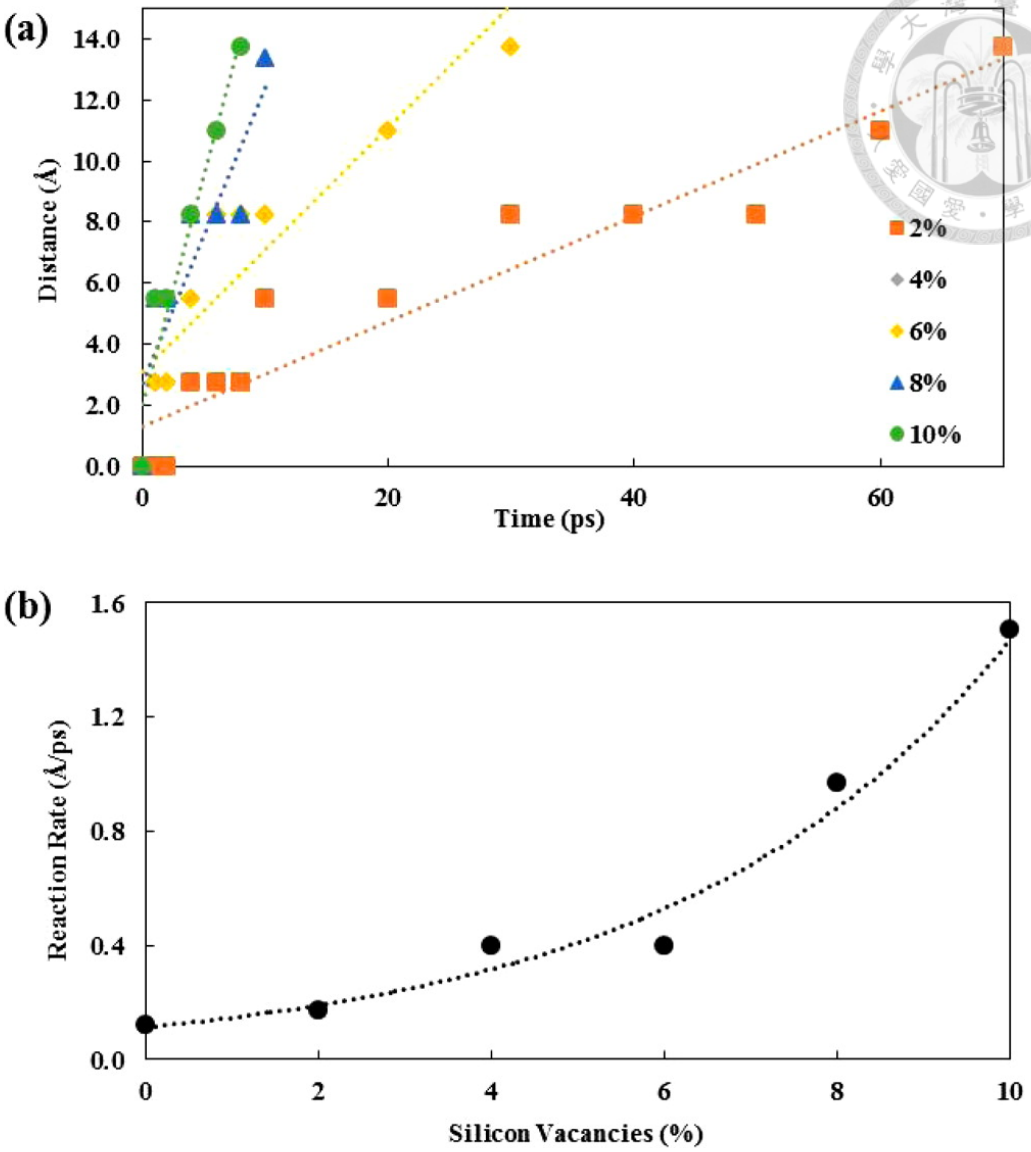

Figure 2.17 The vacancy effect on the lithiation rate (adopted from Kim *et al.*[16])

CHAPTER 3 Methodology

3.1 Molecular Dynamics

In this study, we used the **molecular dynamics** with the **Reactive Force Field** (ReaxFF) implemented in LAMMPS to study the Si lithiation problem. The molecular dynamics simulation predicts the atomic movement by solving the Newton's equation of motion by time integration. *i.e.* if there are n atoms in the system and for each atom i, for all $1 \leqq i \leqq n$, we have.

$$\mathbf{F}_i(t) = m_i \frac{\mathrm{d}^2 \mathbf{x}_i(t)}{\mathrm{d}t^2} \tag{3.1}$$

while

$\mathbf{F}_i(t)$ = The force vector imposed on atom i at time t

m_i = The atomic mass of atom i

$\mathbf{x}_i(t)$ = The position vector of atom i at time t

Therefore, if the initial position $\mathbf{x}_i(t)$ and the force $\mathbf{F}_i(t)$ is given, the moving trajectory can be calculated. The **classical molecular dynamics**, which utilizes a **force field**, is adopted in this study. This means that the potential energy surface

$$V = V(\mathbf{x}_1, \mathbf{x}_2, ..., \mathbf{x}_n) \tag{3.2}$$

is given by an **empirical formula** and the force imposed on atom i can be calculated by

$$\mathbf{F}_i = -\nabla_i V \tag{3.3}$$

In order to solve the equation of motion **(3.1)**, the **initial velocity and position** must be given. This is done by giving a random velocity with their absolute value in Gaussian distribution for each atom.

While the acceleration (solved by force) $\ddot{\mathbf{x}}$, velocity $\dot{\mathbf{x}}$ and position $\mathbf{x}$ of each atom (from now on, we dropped the i in each atom for simplicity) are given, the problem remains is to solve the differential equation **(3.1)** by time integration. There are many ways to solve this initial value problem but the **velocity Verlet algorithm**[17] is the most widely adopted method. Given the position, velocity and acceleration of atoms in timestep n, it solves the position of atoms in the next time step $n + 1$ by Taylor expansion:

$$\mathbf{x}_{n+1} = \mathbf{x}_n + \dot{\mathbf{x}}_n \Delta t + \ddot{\mathbf{x}}_n \Delta t^2/2 \tag{3.4}$$

The velocity Verlet algorithm utilized a velocity in time integration, which is not the case by original Verlet algorithm. It calculates the velocity of the next time step by

$$\dot{\mathbf{x}}_{n+1} = \dot{\mathbf{x}}_n + (\ddot{\mathbf{x}}_{n+1} + \ddot{\mathbf{x}}_{n-1})\Delta t/2 \tag{3.5}$$

Note that the acceleration can always be obtained by **(3.3)** if the potential surface and the position are given.

$$\ddot{\mathbf{x}}_{n+1} = -\nabla_i V(\mathbf{x}_{n+1})/m \tag{3.6}$$

By applying this iteration, the movement of all atoms in all time can be integrated.

In most cases, we want to control some envionmental variables such as pressure P, temperature T in order to observe the dynamic behavior in different situations. This is called the *ensembles*. The simplest ensemble is NVE, which fixes the number of atoms, volumes and energy. However, in real world cases, we often fix the temperature T or the external pressure P. The NVT and NPT ensemble is used for the case. The NVT ensemble fixed the *volume* and controls the *temperature* while the NPT ensemble controls the *pressure* and *temperatures*. They utilizes the Nosé Hoover thermostat and barostat for the control of temperature and pressure.

In summary, A classical molecular dynamics consists of the following elements:

- **The molecular or crystal structure.**

  This is the structure of the simulation system of interest.

- **The force field.**

  This is the energy function that depends on atomic position.

- **The time integration algorithm.**

  This is the algorithm used to solve the Newton's equation of motion.

- **The statistic mechanical ensemble and simulation conditions.**

  The statistic mechanical ensemble like the microcanonical ensemble NVE, canonical ensemble NVT or isothermal-isobaric ensemble NPT, *etc.* can be imposed on the system to simulate the real world cae.

3.2 Reactive Force Field (ReaxFF)

The ReaxFF[18] is developed by van Duin *et al.* in 2001. It is first used for C/H system initially. It is later modified by Chenoweth[19] *et al.* in 2008. Most of the simulation packages like LAMMPS[20 and 21] or GULP[22 and 23] utilize this functional form. The `user-reaxc` package in LAMMPS is a revision of the Aktulga *et al.*'s implementation[21]. The following parameter description can be found in the supporting information of Chenoweth *et al.*'s paper.

First, the energy function of ReaxFF is composed of the following parameters

$$
\begin{aligned}
E_{\text{system}} = {} & E_{\text{bond}} + E_{\text{lp}} + E_{\text{over}} + E_{\text{under}} \\
& + E_{\text{val}} + E_{\text{pen}} + E_{\text{coa}} + E_{\text{C2}} + E_{\text{triple}} + E_{\text{tors}} + E_{\text{conj}} \\
& + E_{\text{H-bond}} + E_{\text{vdWaals}} + E_{\text{Coulomb}}
\end{aligned}
$$

The ReaxFF utilizes the **bond order** to describe the energy surface of bond-breaking. The bond order (uncorrected) is described by the function below

$$
\begin{aligned}
BO_{ij}' &= BO_{ij}'^{\,\sigma} + BO_{ij}'^{\,\pi} + BO_{ij}'^{\,\pi\pi} \\
&= \exp\left[p_{bo,1}\left(\frac{r_{ij}}{r_0^{\sigma}}\right)^{p_{bo,2}}\right] + \exp\left[p_{bo,3}\left(\frac{r_{ij}}{r_0^{\sigma}}\right)^{p_{bo,4}}\right] + \exp\left[p_{bo,5}\left(\frac{r_{ij}}{r_0^{\sigma}}\right)^{p_{bo,6}}\right]
\end{aligned}
$$

The energy of each term is a function of the bond order. *e.g.* for the first term E_{bond} we have

$$
E_{bond} = -D_e^{\sigma} BO_{ij}^{\sigma} \exp[p_{be,1}(1 - (BO_{ij}^{\sigma})^{p_{be,2}})] - D_e^{\pi} BO_{ij}^{\pi} - D_e^{\pi\pi} BO_{ij}^{\pi\pi} \tag{3.7}
$$

Figure **3.1** is the results of the Si–O reactive force field[24] published in 2003. It shows the energy–distance curve that the energy will be close to zero when the distance of Si–Si is larger enough. This is different from the traditional forcefield like harmonic oscillator approximation, which will be the infinity when the distance goes to infinity. Since the atoms can be separated (bond-breaking) without being attracted. This will be able to describe the bond-breaking behavior, which is critical in our study since Si–Si bond must be broken in our study.

In addition to the bond-breaking behavior, ReaxFF is also able to describe the charge state in each atom. In the ReaxFF implemented by LAMMPS, it used the charge equilibration scheme (Qeq)[25] to calculate the charge for each atom.

In order to study the Li–Si system, we utilizes the $\text{ReaxFF}_{\text{LiSiAlO}}$ obtained from Ostadhossein *et al.*[26] which have the Li–Si parameter obtained from the same group.[14] This parameter is a enhanced parameter from Fan *et al.*[27]

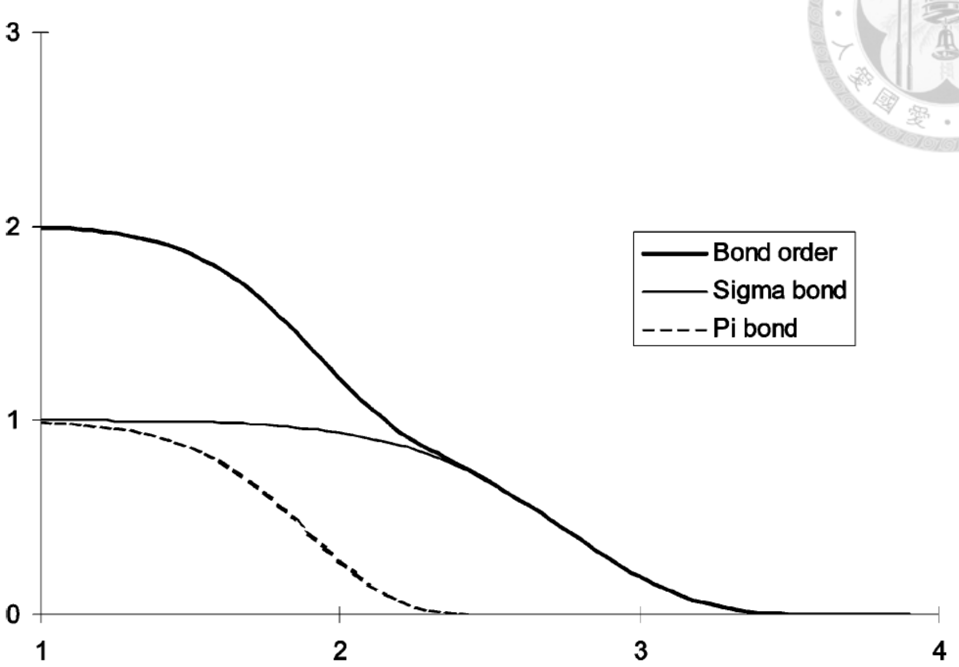

The bond order function with respect to distance

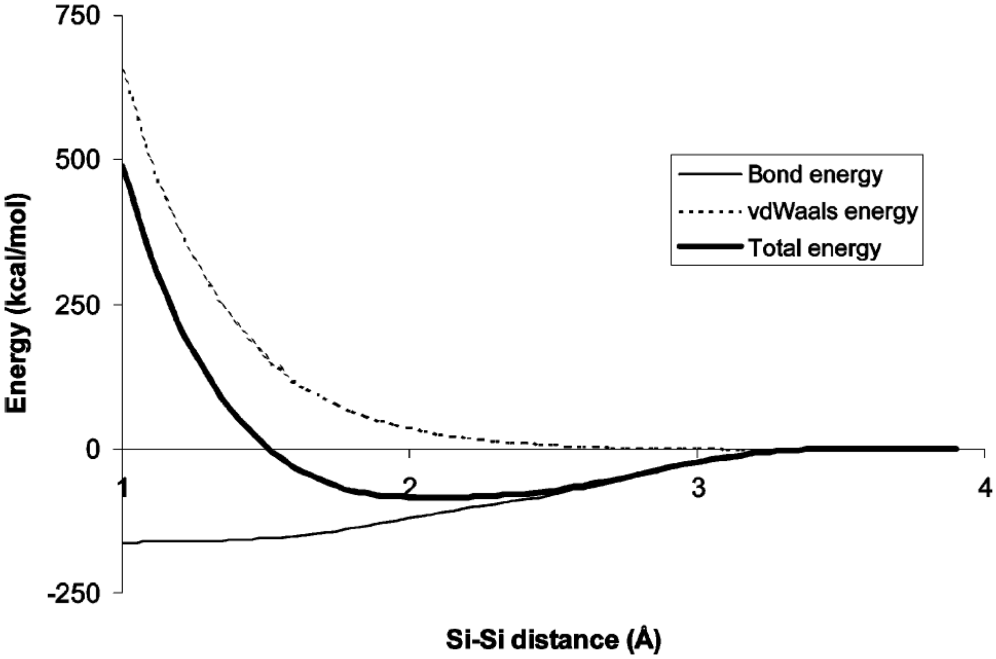

The bond breaking energy–distance curve

Figure 3.1 The bond order function and the bond breaking behavior in ReaxFF

doi:10.6342/NTU201703940

CHAPTER 4 ReaxFF Parameter Validation

4.1 Computational Details

We have mentioned that the ReaxFF parameter that we used are taken from Ostadhossein *et al.*. In this part, we will validate the parameter by checking for the structural properties, charge, thermodynamical properties, mechanical properties and diffusion energy barrier of Li in Si by nudged elastic band method.

It is worth mention that when evaluating energy volume curve. Some break-points are found in the original parameter. Therefore, some changes are made in order to make the energy volume curve smoother. The detailed change is described in the appendix.

For the crystal structure, We used the following structures for calculation.

c-Si, *c*-LiSi[28], *c*-$Li_{12}Si_7$[29], *c*-$Li_{13}Si_4$[30], *c*-$Li_{15}Si_4$[31], *c*-$Li_{17}Si_4$[32], *c*-$Li_{22}Si_5$ and *c*-Li.

while for the amorphous structure, the following structures generated by DFT data from Chiang *et al.*[33] are used.

a-$Li_{20}Si_{44}$, *a*-$Li_{22}Si_{42}$, *a*-$Li_{32}Si_{32}$, *a*-$Li_{36}Si_{28}$, *a*-$Li_{40}Si_{24}$,
a-$Li_{42}Si_{22}$, *a*-$Li_{45}Si_{19}$, *a*-$Li_{46}Si_{18}$, *a*-$Li_{50}Si_{14}$

Each concentration are averaged with 3 samples. The *a*-Li_xSi are equilibrated in 300, 600 and 1200 K and fully relaxed for the most stable structure and energy.

4.1.1 Structural Properties

The crystal structures mentioned previously are calculated. We used the fully relaxation command `fix box/relax` implemented in LAMMPS for structure optimization. The convergence criteria is 10^{-3} kcal/mol/Å **force convergence**, which corresponds to 4.3×10^{-5} eV/Å force convergence. The **lattice constants** and **energy volume curve** of ReaxFF optimized, DFT and the experimental results were compared for ReaxFF parameter valida-

doi:10.6342/NTU201703940

tion. The energy volume curve are calculated by isotropically scaling the lattice constant of the structure from 0.95x to 1.05x.

In order to catch the structural properties, we have utilized the radial distribution function (RDF) to check for the structural resemblance. It is defined as in **(4.1)**

$$g_{ij}(r) = \frac{\mathrm{d}n_j(r)}{4\pi r^2 \rho \mathrm{d}r} \tag{4.1}$$

while i, j are the type of atoms, and $\mathrm{d}n(r)$ is the number of atoms of type j in the $\mathrm{d}r$ shell with the center of atom type i. This shows the atom distance distribution in on structure.

4.1.2 Thermodynamic Properties

The **melting point** is tested for *c*-Si and *c*-Li in **NPT** and the **potential energy** is sampled for 10 ps. The structures and temperatures range are presented as follows:

- Si: $8 \times 8 \times 8$ diamond with 4096 atoms in $1200 - 1650$ K.
- Li: $8 \times 8 \times 8$ BCC with 1024 atoms in $300 - 600$ K.

The **mixing energy** and **formation energy** are the concept of the mixing behavior in thermodynamics. The mixing energy is defined as

$$E_{\mathrm{mix}} = E_{\mathrm{Li}_x\mathrm{Si}_{1-x}} - xE_{\mathrm{Li}} - (1-x)E_{\mathrm{Si}} \tag{4.2}$$

while for formation energy

$$E_{\mathrm{form}} = E_{\mathrm{Li}_x\mathrm{Si}} - xE_{\mathrm{Li}} - E_{\mathrm{Si}} \tag{4.3}$$

For the anode reaction, the **formation energy** is more important since **the amount of Si is fixed** in anode. The lithiation voltage is the derivative of the formation energy.

$$V = -\{(E_{\mathrm{form,Li_ySi}} - E_{\mathrm{form,Li_xSi}})/(y-x) - E_{Li}\} \tag{4.4}$$

doi:10.6342/NTU201703940

4.1.3 Mechanical Properties

The mechanical properties is the stress and strain relationships in the material. First, the stress tensor is defined as

$$\sigma_{ij} = \frac{F_j}{A_i} \tag{4.5}$$

while

F_j = The force on direction j

A_i = The area on direction i

We can also define the deformation gradient tensor

$$e_{ij} = \frac{\partial \Delta x_i}{\partial x_j} \tag{4.6}$$

while

Δx_i = The dimensional change in direction i

x_j = The normal vector of the facet direction j

The strain tensor ϵ_{ij} is defined as its straining component, while ω_{ij} is its rotational component as shown in equation (**4.7**).

$$\mathbf{e} = \frac{1}{2}(\mathbf{e} + \mathbf{e}^t) + \frac{1}{2}(\mathbf{e} - \mathbf{e}^t) = \boldsymbol{\varepsilon} + \boldsymbol{\omega} \tag{4.7}$$

After the stress tensor and the strain tensor are defined, we have the generalized Hooke's law (in Einstein notation)

$$\sigma_{ij} = c_{ijkl}\varepsilon_{kl} \tag{4.8}$$

doi:10.6342/NTU201703940

In static equilibrium, we have $\sigma_{ij} = \sigma_{ji}$ and $\varepsilon_{ij} = \varepsilon_{ji}$. Therefore, the generalized Hooke's law can be reduced by changing the 11 → 1, 22 → 2, 33 → 3, 23(32) → 4, 31(13) → 5, 12(21) → 6 (The Voigt notation). Then we have

$$\sigma_i = c_{ij}\varepsilon_j \tag{4.9}$$

Note that

$$\varepsilon_4 = \varepsilon_{23} + \varepsilon_{32}, \varepsilon_5 = \varepsilon_{13} + \varepsilon_{31}, \varepsilon_4 = \varepsilon_{12} + \varepsilon_{21}$$

The stiffness tensor c_{ij} is shown in matrix form as in equation **(4.10)**.

$$\begin{pmatrix} \sigma_{xx} \\ \sigma_{yy} \\ \sigma_{zz} \\ \sigma_{yz} \\ \sigma_{zx} \\ \sigma_{xy} \end{pmatrix} = \begin{pmatrix} c_{11} & c_{12} & c_{13} & c_{14} & c_{15} & c_{16} \\ c_{21} & c_{22} & c_{23} & c_{24} & c_{25} & c_{26} \\ c_{31} & c_{32} & c_{33} & c_{34} & c_{35} & c_{36} \\ c_{41} & c_{42} & c_{43} & c_{44} & c_{45} & c_{46} \\ c_{51} & c_{52} & c_{53} & c_{54} & c_{55} & c_{56} \\ c_{61} & c_{62} & c_{63} & c_{64} & c_{65} & c_{66} \end{pmatrix} \begin{pmatrix} \varepsilon_{xx} \\ \varepsilon_{yy} \\ \varepsilon_{zz} \\ \varepsilon_{yz} \\ \varepsilon_{zx} \\ \varepsilon_{xy} \end{pmatrix} \tag{4.10}$$

while the compliance tensor is its invert matrix in equation **(4.11)**.

$$\begin{pmatrix} \varepsilon_{xx} \\ \varepsilon_{yy} \\ \varepsilon_{zz} \\ \varepsilon_{yz} \\ \varepsilon_{zx} \\ \varepsilon_{xy} \end{pmatrix} = \begin{pmatrix} s_{11} & s_{12} & s_{13} & s_{14} & s_{15} & s_{16} \\ s_{21} & s_{22} & s_{23} & s_{24} & s_{25} & s_{26} \\ s_{31} & s_{32} & s_{33} & s_{34} & s_{35} & s_{36} \\ s_{41} & s_{42} & s_{43} & s_{44} & s_{45} & s_{46} \\ s_{51} & s_{52} & s_{53} & s_{54} & s_{55} & s_{56} \\ s_{61} & s_{62} & s_{63} & s_{64} & s_{65} & s_{66} \end{pmatrix} \begin{pmatrix} \sigma_{xx} \\ \sigma_{yy} \\ \sigma_{zz} \\ \sigma_{yz} \\ \sigma_{zx} \\ \sigma_{xy} \end{pmatrix} \tag{4.11}$$

The mechanical properties is calculated by adding **strain** on the cell and check for its **stress**. For example, the strain of 0.001 can be added on the ε_{xx}, ε_{yy}, ε_{zz}, ε_{yz}, ε_{zx}, ε_{xy}

respectively. By using LAMMPS structure optimization routine with cell fixed, the stress will be outputted as σ_{xx}, σ_{yy}, σ_{zz}, σ_{yz}, σ_{zx}, σ_{xy}. The stiffness tensor c_{ij} can therefore be solved.

The Young's modulus E, shear modulus G and bulk modulus B can be obtained by the formula of Reuss, Voigt and Hill[34]. Note that this only holds in isotropic material.

- The Voigt model is shown as follows

$$E_V = \frac{(A - B + 3C)(A + 2B)}{2A + 3B + C}$$

$$G_V = \frac{A - B + 3C}{5}$$

$$B_V = \frac{A + 2B}{3}$$

while

$$A = (c_{11} + c_{22} + c_{33})/3$$

$$B = (c_{12} + c_{23} + c_{31})/3$$

$$C = (c_{44} + c_{55} + c_{66})/3$$

- The Reuss model is shown as follows

$$E_R = \frac{5}{3X + 2Y + Z}$$

$$G_R = \frac{5}{4X - 4Y + 3Z}$$

$$B_R = \frac{1}{3(X + 2Y)}$$

while

$$X = (s_{11} + s_{22} + s_{33})/3$$

$$Y = (s_{12} + s_{23} + s_{31})/3$$

$$Z = (s_{44} + s_{55} + s_{66})/3$$

- The Hill model averages Voigt and Reuss model

$$E_H = (E_V + E_R)/2$$

$$G_H = (G_V + G_R)/2$$

$$B_H = (B_V + B_R)/2$$

In this case, We calculated the Si diamond structure, Li BCC structure and some Li–Si alloys in ReaxFF, Stillinger-Weber and VASP for comparison.

4.1.4 Nudged Elastic Band Calculation of Li diffusion in crystalline Si

The final validation is the Li diffusion barrier in Si diamond crystal. In order to calculate the dynamical properties, it is crucial to check for the diffusion energy barrier of lithium in silicon. It is calculated by nudged-elastic band (NEB) method. The nudged-elastic band (NEB) method finds the **saddle point** of the energy surface during reaction. It can be though of as a series of springs in a energy surface and it will finally find the saddle point by the contraction of the spring as shown in figure **4.1**.

We tested the diffusion barrier of lithium in silicon T_d site to another silicon T_d site by ReaxFF. The silicon cell size is $4 \times 4 \times 4$. We have used 21 images in my calculations.

doi:10.6342/NTU201703940

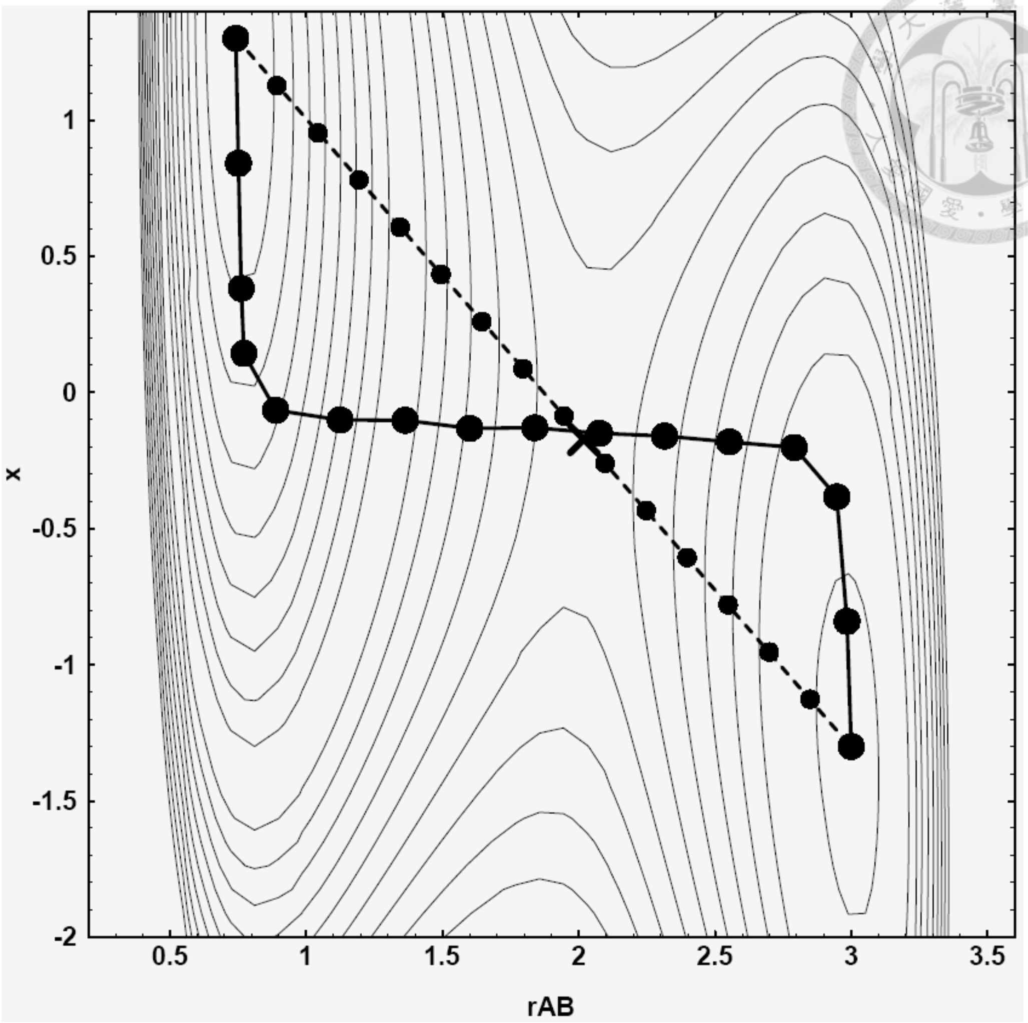

Figure 4.1 The illustration of the nudge elastic band method

doi:10.6342/NTU201703940

4.2 Structural Properties

The energy volume curve of *c*-Si, *c*-LiSi, *c*-$Li_{12}Si_7$, *c*-$Li_{13}Si_4$, *c*-$Li_{15}Si_4$, *c*-$Li_{22}Si_5$ and *c*-Li are shown in figure **4.2**, **4.3**, **4.4**, **4.5**, **4.6**, **4.7** and **4.8** respectively. We can observed that a smooth energy volume curve is obtained. (by applying the changes in appendix)

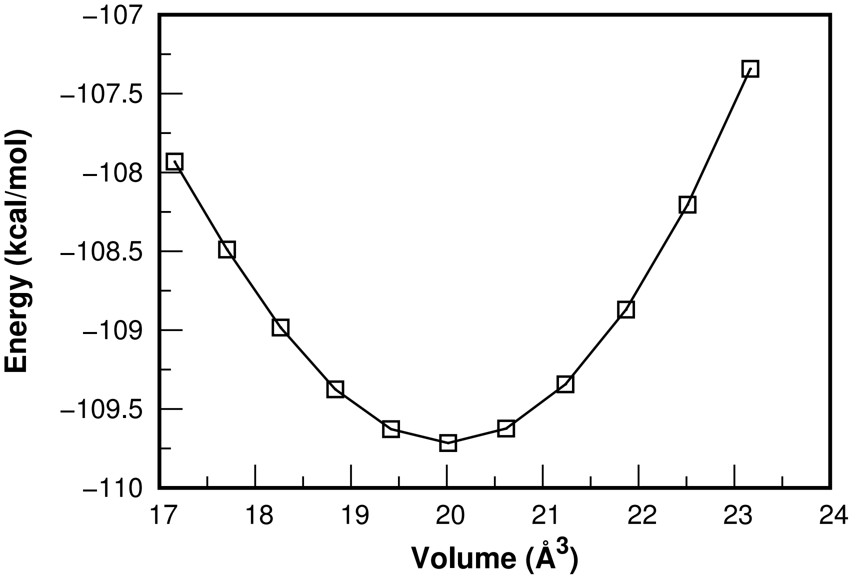

Figure 4.2 The energy volume curve of *c*-Si

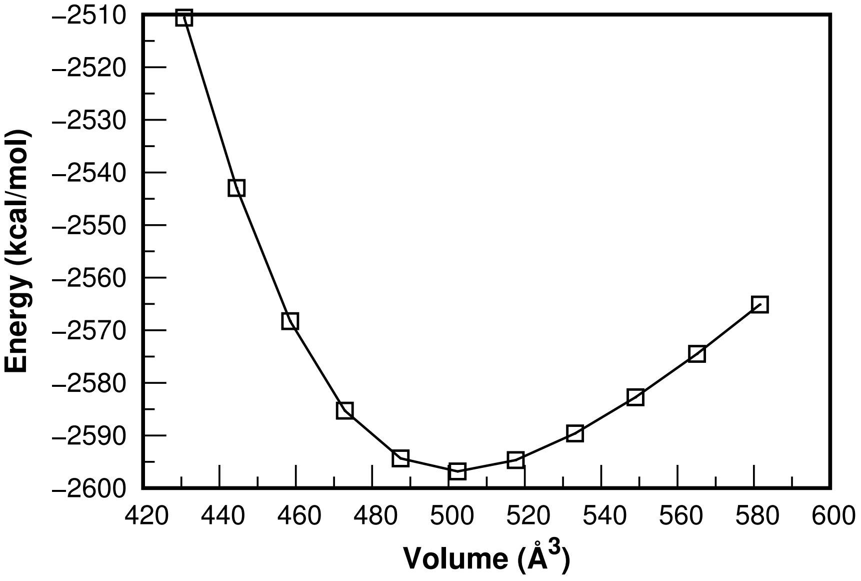

Figure 4.3 The energy volume curve of *c*-LiSi

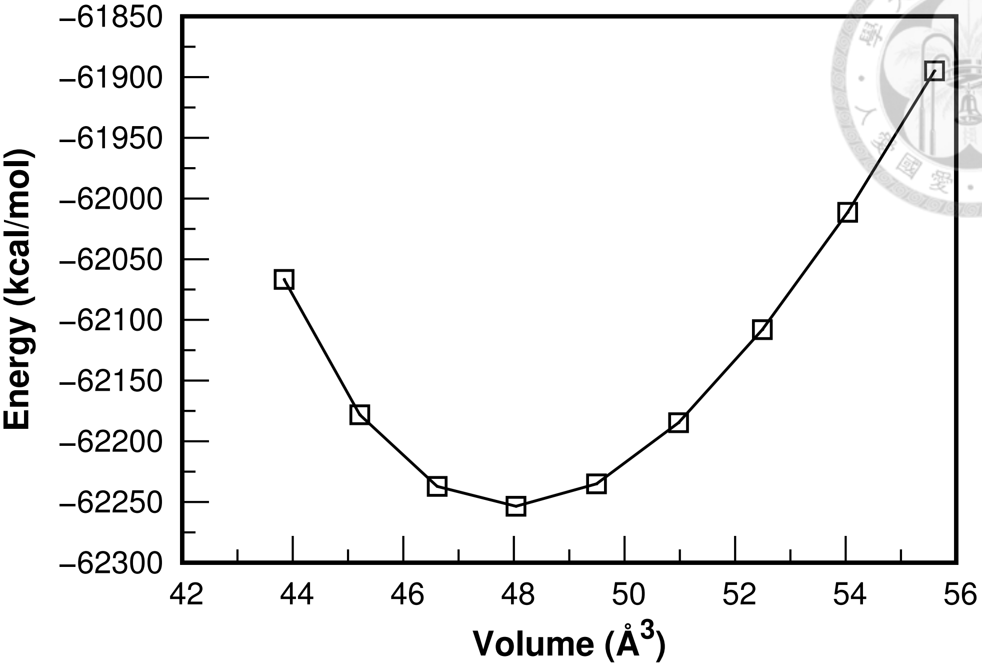

Figure 4.4 The energy volume curve of *c*-$Li_{12}Si_7$

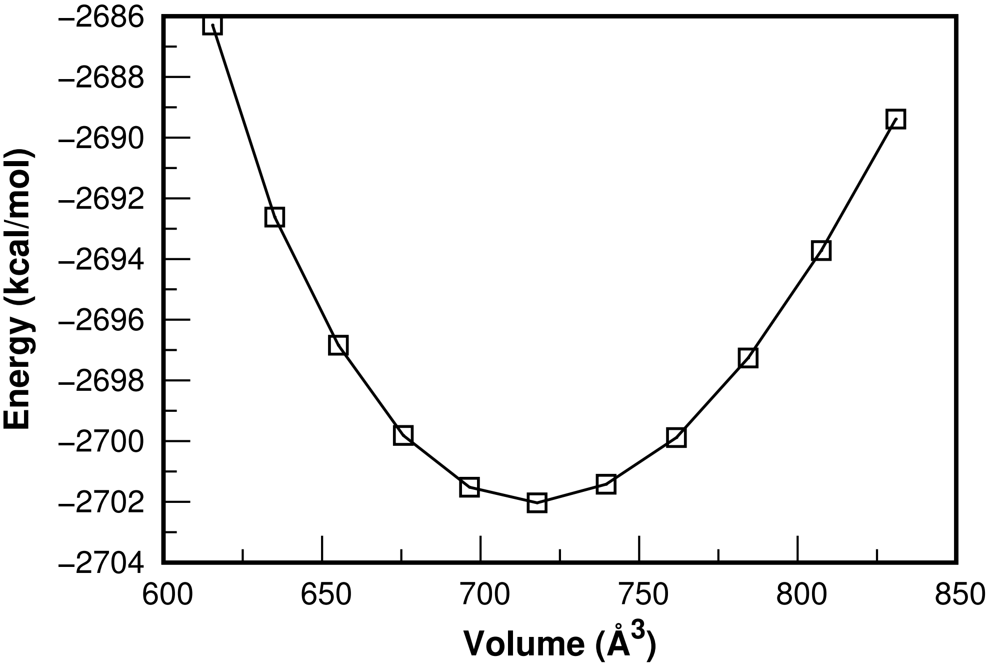

Figure 4.5 The energy volume curve of *c*-$Li_{13}Si_4$

doi:10.6342/NTU201703940

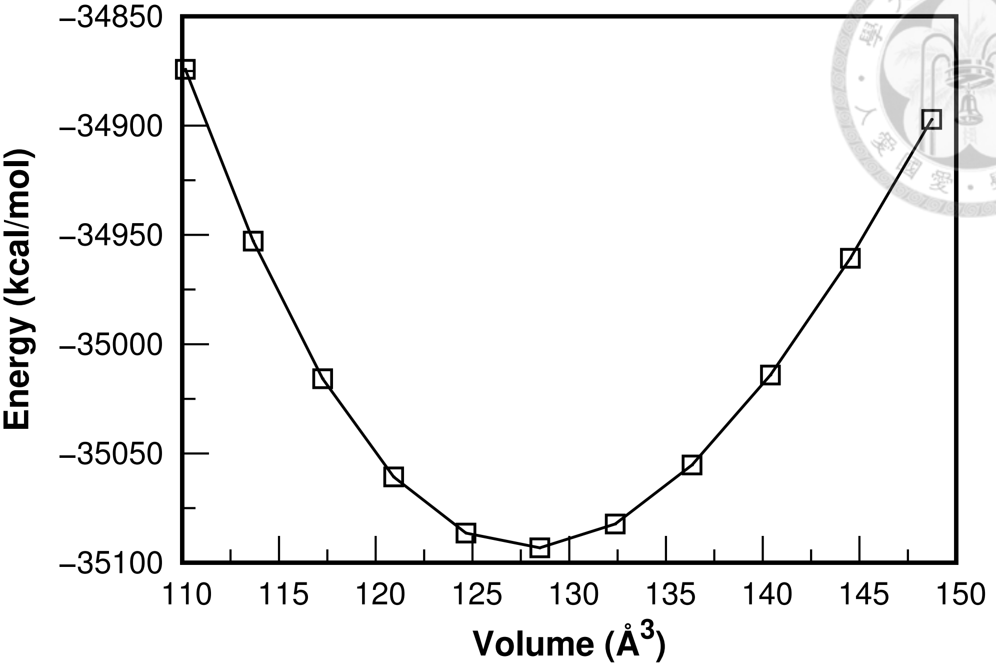

Figure 4.6 The energy volume curve of c-$Li_{15}Si_4$

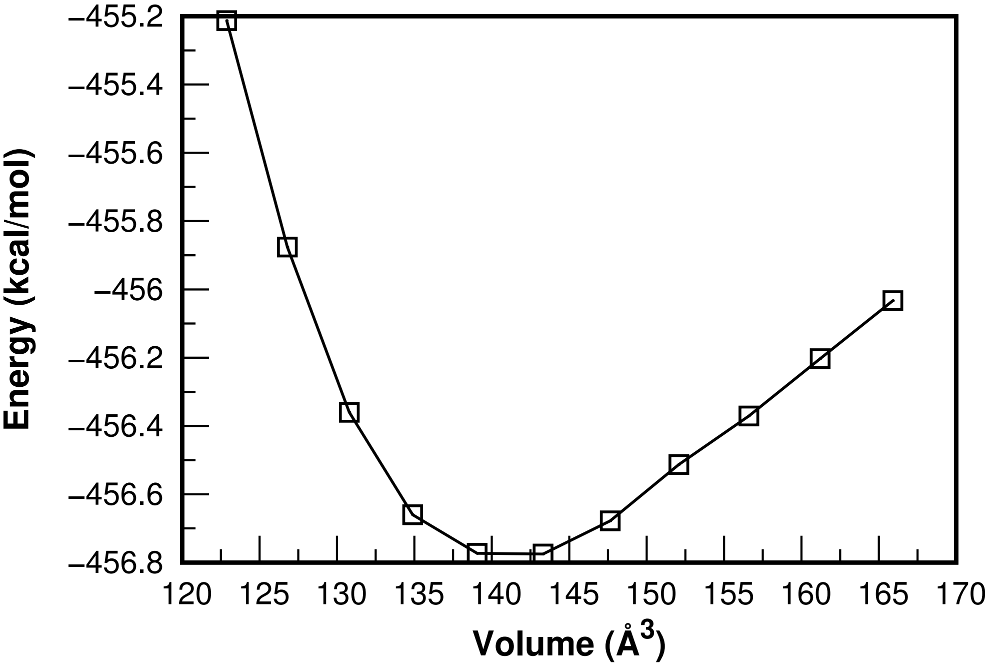

Figure 4.7 The energy volume curve of c-$Li_{22}Si_5$

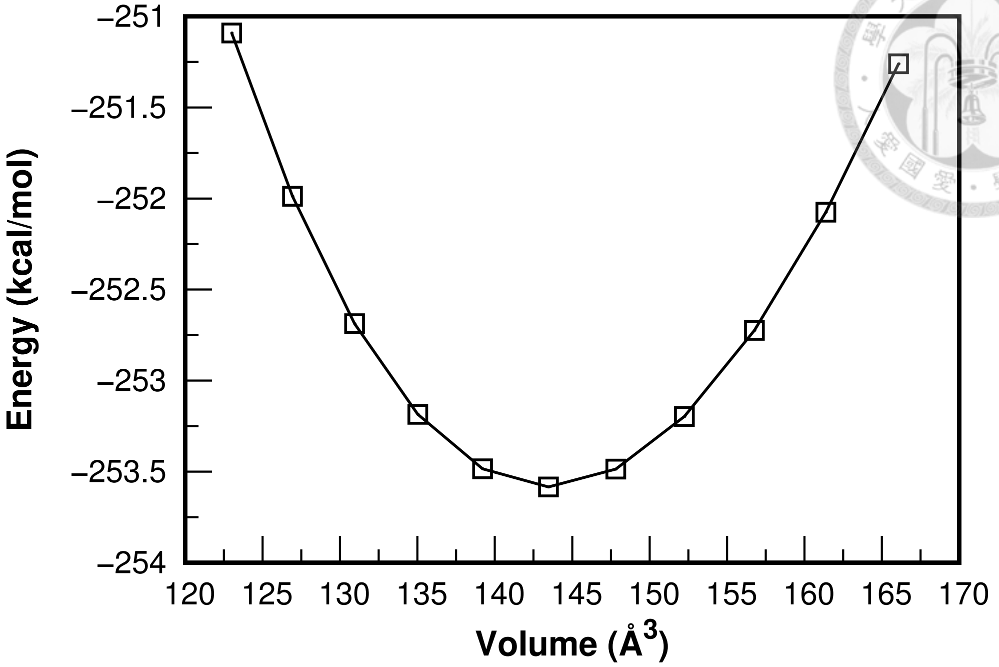

Figure 4.8 The energy volume curve of *c*-Li

The lattice constants of Si, Li and Li–Si alloys calculated by the optimization as described in the previous section are shown as in table **4.1**:

We can observe very good agreement of the ReaxFF, DFT and experimental results in lattice constant. The comparison of ReaxFF charge and Bader charge (adopted from Chevrier *et al.*[35]) in crystalline Li–Si alloys is shown in table **4.2**. The Bader charge in amorphous Li–Si alloys are also calculated in table **4.3**. The charge of Li in ReaxFF has a value of about the half of the Bader charge. It is closer to the Mulliken charge calculated by Li_2O in Gaussian as 0.4 e.

The RDF of *a*-$Li_{32}Si_{32}$ by ReaxFF and DFT is compared in figure **4.9**, **4.10**, **4.11**. While *a*-$Li_{40}Si_{24}$ and *a*-$Li_{50}Si_{14}$ are shown in figure **4.12**, **4.13**, **4.14** and **4.15**, **4.16**, **4.17** respectively. The coordination number is calculated by the integration with cutoff shown in table **4.4**. The coordination number of each concentration is shown in table **4.5**.

A good description of the structural properties can be observed in the radial distribution

doi:10.6342/NTU201703940

	c-Si	*c*-LiSi			*c*-Li$_{12}$Si$_7$		
	a(Å)	*a*(Å)	*b*(Å)	*c*(Å)	*a*(Å)	*b*(Å)	*c*(Å)
ReaxFF	5.46	9.48	9.48	5.59	8.40	19.95	14.30
DFT	5.46	9.35	9.35	5.75	8.55	19.67	14.33
exp	5.43	9.35	9.35	5.74	8.61	19.74	14.34

	c-Li$_{13}$Si$_4$			*c*-Li$_{15}$Si$_4$	*c*-Li$_{22}$Si$_5$	*c*-Li
	a(Å)	*b*(Å)	*c*(Å)	*a*(Å)	*a*(Å)	*a*(Å)
ReaxFF	7.74	15.45	4.38	10.61	18.61	3.44
DFT	7.92	15.11	4.44	10.62	18.65	3.44
exp	7.99	15.21	4.43	10.69	18.75	3.51

Table 4.1 The lattice constant of Li, Si and their alloys

species	Li (ReaxFF)	Li(Bader)	Si (ReaxFF)	Si(Bader)
c-LiSi	0.40	0.77	-0.40	-0.70
c-Li$_{12}$Si$_7$	0.36	0.76	-0.50	-1.36
c-Li$_{13}$Si$_4$	0.32	0.73	-1.03	-2.39
c-Li$_{15}$Si$_4$	0.30	0.80	-1.13	-2.72

Table 4.2 The comparison of ReaxFF and Bader charge of Li in crystalline Li–Si alloy (unit: e)

function. It shows similar peak position in DFT and ReaxFF. However, there are some slight difference between the ReaxFF and DFT data. While focusing on the Li–Li RDF in all concentration, a broader first peak can be observed in the structure. This shows that Li–Li will tend to be closer than the DFT result. The Li–Si bonding population in ReaxFF is lower than the DFT, which may indicate that the Li–Si bonding in ReaxFF is weaker than

species	Li (ReaxFF)	Li (Bader)	Si (ReaxFF)	Si (Bader)
a-$Li_{20}Si_{44}$	0.42	0.83	-0.19	-0.38
a-$Li_{22}Si_{42}$	0.42	0.83	-0.22	-0.43
a-$Li_{32}Si_{32}$	0.39	0.82	-0.39	-0.82
a-$Li_{36}Si_{28}$	0.37	0.82	-0.47	-1.05
a-$Li_{40}Si_{24}$	0.34	0.81	-0.57	-1.35
a-$Li_{42}Si_{22}$	0.33	0.81	-0.63	-1.54
a-$Li_{45}Si_{19}$	0.32	0.80	-0.75	-1.90
a-$Li_{46}Si_{18}$	0.31	0.80	-0.79	-2.04
a-$Li_{50}Si_{14}$	0.28	0.79	-1.01	-2.78

Table 4.3 The comparison of ReaxFF and Bader charge of Li in amorphous Li–Si alloy (unit: e)

bonding type	cutoff radius
Si–Si	2.8
Si–Li	3.6
Li–Si	3.6
Li–Li	3.9

Table 4.4 The cutoff radius used in the coordination number determiniation

in DFT result. Finally, The Si–Si peak is slightly higher than the DFT Si–Si peak, indicate stronger Si–Si bonding in ReaxFF. The same trend can also be found in the coordination number result in table **4.5**.

Despite the good reproduction of the structural properties by ReaxFF, the silicon structure have some irregular properties. In figure **4.18**, We have plotted the pressure vs. vol-

	a-$Li_{32}Si_{32}$		a-$Li_{40}Si_{24}$		a-$Li_{50}Si_{14}$	
bonding type	ReaxFF	DFT	ReaxFF	DFT	ReaxFF	DFT
Li–Li	6.88	6.87	9.14	8.54	9.61	10.35
Li–Si	7.46	6.90	5.31	5.21	2.64	2.87
Si–Li	7.46	6.90	8.84	8.68	9.44	10.25
Si–Si	3.38	2.79	2.77	2.13	1.58	0.80

Table 4.5 The coordination number of a-$Li_{32}Si_{32}$, a-$Li_{40}Si_{24}$ and a-$Li_{50}Si_{14}$

ume for the optimal lattice constant in NVT 1200 K by ReaxFF and Stillinger Weber potential. It shows that the optimal lattice constant in 1200 K is 5.32 Å, while it is 5.46 Å in 0 K optimization as shown in table **4.1**. We have tried fully relaxed the structure after 1200 K simulation, which has a lattice constant of 5.32 Å. However, it can not revert back into the lattice constant of 5.46 Å. It can only revert back to up to the lattice constant of 5.38 Å. Besides, the energy for lattice constant as 5.38 Å is *unstable* when comparing with the silicon structure in the lattice constant of 5.46 Å.

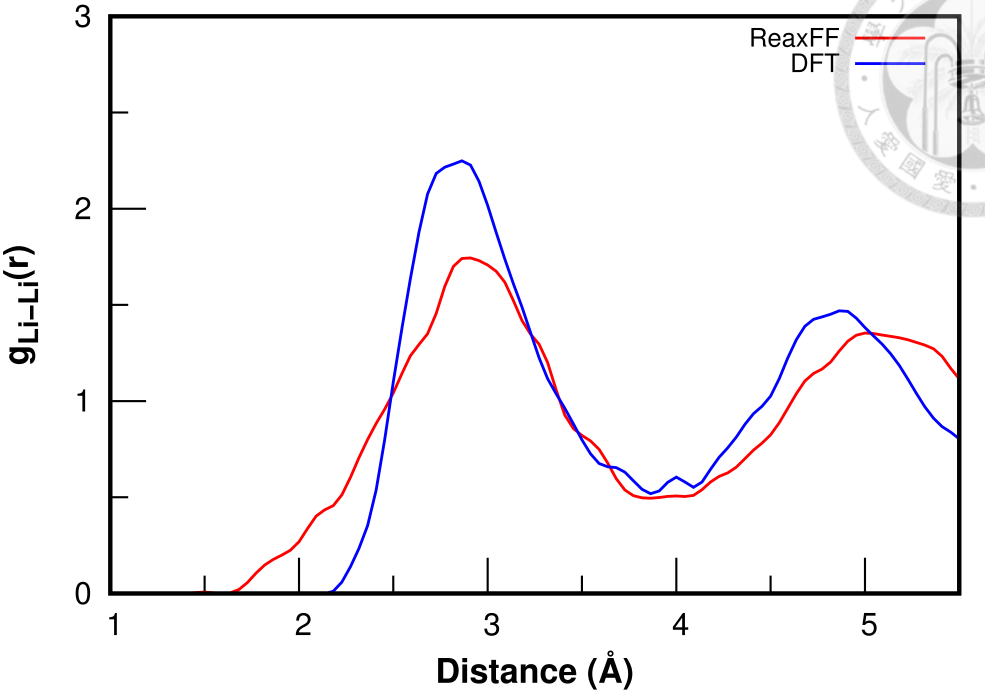

Figure 4.9 The radial distribution function of Li–Li in *a*-$Li_{32}Si_{32}$

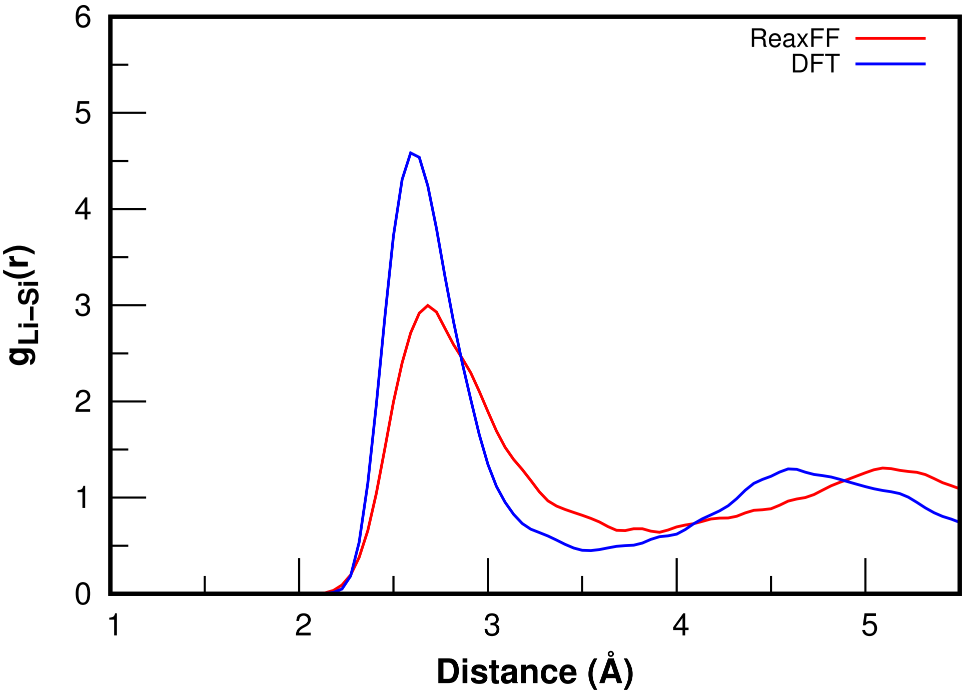

Figure 4.10 The radial distribution function of Li–Si in *a*-$Li_{32}Si_{32}$

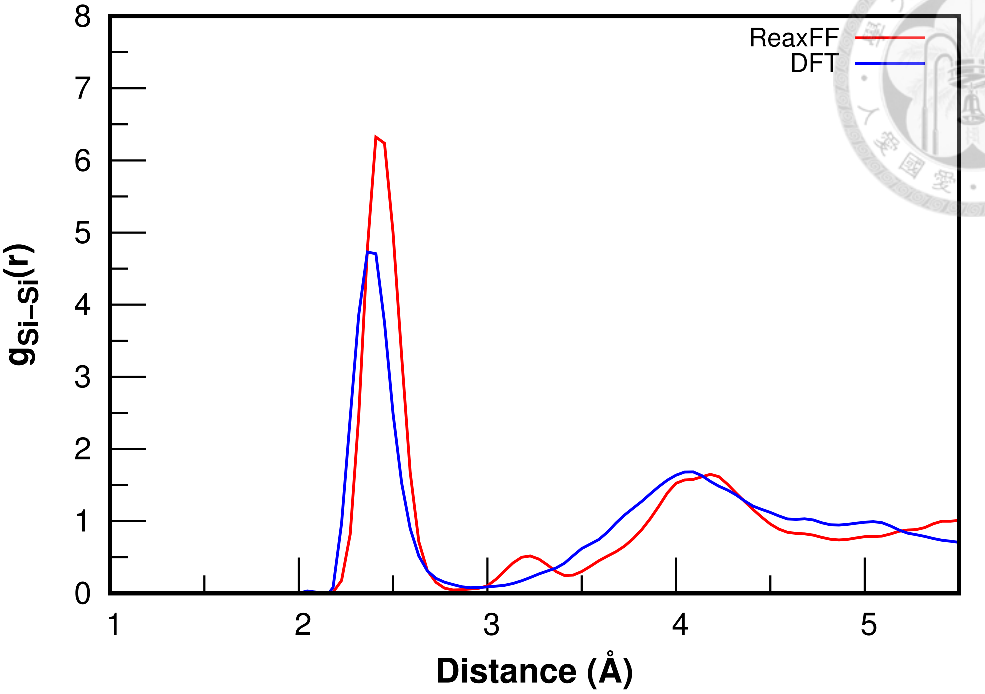

Figure 4.11 The radial distribution function of Si–Si in *a*-$Li_{32}Si_{32}$

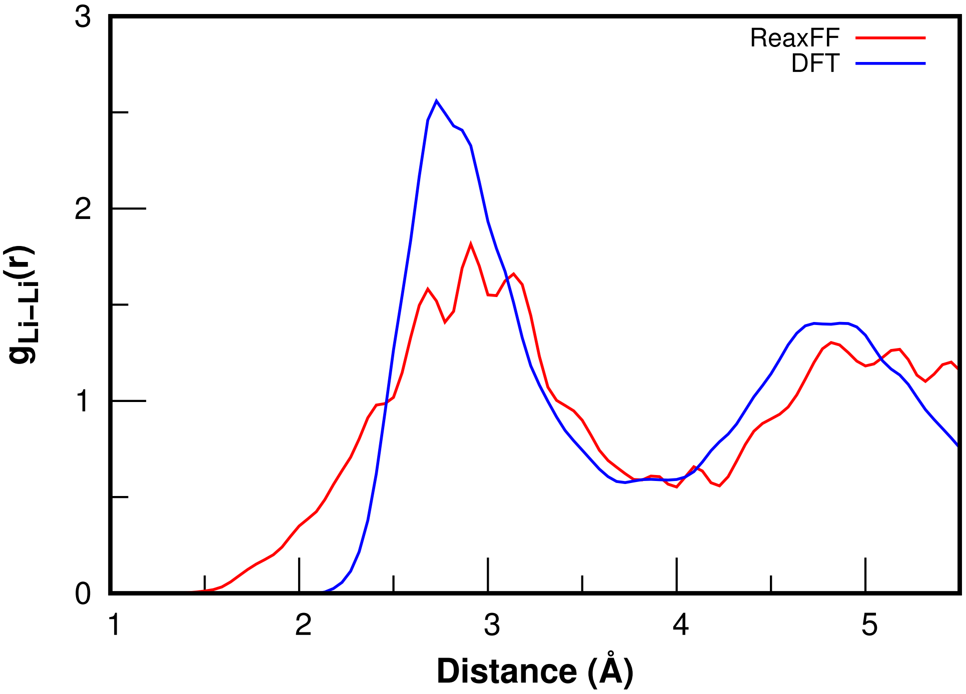

Figure 4.12 The radial distribution function of Li–Li in *a*-$Li_{40}Si_{24}$

doi:10.6342/NTU201703940

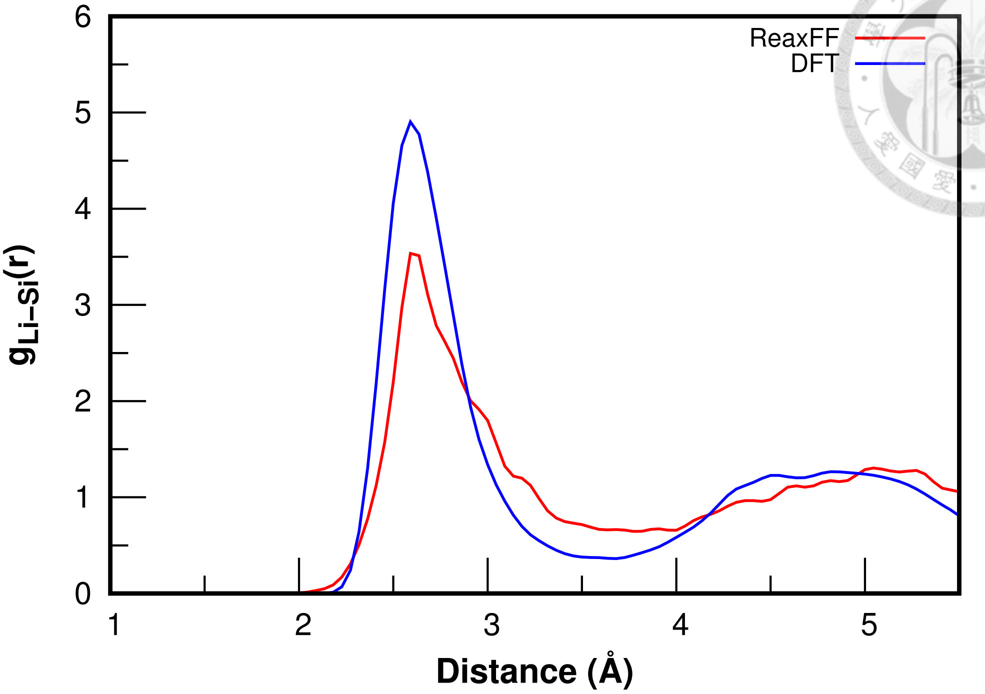

Figure 4.13 The radial distribution function of Li–Si in *a*-$Li_{40}Si_{24}$

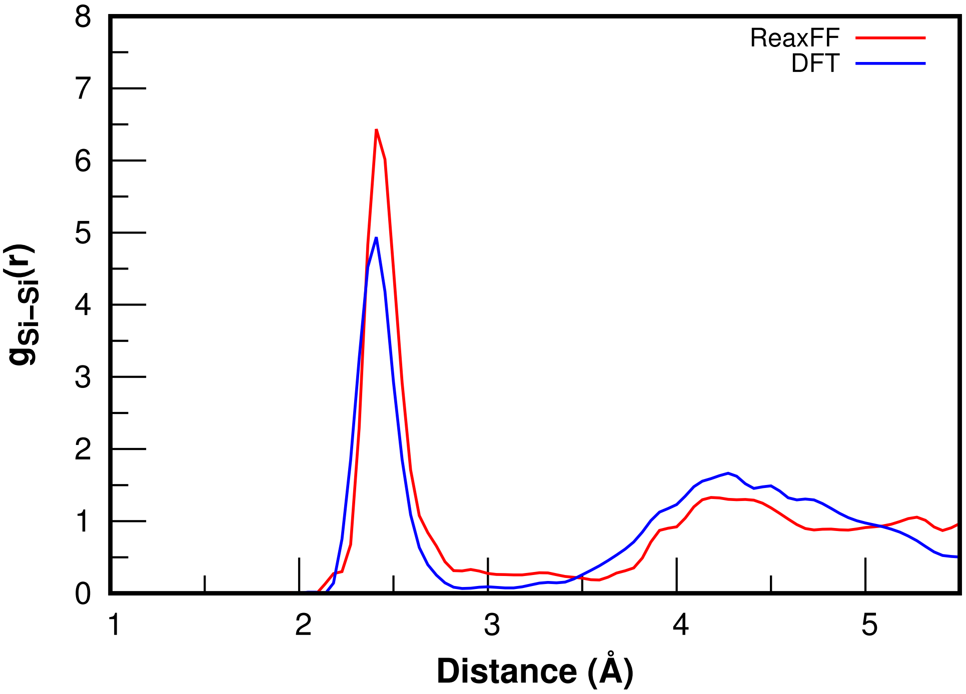

Figure 4.14 The radial distribution function of Si–Si in *a*-$Li_{40}Si_{24}$

doi:10.6342/NTU201703940

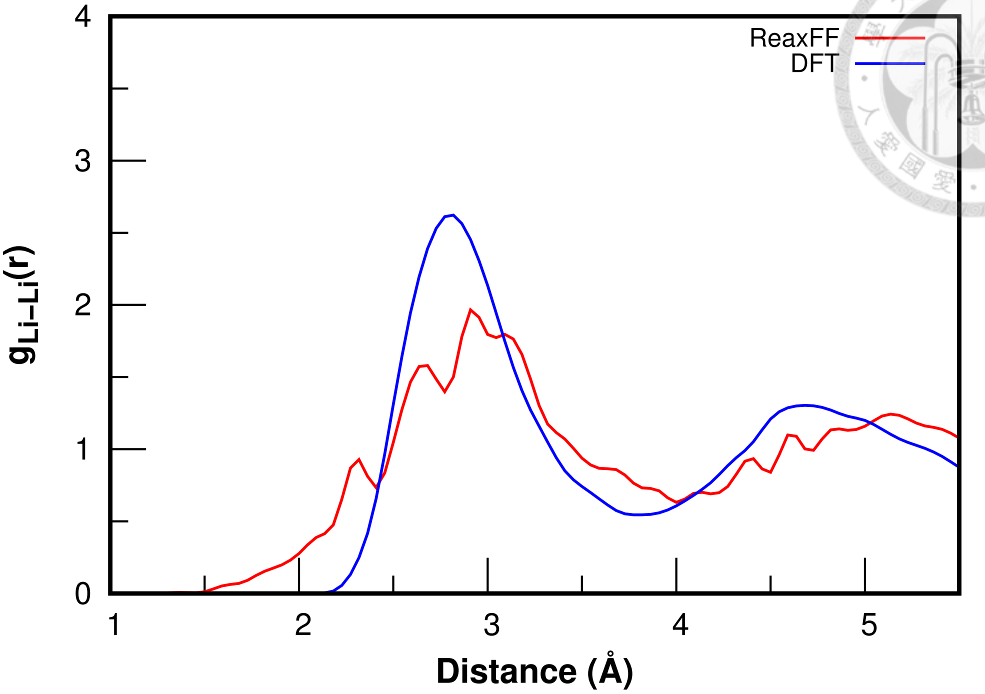

Figure 4.15 The radial distribution function of Li–Li in *a*-$Li_{50}Si_{14}$

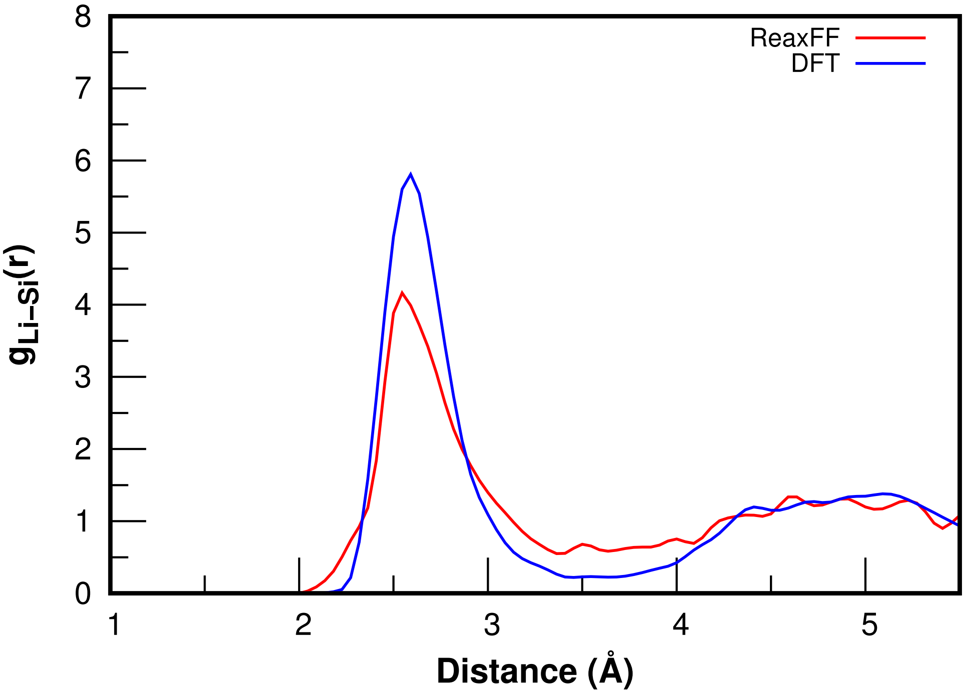

Figure 4.16 The radial distribution function of Li–Si in *a*-$Li_{50}Si_{14}$

doi:10.6342/NTU201703940

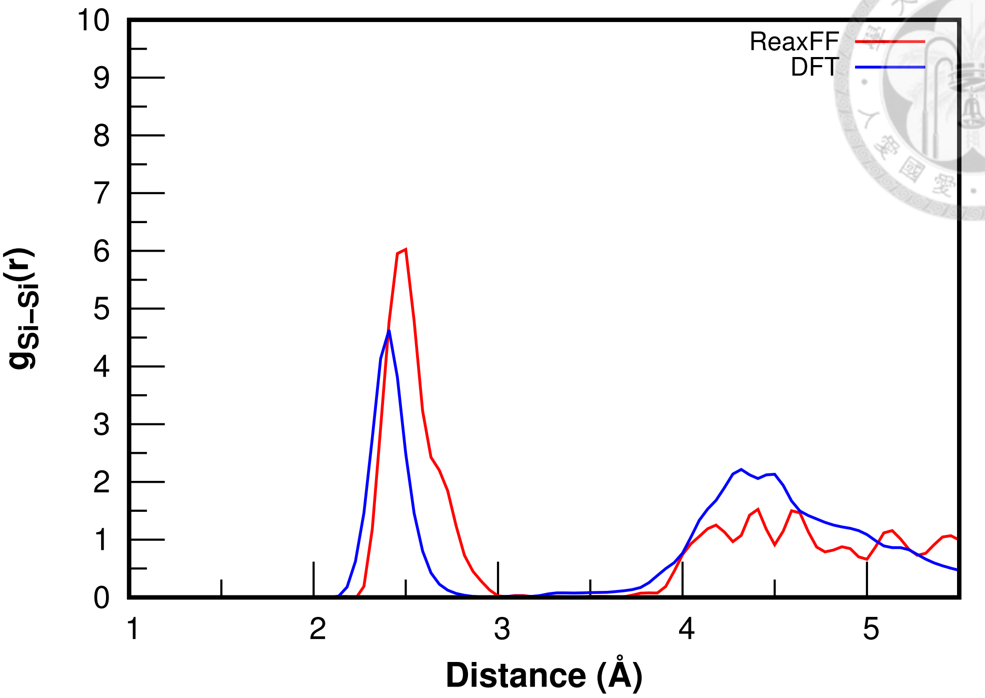

Figure 4.17 The radial distribution function of Si–Si in *a*-$Li_{50}Si_{14}$

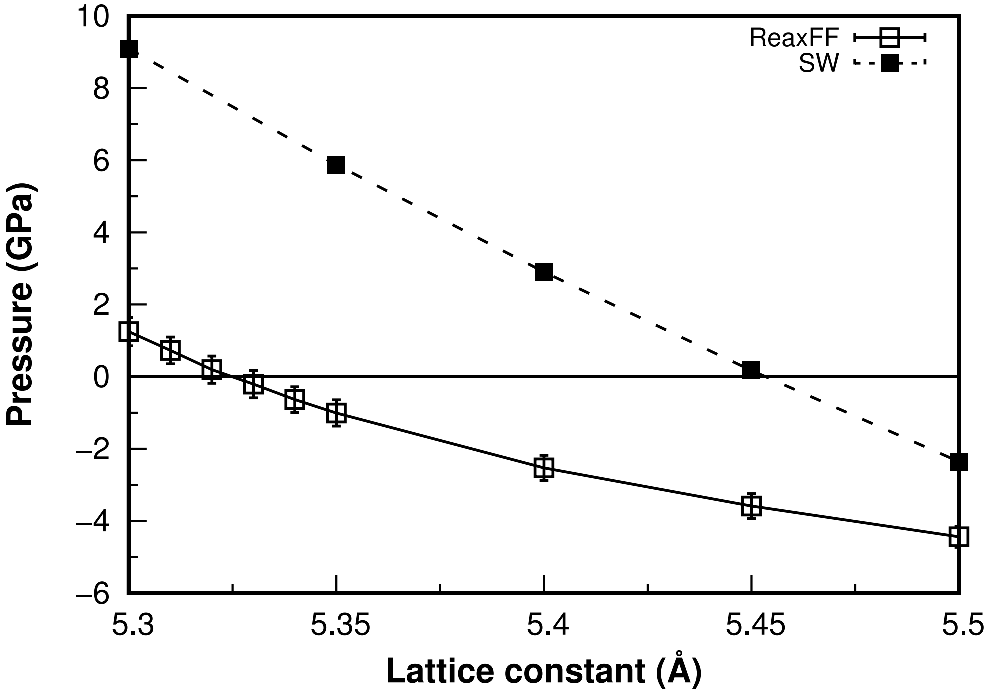

Figure 4.18 The pressure vs. volume curve comparison

between ReaxFF and Stillinger Weber in NVT 1200 K

doi:10.6342/NTU201703940

4.3 Thermodynamical Properties

The formation energy and mixing energy of crystalline Li–Si alloys are plotted as in figure **4.19** and **4.20**, while it is plotted as in figure **4.21** and **4.22** for amorphous Li–Si alloys. It is compared with the DFT results. We have also compared our result of crystalline Li–Si alloy with Fan *et al.*'s data in table **4.6**.

The crystalline formation and mixing energy shows some deviation from the DFT results, while the amorphous counterparts have similar trend with DFT data. The crystalline formation energy shows good agreement with Fan *et al.*'s data in table **4.6**. However, the amorphous alloy has a lower formation or mixing energy than the crystalline counterparts in the x range of $\mathrm{Li_xSi}$ and $\mathrm{Li_xSi_{1\text{-}x}}$ respectively. This is shown in figure **4.23** and **4.24**. The energy preference of a-$\mathrm{Li_xSi}$ means that the amorphous structure is more stable than the crystalline structure, which is a problem in the ReaxFF.

bonding type	ReaxFF (This work)	ReaxFF (Fan *et al.*)	DFT
c-LiSi	-14.96	-14.85	-9.30
c-$\mathrm{Li_{13}Si_4}$	-86.07	-85.47	-99.75
c-$\mathrm{Li_{15}Si_4}$	-95.07	-95.02	-104.84

Table 4.6 The comparison of ReaxFF formation energy with Fan *et al.*'s data and DFT data. (unt: kcal/mol)

The volume expansion ratio is plotted with DFT data in figure **4.25** and also shows good agreement. We can also observe that the volume of the ReaxFF structure are typicially smaller than the DFT data.

doi:10.6342/NTU201703940

The potential energy curve of Si is plotted in figure **4.26** while the potential energy curve of Li is calculated in figure **4.27**. An abrupt increase in potential energy means phase transformation and therefore the melting point. We have got a range of 1450–1500 K for silicon while about 450 K for lithium. The experimental value is 1687 K for silicon and 453.65 K for lithium.[36] It shows good agreement with the experimental data. We have also tested the melting point *c*-$Li_{12}Si_7$, *c*-$Li_{13}Si_4$, *c*-$Li_{15}Si_4$ and *c*-$Li_{22}Si_5$. However, the *c*-$Li_{13}Si_4$, *c*-$Li_{15}Si_4$ and *c*-$Li_{22}Si_5$ structure collapsed at 400 K and *c*-$Li_{12}Si_7$ collapsed at 300 K. Even when the structures are not collapsed, the lithium atoms show high mobility and diffused off from the equilibrium sites. This shows the instability in the crystal structure, and the agreement with the relative stability of the amorphous and the crystal structures found previously.

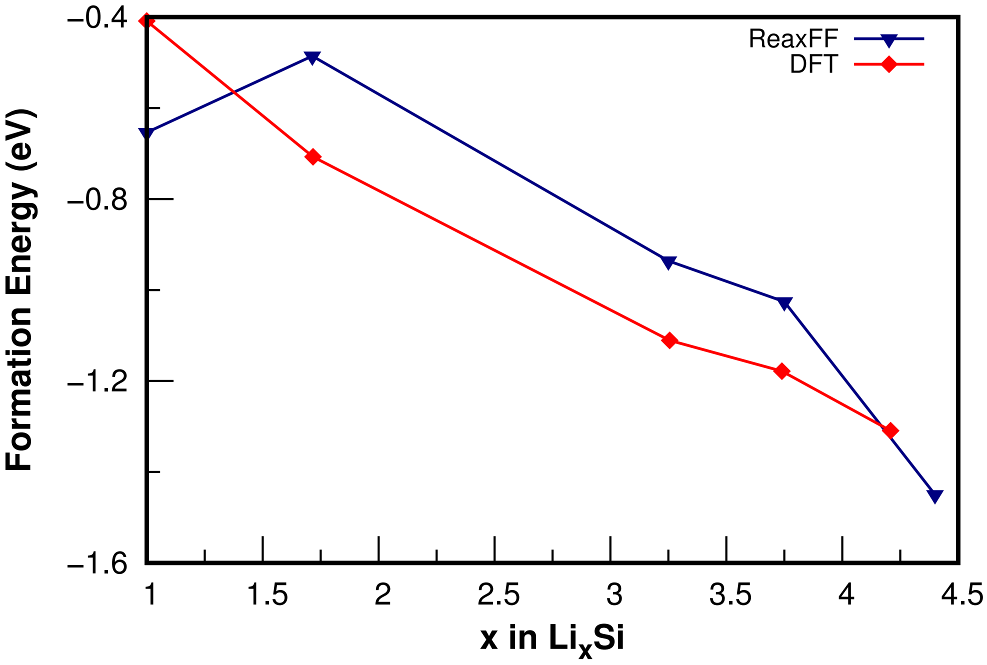

Figure 4.19 The formation energy of *c*-Li_xSi

doi:10.6342/NTU201703940

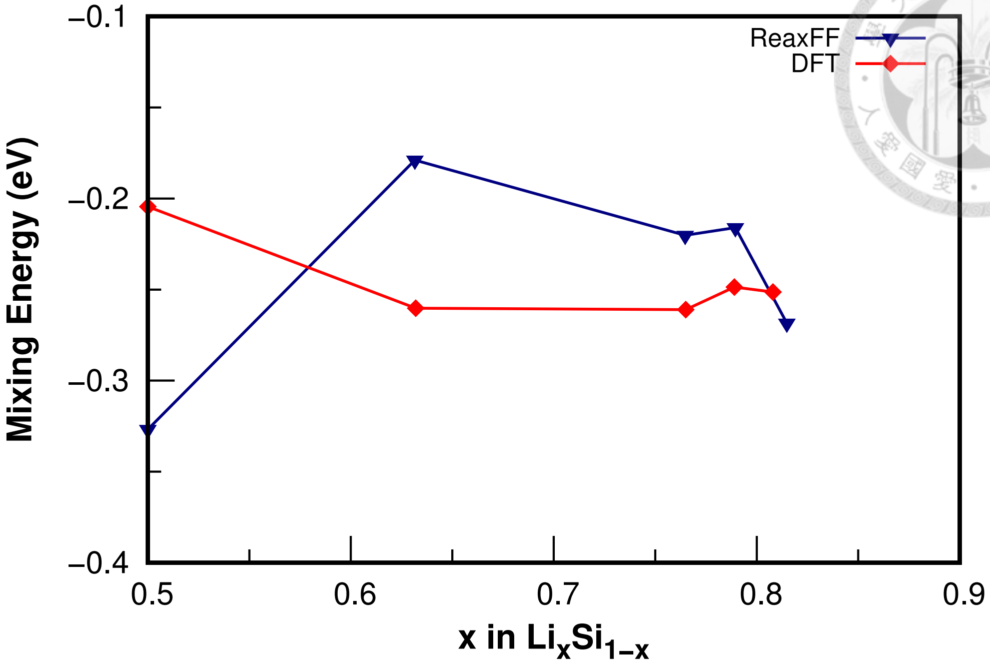

Figure 4.20 The mixing energy of *c*-Li_xSi

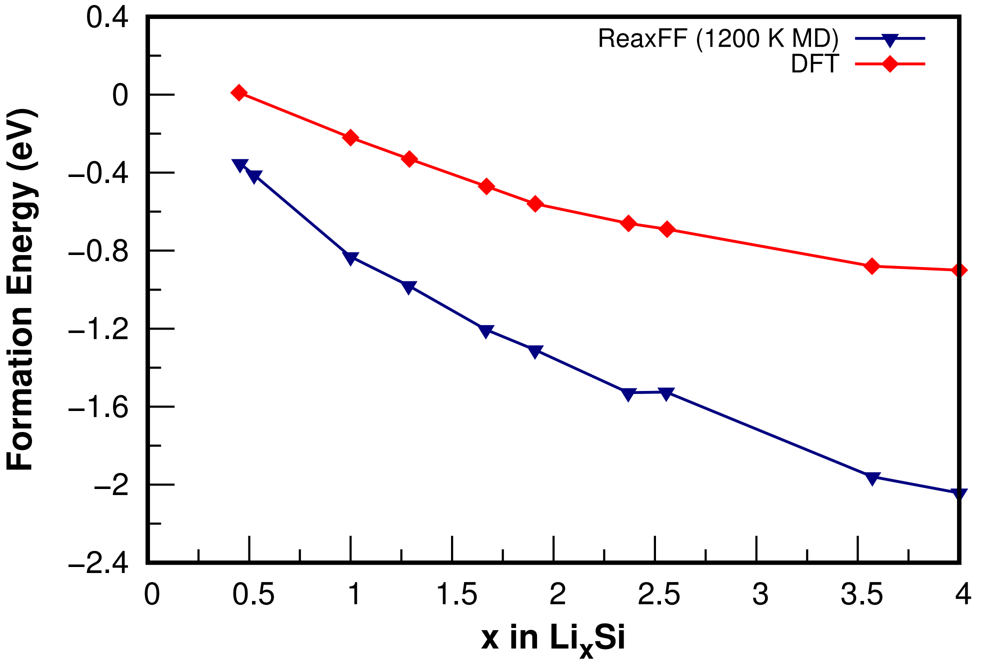

Figure 4.21 The formation energy of *a*-Li_xSi

doi:10.6342/NTU201703940

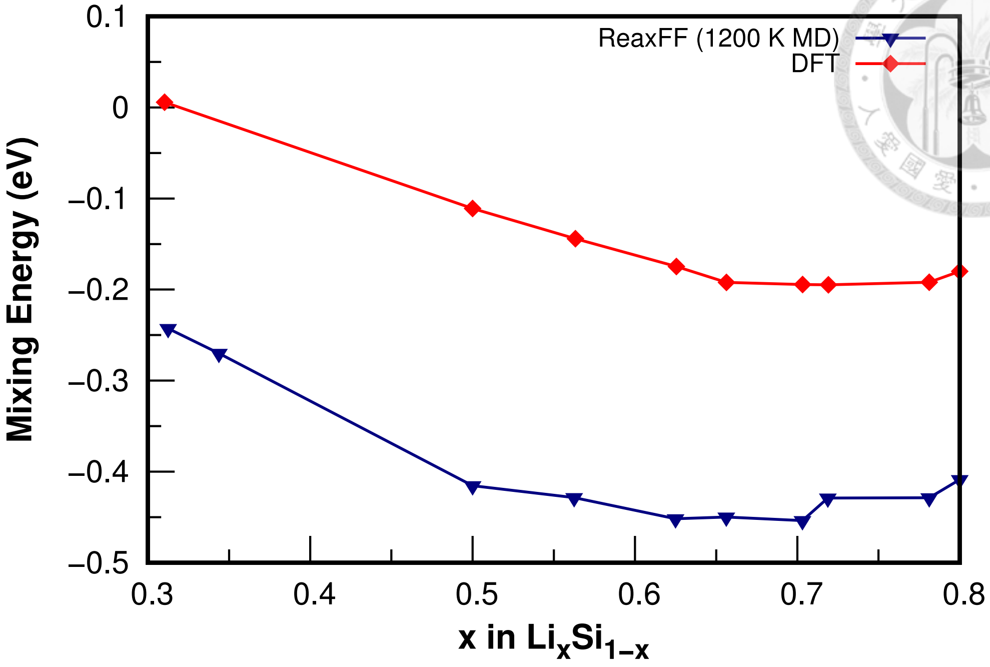

Figure 4.22 The mixing energy of *a*-Li_xSi

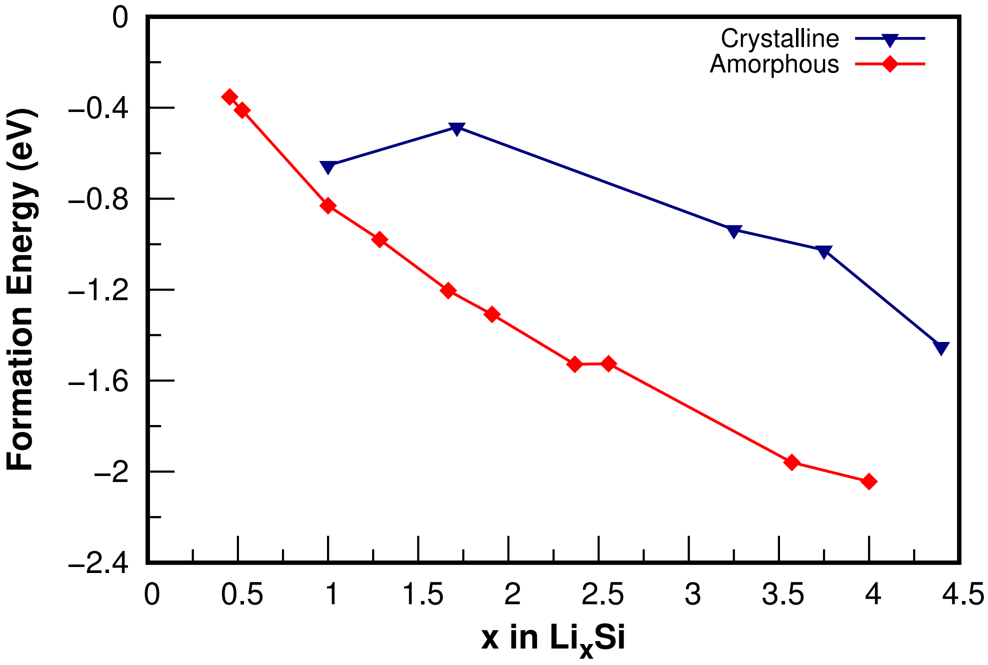

Figure 4.23 The formation energy comparison of amorphous and crystalline Li–Si alloys

doi:10.6342/NTU201703940

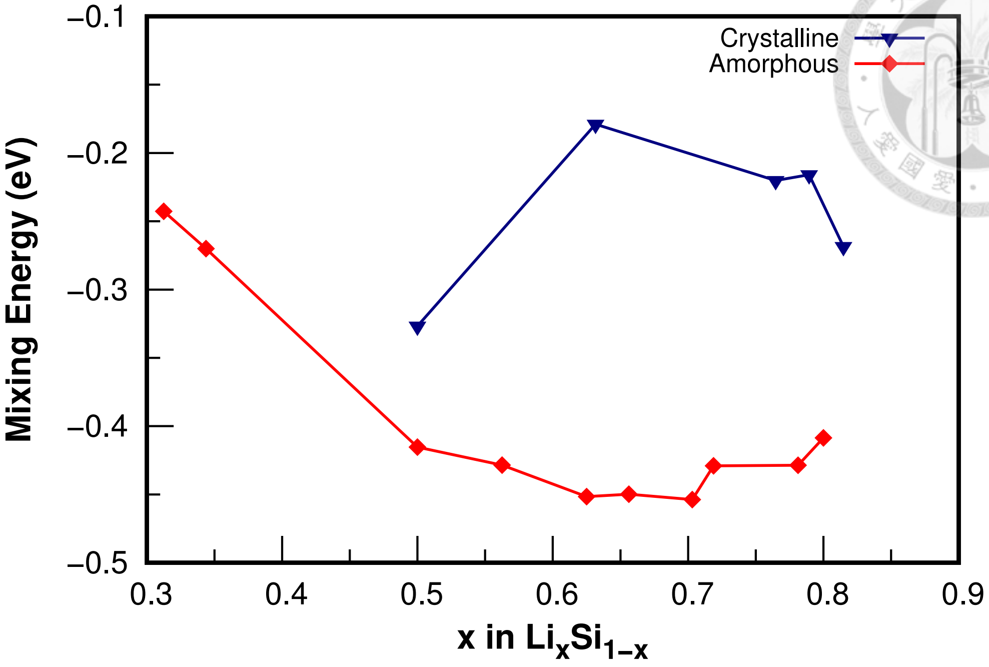

Figure 4.24 The mixing energy comparison of amorphous and crystalline Li–Si alloys

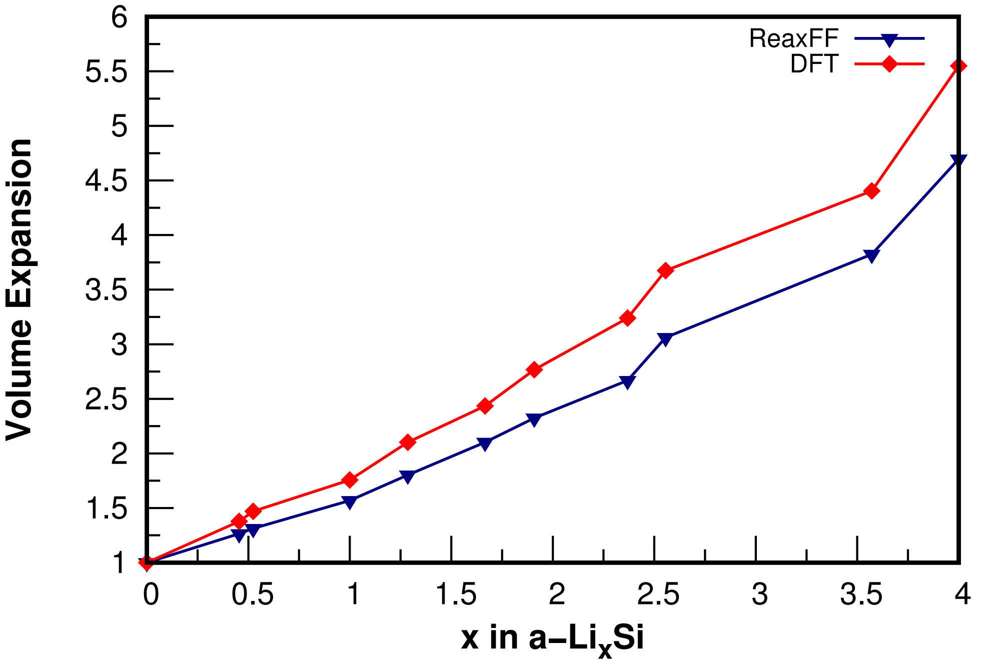

Figure 4.25 The volume expansion of *a*-Li$_x$Si

doi:10.6342/NTU201703940

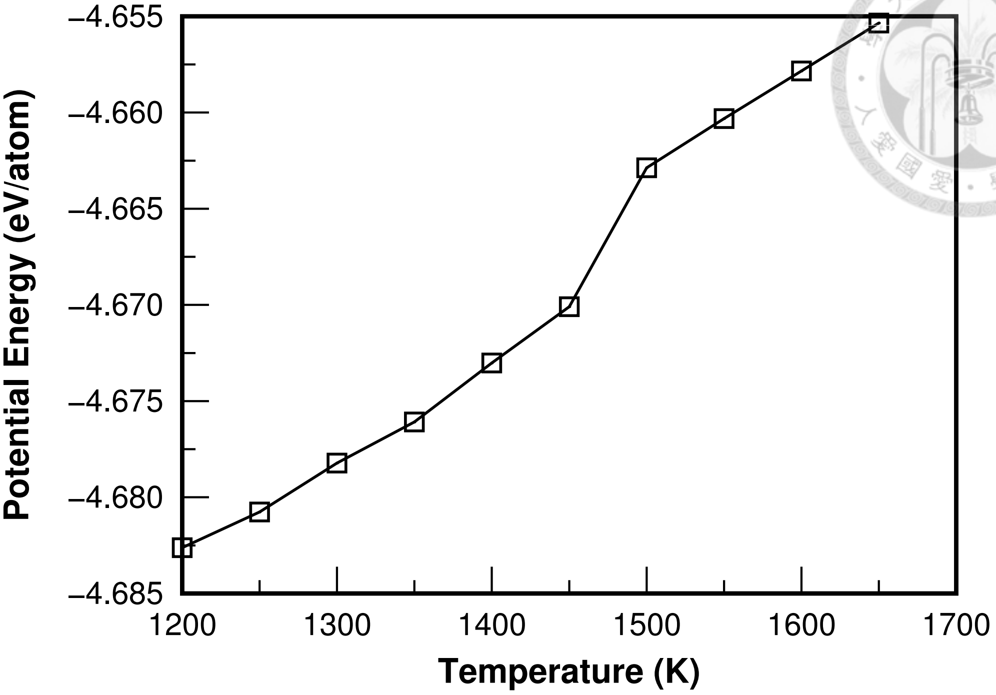

Figure 4.26 The melting point of Si

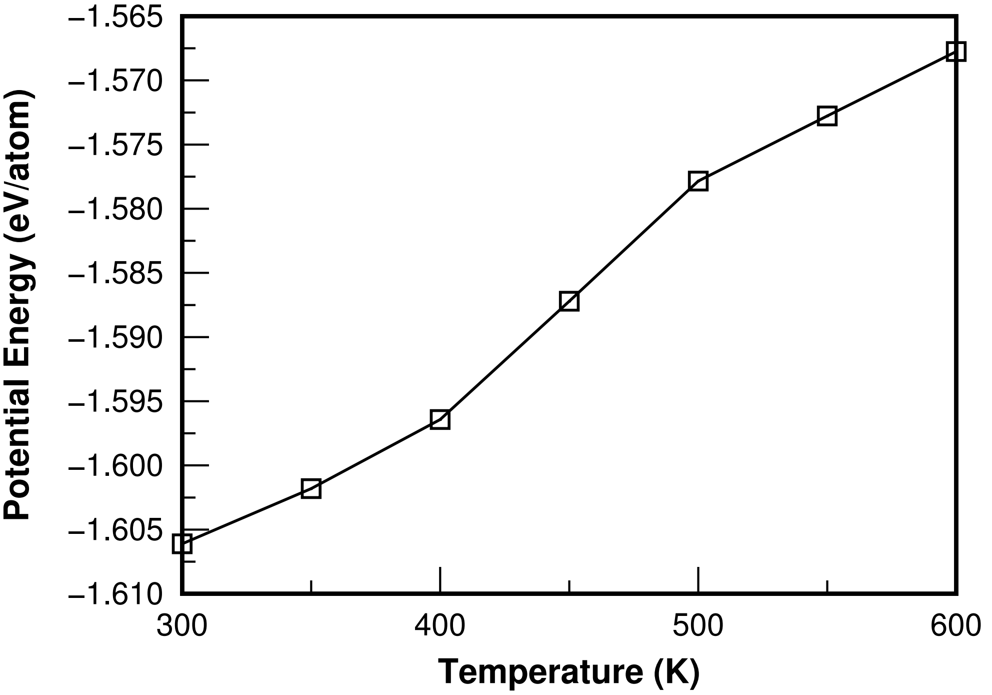

Figure 4.27 The melting point of Li

doi:10.6342/NTU201703940

4.4 Mechanical Properties

The bulk modulus, Young's modulus and shear modulus are calculated from table 4.8 to 4.11. The silicon has a lower stiffness tensor and lower modulus than DFT and the experimental values. The lithium has a similar modulus with the experimental data. However, some errors are found in the mechanical properties of Li–Si alloys.

	c_{11}	c_{12}	c_{44}
ReaxFF	110.69	47.48	36.37
SW	151.54	76.48	56.49
VASP	153.48	57.00	99.06
exp	166.0	64.0	79.6

Table 4.7 The calculated stiffness tensor in silicon (unit: GPa)

	G_{Voigt}	G_{Reuss}	G_{Hill}	B_{Voigt}	B_{Reuss}	B_{Hill}	E_{Voigt}	E_{Reuss}	E_{Hill}
ReaxFF	34.46	34.30	34.38	68.55	68.55	68.55	88.55	88.19	88.36
SW	48.91	47.00	47.95	101.50	101.50	101.50	126.42	122.14	124.28
VASP	64.13	61.27	62.70	89.16	89.16	89.16	155.18	149.55	152.37
exp	-	-	79.92	-	-	101.97	-	-	130.91

Table 4.8 The mechanical properties of *c*-Si (unit: GPa)

doi:10.6342/NTU201703940

	G_{Voigt}	G_{Reuss}	G_{Hill}	B_{Voigt}	B_{Reuss}	B_{Hill}	E_{Voigt}	E_{Reuss}	E_{Hill}
ReaxFF	6.62	6.01	6.31	10.84	10.84	10.84	16.49	15.22	15.86
DFT	7.0	2.2	4.6	13.67	13.67	13.67	17.94	6.26	12.41
exp	-	-	4.2	-	-	11.6	-	-	4.9

Table 4.9 The mechanical properties of *c*-Li (unit: GPa)

	G_{Voigt}	G_{Reuss}	G_{Hill}	B_{Voigt}	B_{Reuss}	B_{Hill}	E_{Voigt}	E_{Reuss}	E_{Hill}
ReaxFF	22.24	20.96	21.60	66.73	66.72	66.73	60.06	56.92	58.49
DFT	35.87	33.02	34.44	52.11	51.99	52.05	87.52	81.76	84.66

Table 4.10 The mechanical properties of *c*-LiSi (unit: GPa)

	G_{Voigt}	G_{Reuss}	G_{Hill}	B_{Voigt}	B_{Reuss}	B_{Hill}	E_{Voigt}	E_{Reuss}	E_{Hill}
ReaxFF	9.03	7.99	8.51	14.11	14.11	14.11	22.33	20.16	21.25
DFT	23.20	19.70	21.45	29.67	29.67	29.67	55.21	48.38	51.85

Table 4.11 The mechanical properties of *c*-$Li_{15}Si_4$ (unit: GPa)

4.5 Nudged Elastic Band calculation of lithium diffusion in crystalline silicon

In order to catch the dynamical properties in ReaxFF, we have to calculate the energy barrier of lithium diffusion in crystalline silicon for validation. The calculated path is shown as in figure **4.28**, while the calculated energy barrier of lithium diffusion in silicon is 0.50 eV. This is similar to the 0.58 eV by van Duin *et al.* and the DFT value 0.65 eV. We can conclude good agreement with the literatural value.

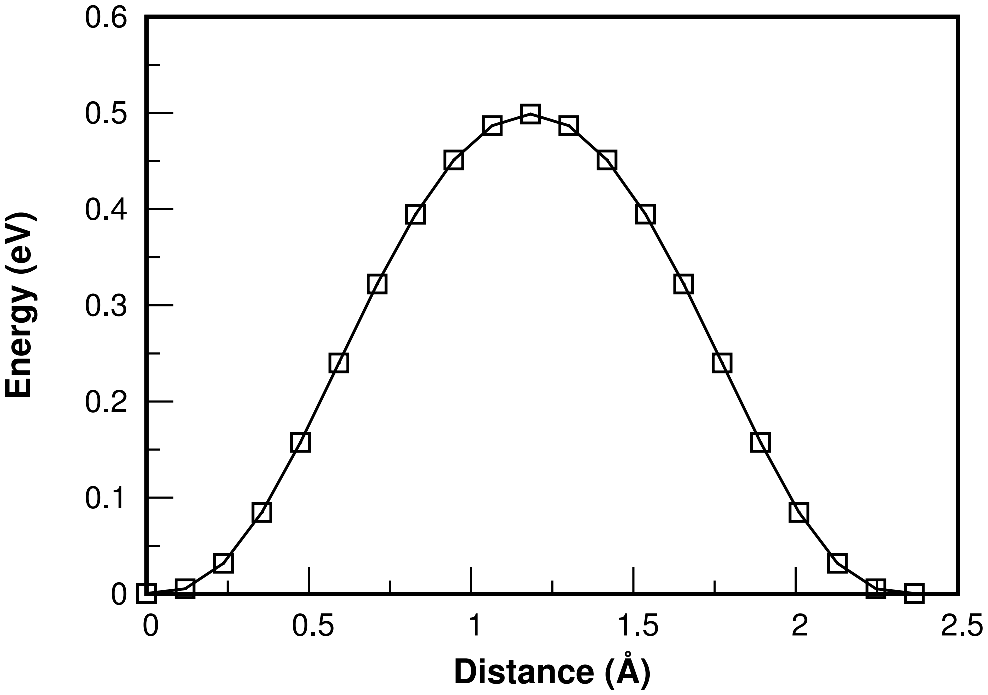

Figure 4.28 The energy barrier of Li diffusion in Si by ReaxFF in this study

doi:10.6342/NTU201703940

4.6 Summary

The ReaxFF$_{\text{LiSiAlO}}$ used in this thesis can reproduce the properties of crystal and amorphous structures well at 0 K calculation (energy minimization only). However, there are some problem in the description of the relative stability in the crystal and amorphous structures. We have found that the amorphous Li–Si alloy is more stable than the crystalline counterparts, which is in contradiction with experimental results. Besides, when using molecular dynamics simulations, the crystal structure is unstable and prone to collapse even at low temperature as 300 K, which again shows the instability of the crystal structure. In addition, the Si lattice constant of 5.32 Å at 1200 K also shows the instability. However, some of the properties as the RDF, formation and mixing energy and volume expansion for amorphous Li–Si alloys done by molecular dynamics equilibration shows good agreements with DFT results.

doi:10.6342/NTU201703940

國立臺灣大學
敬業 樂群 愛國 愛人

doi:10.6342/NTU201703940

CHAPTER 5 Silicon lithiation rate comparison

5.1 Structure of silicon

The silicon has a diamond structure as in figure **5.1**. It has a Fd$\bar{3}$m symmetry, which means it has a glide plane along $\langle 110 \rangle$ direction (diamond glide). Therefore the Si$\langle 110 \rangle$ is a good direction for observing the silicon structure. The stereographic projection is another useful tool for determining the direction. Different facets that will be used in this study are shown in figure.**5.2**

The lithium will insert in the tetrahedral (T_d) site. When Li diffuses, it will move from one *tetrahedral* site to *hexagoanl* site as intermediate, then move to another *tetrahedral* site. Besides, the T_d site of Li interstitial in Si forms another diamond structure **5.3**. This is useful in determining the position of Li in Si and its diffusion path.

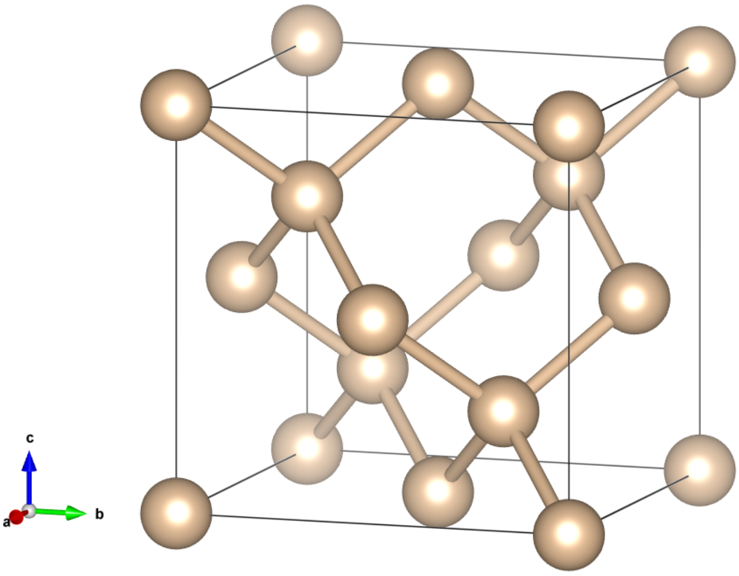

Figure 5.1 The silicon structure

doi:10.6342/NTU201703940

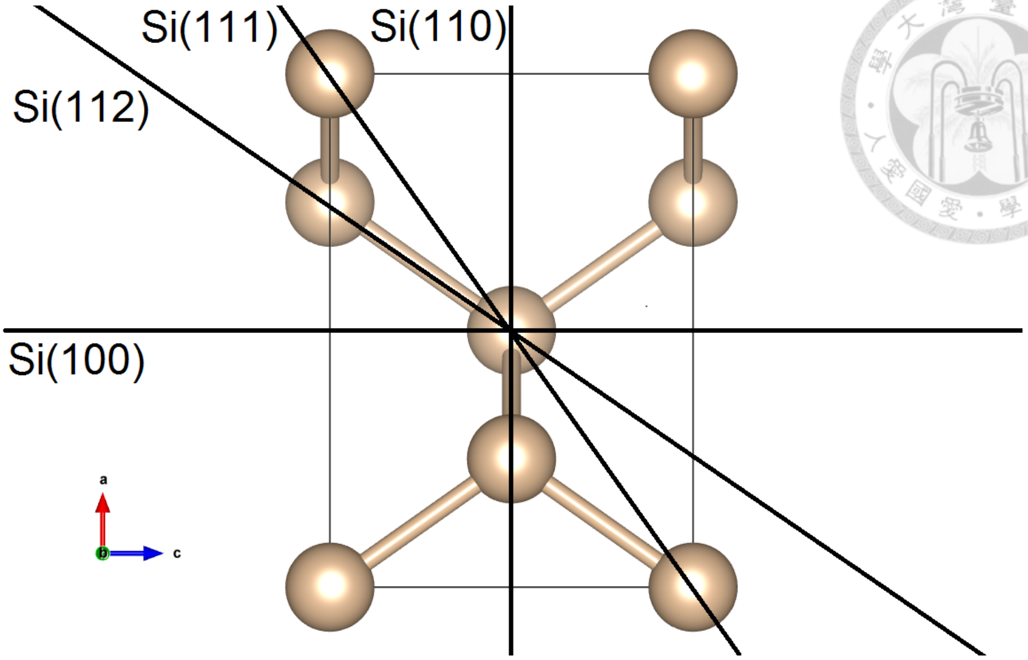

Figure 5.2 The facets viewed along [110]

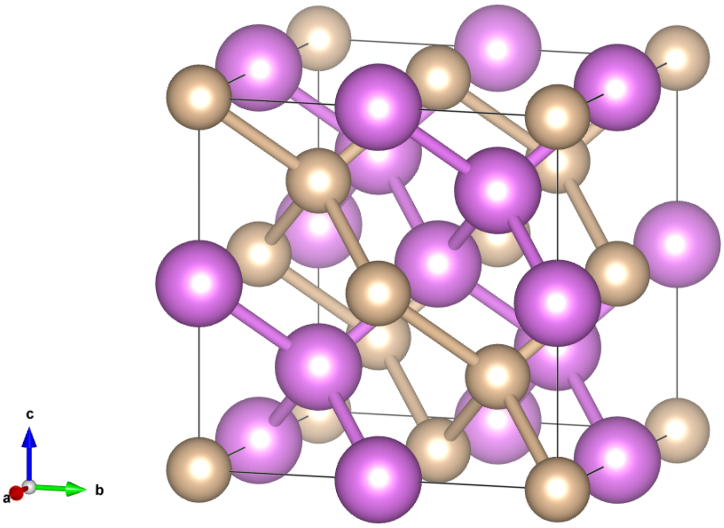

Figure 5.3 The silicon and the lithium in all T_d site. The silicon is in ivory color while the lithium is in pink. The lithium should not be connected since there are no covalent bonding between them. The Li–Li connection is only used to show the duality of the silicon and lithium structure and the diffusion path of lithium in silicon.

5.2 Computational Details

In this part, we used the Si(100), Si(110), Si(111) and Si(112) slab with Li up above it in NVT 800 K, 1000 K and 1200 K for lithiation. The initial conditions are shown in figure **5.4**. For the silicon slab, we have used the silicon with lattice constant 5.4635 Å, which is the equilibrium lattice constant we found by optimization in the previous section. The silicon slab has the following dimensions

	a (Å)	b (Å)	c (Å)	size	# atoms
Si (100)	38.632782	38.632782	98.343000	10×10×18	7200
Si (110)	38.244500	38.632782	100.445232	7×10×26	7280
Si (111)	38.632782	40.148334	94.6306351	10×6×10	7200
Si (112)	38.632782	37.852254	100.370835	10×4×15	7200

Table 5.1 Dimensions of the Si slab used in this simulation (20 Å vacuum layer for surface structure simulation is excluded from the table)

The initial structure of lithium is in BCC, which has the dimensions and density shown as below. It was later equilibrated in 1200 K as described in the next paragraph. In this case, we have chosen the density of BCC lithium in room temperature.

	density (low) (#/Å^3)	lattice constant (low) (Å)	geom. mean (Å)	size	# atoms
Si (100)	0.04629	3.51207×3.51207×3.50257	3.50890	11×11×74	17908
Si (110)	0.04629	3.47677×3.51207×3.53813	3.50890	11×11×74	17908
Si (111)	0.04629	3.51207×3.64985×3.37035	3.50890	11×11×74	17908
Si (112)	0.04629	3.51207×3.44114×3.57476	3.50890	11×11×74	17908

Table 5.2 Dimensions of the Li slab used in this simulation

The silicon slab is reconstructed by slightly moving the atoms off the equilibrium position. After that, the structure are relaxed by the Stillinger-Weber potential [37] and then relaxed again by the ReaxFF potential. The lithium slab is first equilibrated at 1200 K for 20 ps and then relaxed. The silicon and lithium slab are joined together and relaxed again for the most stable surface structure. Later, the lithiation is carried out in NVT at the temperature of 800, 1000 and 1200 K to observe the lithiation bahavior. The computational settings are shown in figure **5.4**.

5.3 Analysing Details

In this study, the lithiation process is separated by the front and back of the phase boundary. We have defined the **back** of the phase boundary as the coordination number of silicon = 3.5, while the front has the phase boundary of the concentration $X_{\mathrm{Si}} = 0.99$. The back layer is the position that the phase boundary transform to the a-$\mathrm{Li_xSi}$. The front layer is the deepest layer that Li can penetrate into. In our study, we have calculated the lithiation velocity of the back in steady state by linear fitting.

In addition to the steady state velocity, we have also calculated the stress in the phase boundary. We have divided the stress outputted from LAMMPS by the Voronoi volume, which is a built-in package. This step is important or it will generate the stress in wrong order. Next, we averaged the stress by finite difference on the z-direction with $\Delta z = 1$ Å. We calculated the *principal in-plane stress*, which is calculated by solving the eigenvalue problem in x-, y-direcion and it is defined as below:

$$\sigma = \frac{\sigma_{xx} + \sigma_{yy} \pm \sqrt{(\sigma_{xx} - \sigma_{yy})^2 + (2\sigma_{xy})^2}}{2} \tag{5.1}$$

We choose the one with the largest absolute value as the *maximal principal in-plane stress*, which is more important than the minimal in-plane stress in my discussion.

doi:10.6342/NTU201703940

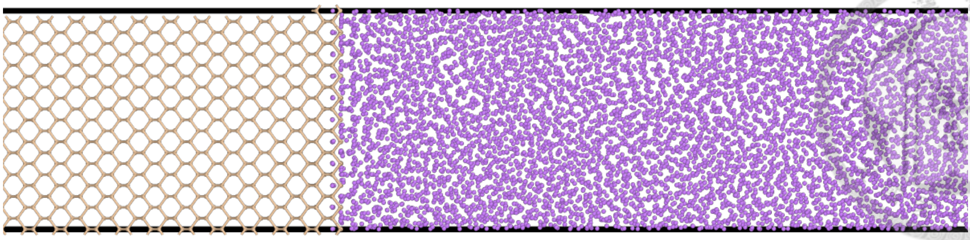

Si(100)

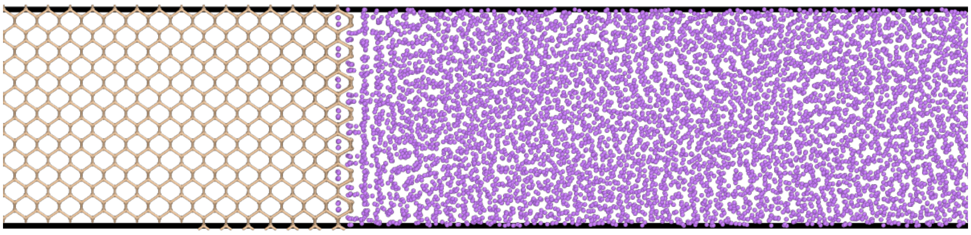

Si(110)

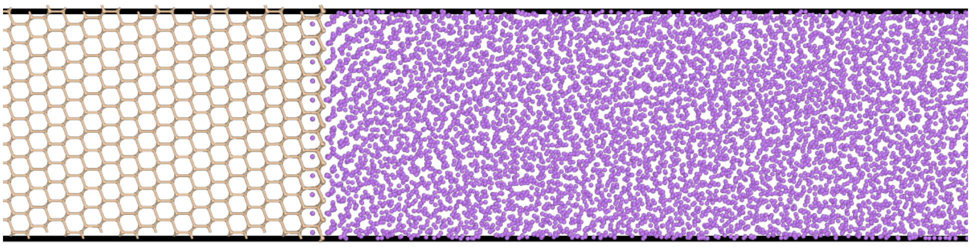

Si(111)

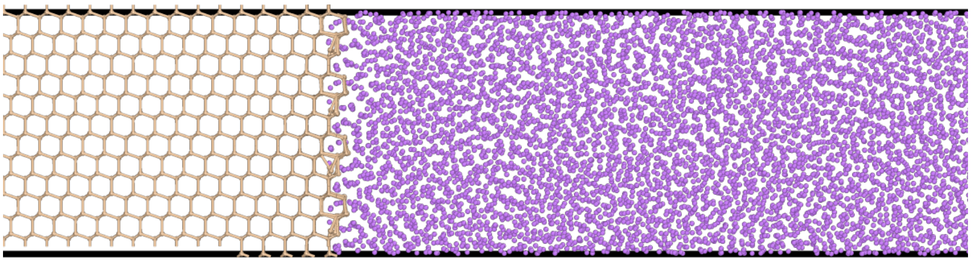

Si(112)

Figure 5.4 The silicon with lithium slab used in this study

5.4 Results

5.4.1 Structural Observations in the Lithaition Mechanism

The lithiation snapshost are shown in figure **5.5**. The phase boundary is again observed in our simulation. The calculated radial distribution function (RDF) (figure **5.6**, **5.7**, **5.8**) are compared with Kim *et al.*'s result (figure **5.9**). We can observe similar peak positions in our result and Kim *et al.*'s result.

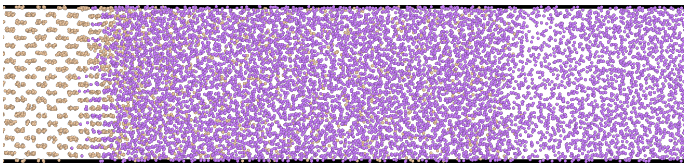

Si(100)

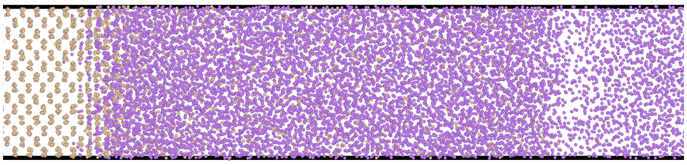

Si(110)

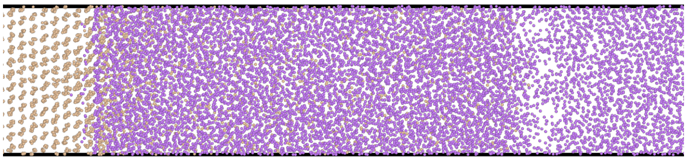

Si(111)

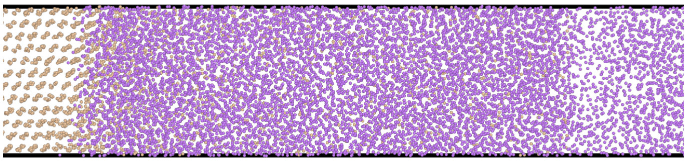

Si(112)

Figure 5.5 The lithiation in NVT 1000 K at 100 ps.

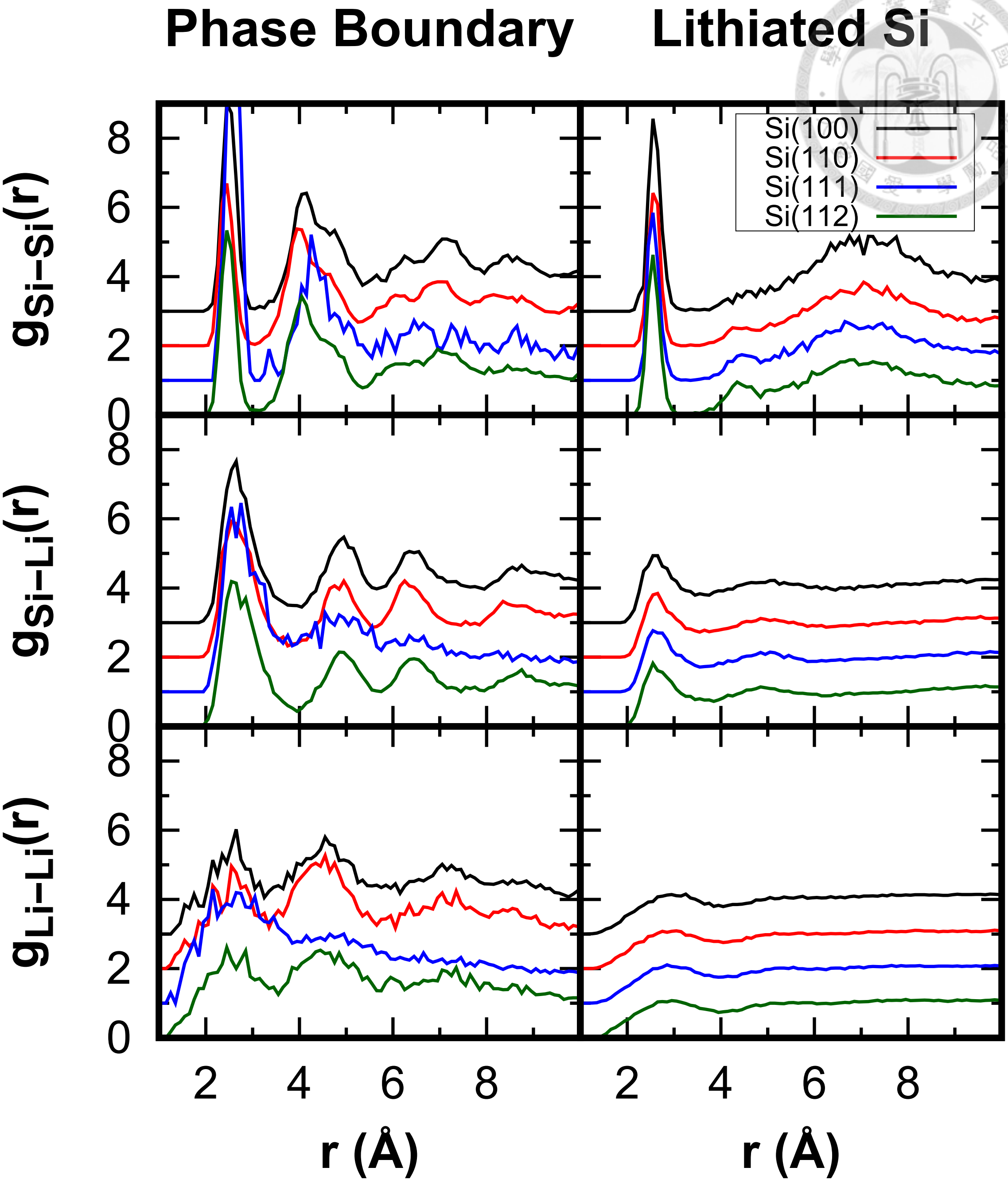

Figure 5.6 The RDF 800 K result

doi:10.6342/NTU201703940

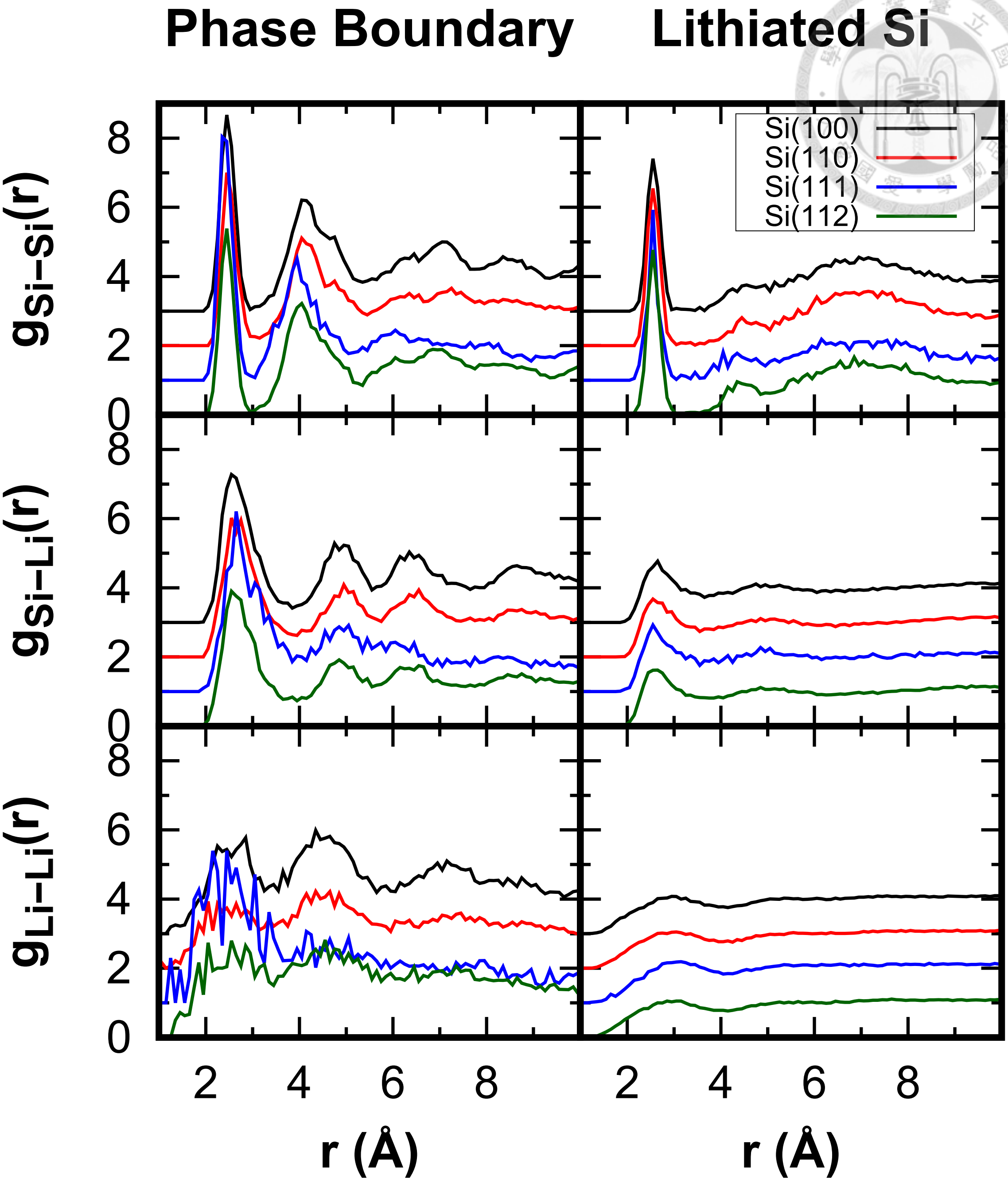

Figure 5.7 The RDF 1000 K result

doi:10.6342/NTU201703940

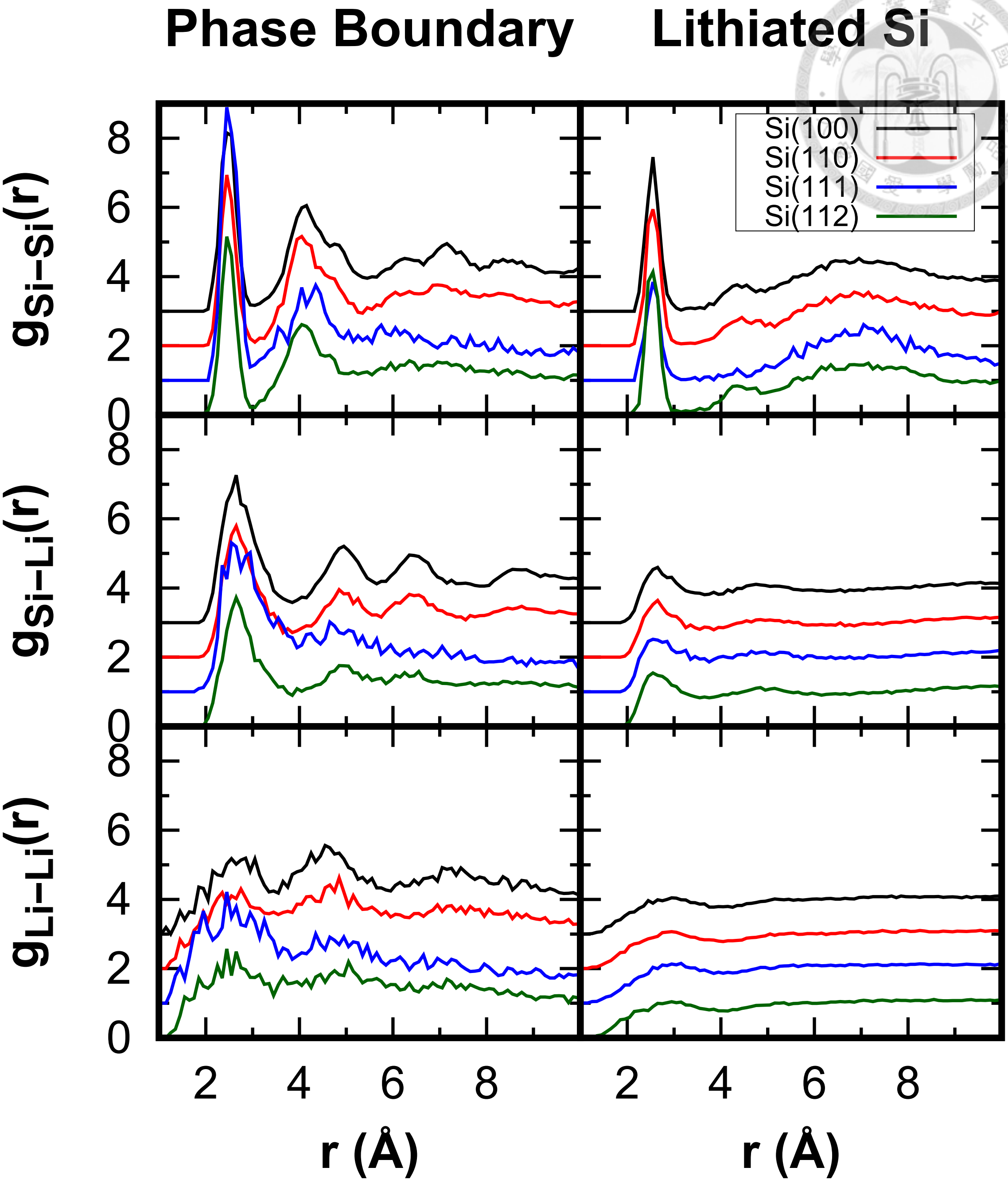

Figure 5.8 The RDF 1200 K result

doi:10.6342/NTU201703940

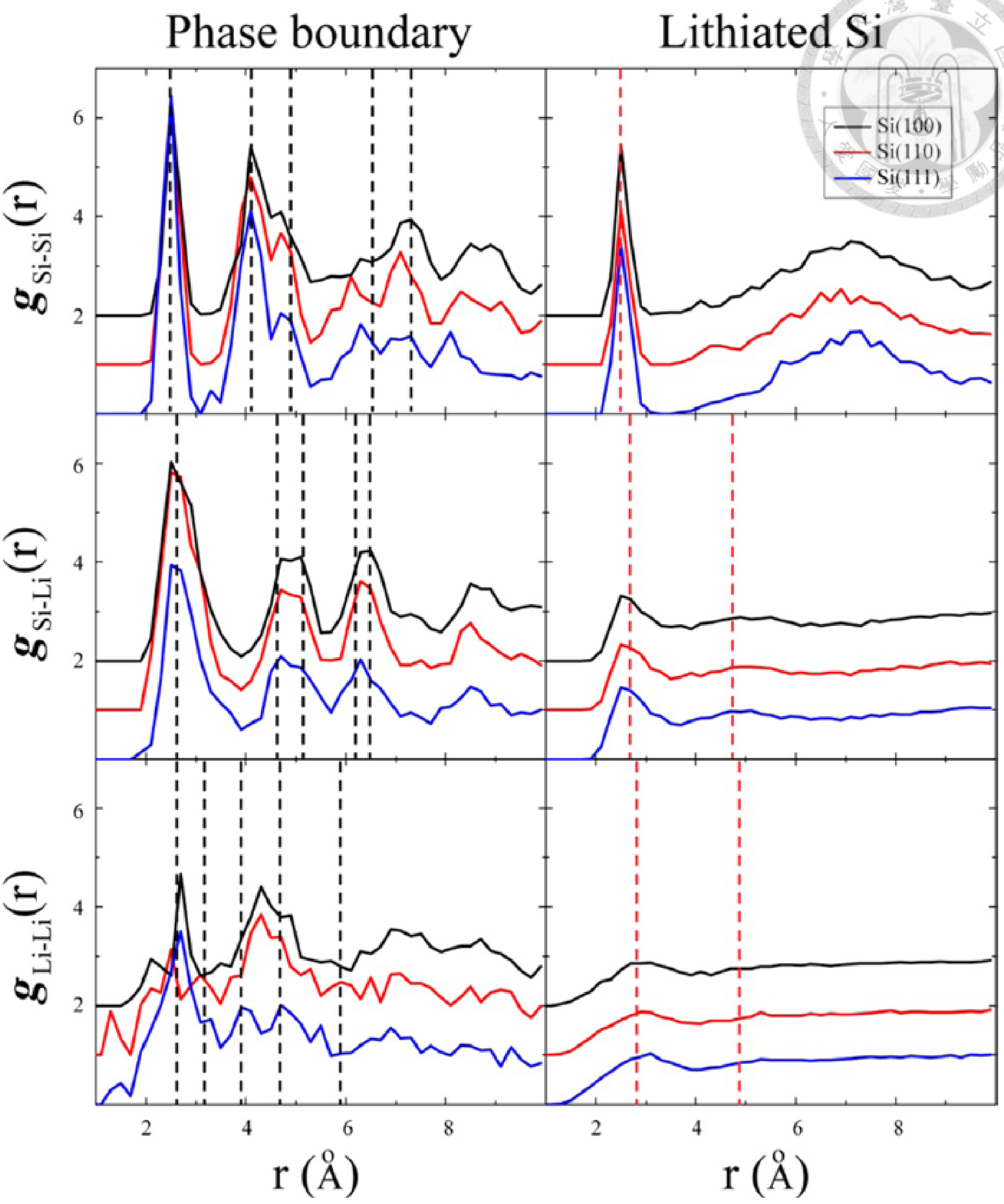

Figure 5.9 Kim's *et al.* result of RDF in lithiation

doi:10.6342/NTU201703940

5.4.2 Lithiation Rates in Different Facets

The NVT lithiation rate in each facet is calculated in table **5.3**, while the phase boundary thickness is calculated in table **5.4**. We have showed similar phase boundary thickness of about 1 nm with respect to the experiment. A general trend is that the phase boundary increases with the temperature. In the case of 800 K, we have reproduced the anisotropy described in the experiment that Si(110) have the highest lithiation rate. However, we did not fully reproduce the anisotropy which has about 3 times than other facet as described in Astrova *et al.*'s experiment.[38] We expect that the simulation at a lower temperature may be able to achieve it.

		800 K	1000 K	1200 K
Si(100)	CN=3.5	62.1	76.0	89.0
	X=0.5	66.8	80.0	100.0
Si(110)	CN=3.5	78.7	83.0	87.7
	X=0.5	79.0	92.0	101.6
Si(111)	CN=3.5	67.3	82.7	94.6
	X=0.5	69.0	83.0	105.7
Si(112)	CN=3.5	56.1	85.0	94.1
	X=0.5	70.0	99.8	110.1

Table 5.3 The NVT lithation rate comparison (unit: Å/ns)

The temperature dependence on the anisotropy shows different activation energy of the facets, as shown in figure **5.10**. The lithiation rate of Si(110) does not depend much on the temperature than other facets, which shows that Si(110) has a lower activation energy barrier than other facets. Therefore, the kinetic control of the lithiation anisotropy is confirmed.

We want to further investigate the cause of the difference between each facets. There

doi:10.6342/NTU201703940

		800 K	1000 K	1200 K
Si(100)	CN=3.5	11.74	11.55	12.88
	X=0.5	10.16	10.36	10.53
Si(110)	CN=3.5	9.57	10.89	11.68
	X=0.5	9.38	10.28	11.79
Si(111)	CN=3.5	5.15	6.33	7.06
	X=0.5	4.01	5.56	5.90
Si(112)	CN=3.5	9.30	10.21	9.49
	X=0.5	8.73	9.44	9.57

Table 5.4 The NVT phase boundary thickness comparison (unit: Å)

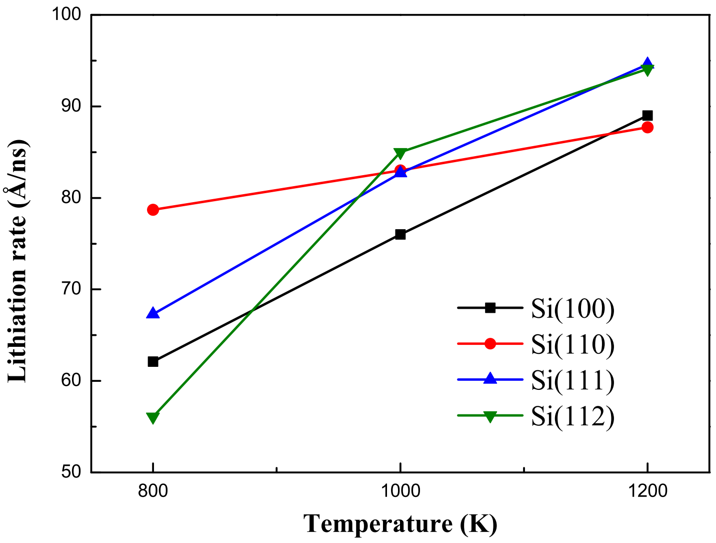

Figure 5.10 The temperature dependence on the lithiation rate difference

are 2 critical factors in lithiation: lithium insertion rate into the silicon and the rate of Si–Si bond breaking which transform the phase boundary layer into *a*-Li_xSi. Since the Li concentration should be the same in all facets, and the Si–Si bond breaking rate is proportional to the Li concentration in the surface. Thus the critical issues should be the

doi:10.6342/NTU201703940

lithium insertion rate. The structure in different facets should have different effect on the energy barrier in lithium insertion rate. For example, in Cubuk *et al.*'s paper, their results show a lower insertion energy barrier in Si(110) than in Si(100). This can support our hypothesis that the insertion energy barrier difference can cause the anisotropy that we reproduced at NVT 800 K.

In addition to the energy barrier calculation in silicon, the difference can also be explained by the insertion energy barrier of germanium. Germanium has the same diamond crystal structure as silicon, but it has higher lattice constant of 5.66 Å than 5.43 Å in silicon. Besides, the lithium insertion in germanium has a much lower energy barrier than silicon. While the anisotropic expansion has not been observed in germanium. We also suggest that it is the low energy barrier of lithium insertion in germanium that makes the lithium diffuse isotropically in all direction. When the energy barrier is low enough, the lithium atom will be energetic to overcome the insertion energy barrier in all facets. However, when the energy barrier is high and have some anisotropy in different facets, the energy barrier in some of the facets will be overcome while the others are not. This will cause the anisotropic insertion preference and therefore cause the anisotropy.

The high temperature case as at NVT 1200 K shows higher lithiation velocity in Si(111) facet. We can apply the energy barrier difference to explain this phenomena. When the Li insertion energy barrier into all facets are overcome, the lithiation rate should be similar. However, there are some fundamental difference in the surface structure in each facets. The Si(111) facet has the highest surface atom density as 15.66 atoms/nm^2, which should be double as mentioned in Kim *et al.*'s result[12]. The main cause of this difference is that a layer of Si(111) surface has 2 sublayers with very little interspacing. Kim *et al.* might have calculated 1 sublayer as its density. However, when lithiation, the *two* sublayers are lithiated *simultanesously* and therefore they should be calculated as *one* combined layer. Since

doi:10.6342/NTU201703940

silicon has a cubic-F Bravais lattice and it should have Si(111) as its close-packing plane. A higher interspacing of Si(111) combined layer should be expected. When the insertion energy barrier are overcome in all facets, the higher interspacing and higher surface density in Si(111) means when 1 layer of silicon is lithiated, the further the phase boundary will advance and more silicon will be lithiated. This can explain the higher lithiation rate of Si(111) than other facets that we observed in higher temperature.

Comparing with Kim *et al.*'s result at 1200 K. They have the similar result that Si(110) fails to be the fastest lithiation facet, therefore cannot reproduce the anisotropic expansion fully. They have used a weighted lithiation rate by multiplying the lithiation velocity with the surface density for explanation. However, this is not entirely correct since it is experimentally observed that the phase boundary in Si(110) should have the highest lithiation velocity instead of the weighted lithiation rate.

5.4.3 Stress analysis in silicon slab

We have performed the stress analysis as in Jung *et al.*'s paper. The stress profile is shown in the appendix. It can be observed that the compressive stress in the phase boundary *decreases* when the temperature increases. Besides, the phase boundary moving rate is much faster in higher temperature. The stress calculated here includes the thermo stress. Therefore the stress in the phase boundary should *increases* if the temperature increases.

5.4.4 Lithiation Rates in Silicon Nanowires

In addition to the silicon slab lithiation, We have performed the silicon nanowire lithiation in 800 K NVT case. We have reproduced the anisotropy in Si[110] nanowire and Si[100] nanowire. This is shown in figure **5.11**, **5.12**. The anisotropy that we have reproduced in nanowire case is much more obvious than in the slab case, indicating different mechanism for anisotropy.

doi:10.6342/NTU201703940

Besides, We have also performed the nanowire lithiation in 600 K NPT, as shown in figure **5.13**. Our results show that the silicon structure hardly lithiates since the temperature is too low. However, the phase boundary interaction will be easier to observe. We can see that the Si(110) has a much larger phase boundary than Si(100) and Si(111). The high insertion rate in Si(110) facet may cause a faster phase boundary formation and induce compressive stress on the other facets and thus suppress the phase front in other facets. The anisotropy in the nanowire might be enhanced due to this compressive stress difference in each facet.

In addition, we have tested the nanowire lithition in 300 K NPT with *z*-axis fixed with 1% compressive strain and *x*-, *y*-direction using NPT in compressive stress. We have reproduced the anisotropy in **5.14** as describe in Jung *et al.*'s study, even though different parameters are used. This is the best anisotropic lithiation that we have reproduced so far.

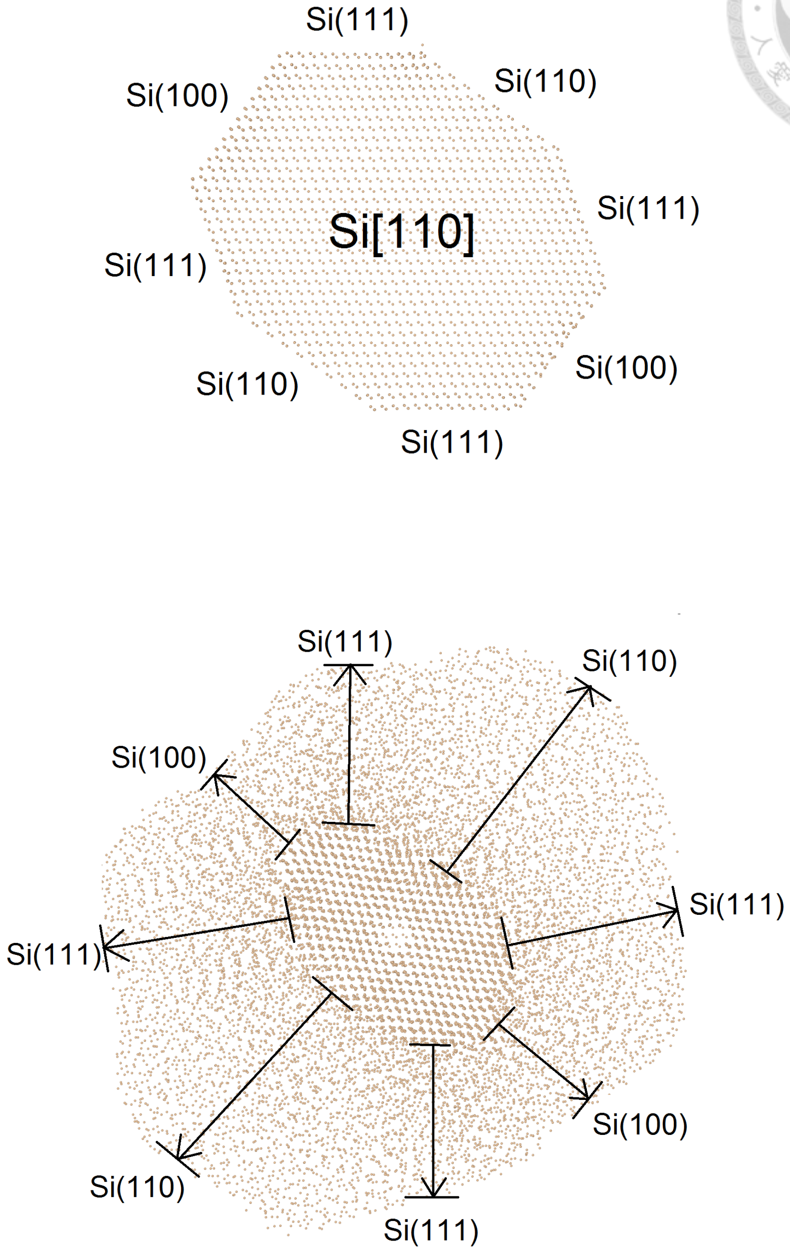
Si(111)
Si(100)
Si(110)
Si[110]
Si(111)
Si(111)
Si(110)
Si(100)
Si(111)
Si(111)
Si(110)
Si(100)
Si(111)
Si(111)
Si(100)
Si(110)
Si(111)

Figure 5.11 The anisotropy is reproduced in the Si[110] nanowire. The silicon is removed for clarity. The subfigure above shows the orignial settings while the subfigure below shows the nanowire after 72 ps. The anisotropy is reproduced.

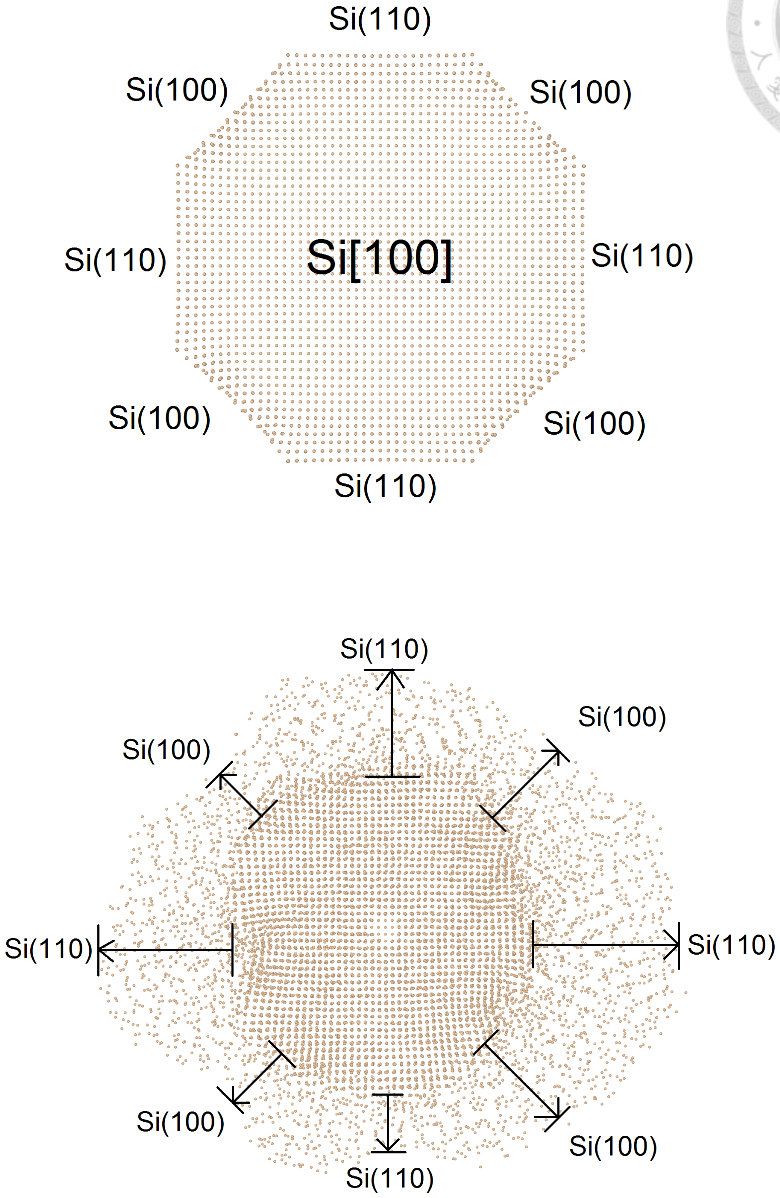
Si(110)
Si(100)
Si(100)
Si(110)
Si[100]
Si(110)
Si(100)
Si(100)
Si(110)
Si(110)
Si(100)
Si(100)
Si(110)
Si(110)
Si(100)
Si(100)
Si(110)

Figure 5.12 The anisotropy is also reproduced in the Si[100] nanowire. The silicon is removed for clarity. The subfigure above shows the original settings while the subfigure below shows the nanowire after NVT 160 ps. The anisotropy is reproduced.

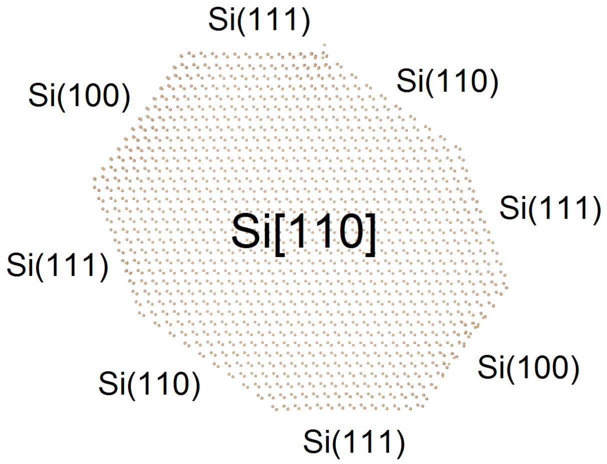
Si(111)
Si(100)
Si(110)
Si(111)
Si[110]
Si(111)
Si(110)
Si(100)
Si(111)

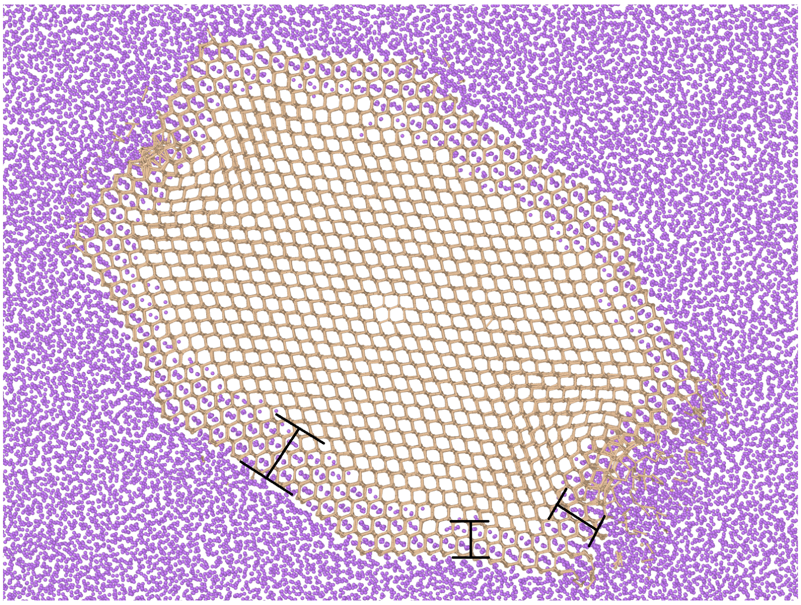

Figure 5.13 The Si[110] nanowire in NPT 600 K. The structure hardly lithiates. Si(110) has much larger phase boundary than other facets.

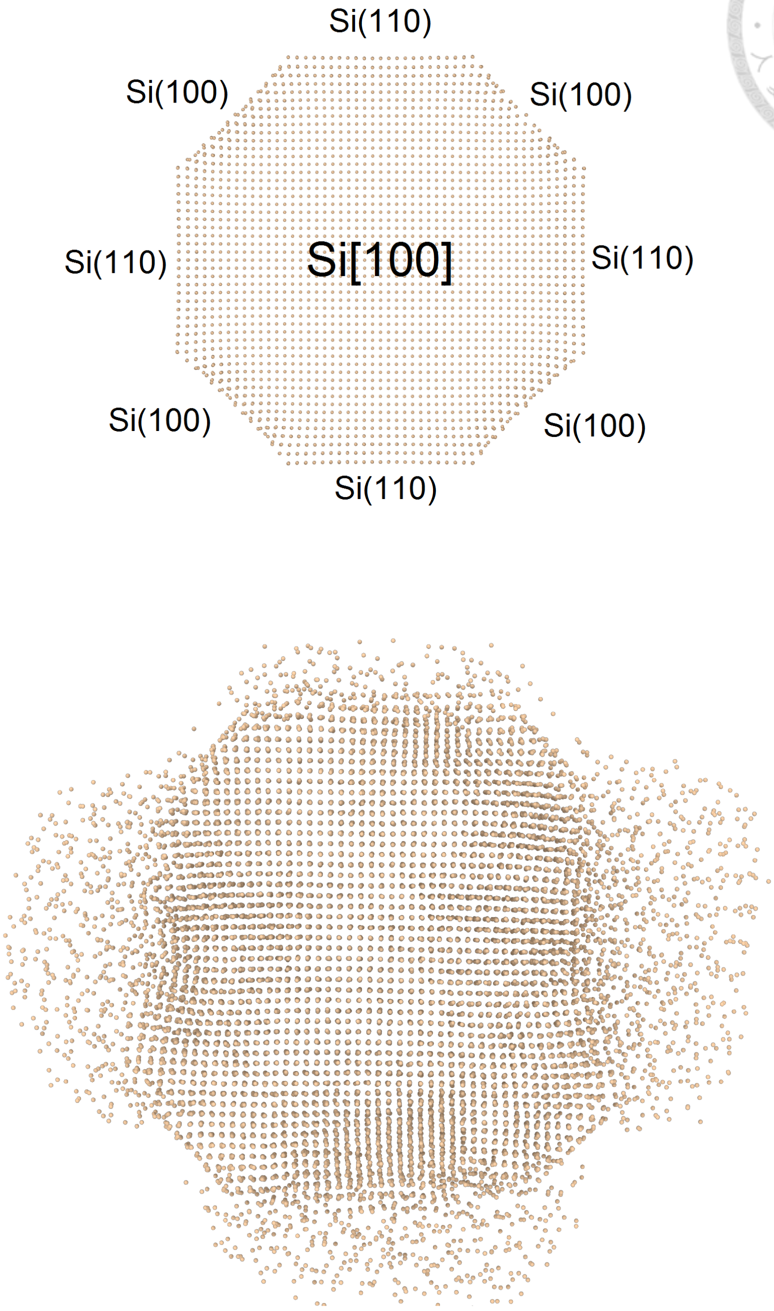
Si(110)
Si(100)
Si(100)
Si(110)
Si[100]
Si(110)
Si(100)
Si(100)
Si(110)

Figure 5.14 The anisotropy is also reproduced in the Si[100] nanowire. The silicon is removed for clarity. The subfigure above shows the original settings while the subfigure below shows the nanowire after NPT 300 K 74.2 ps. with z-direction fixed and adding compressive stress on the x- and y-direction

doi:10.6342/NTU201703940

5.4.5 Some Problems in this Study

Despite the fact that we cannot fully reproduce the anisotropy observed in the experiment, there are still some points to be checked.

First, the NVT conditions that we have used will have some problem in the lithiation since the concentration of Li in the lithiated a-Li$_x$Si is higher than pure Li. This will make lithium deficit in the later stage of lithiation. Besides, LAMMPS have recommended that the period of temperature control to be 100 times of the timestep and pressure control to be 1000 times of the timestep. Since we have used the timestep of 0.2 fs. This will make the period of temperature control to be 20 fs while the one for pressure control to be 200 fs. This kind of control is too frequent and might induce some undesirable results, such as the formation of some unstable region. For example, if the unstable region occurs in Si(100), it will be vulnerable to lithiate and might become the fastest lithiation facet in the simulation, even though it should have a lower lithiation rate than Si(110).

We have found that there are some problem in the ReaxFF in the previous chapter. We have observed that in NVT 1200 K, the lattice constant of silicon is calculated as 5.32 Å while it is 5.46 Å in fully optimization. It is weird that silicon can have a lower lattice constant in NVT 1200 K than in 0 K optimization. Therefore, we have used the 5.46 Å as the lattice constant of silicon in our study. If the lower lattice constant is true in higher temperature, This will induce tensile stress in the silicon cell since the lattice constant of 5.46 Å is in tensile condition.

Besides, we have found some problem in LAMMPS's source code when reproducing the EV curve. This part is shown in the appendix. After doing some correction we can get smoother energy volume curve as we observed in the previous chapter. However, this part is not corrected in the source code released most recently.

doi:10.6342/NTU201703940

We have tried the NPT 600 K lithiation to check if Si(110) can have a higher lithiation rate than Si(111) at lower temperature. However, the silicon hardly lithiates and only shows 3 lithiated atoms after 600 ps simulations. The NVT case also hardly lithiates.

5.4.6 Future Study

By getting the succeed of the nanowire anisotropic lithiation, we have some experiences and opinions about our future research. First, if the anisotropy should be reproduced, **the temperature should be low enough** (< 600 K) since high temperature will make the silicon structure vulneraable to break and make lithiation easy in all facets, which will result in nearly isotropic lithiation. Besides, since the temperature are low, the lithiation reaction will be hard to achieve since there are no electric field as driving force in our study. Therefore a **high density of Li** or a **compressive pressure** on the lithiation direction should be imposed. We have planned to use a z-direction compressed slab for our future study.

In addition the problems mentioned in the previous subsection should also be solved, which we have summarized as below:

- The NVT and NPT thermostat and barostat control period problem.
- Lower lattice constant in higher temperature as NVT 1200 K.
- The energy discontinuity problem in the source code.

doi:10.6342/NTU201703940

doi:10.6342/NTU201703940

CHAPTER 6 Conclusions

We have performed a ReaxFF molecular dynamics simulation in LAMMPS using the $\text{ReaxFF}_{\text{LiSiAlO}}$ from Ostadhossein *et al.*. At first, we have carried out the silicon slab lithiation like Kim *et al.* in NVT within 800, 1000 and 1200 K. We have reproduced the lithiation anisotropy in 800 K, but it is not obvious. We hypothesized that this is due to the Li insertion energy barrier difference between each facet. The Si(110) has the lowest Li insertion energy barrier and thus its lithiation rate does not change much at lower temperature.

On the other hand, we have performed silicon nanowire lithiation at NVT 800 K and shows anisotropy. Although it does not fit exactly the same as the experiment, the phase boundary layer thickness developed at 600 K also shows some anisotropy in the phase boundary thickness. A larger thickness is found in Si(110) than other facets. This may induce compressive stress on other facets and slows down the lithium insertion rate. In addition, the best anisotropy that we have reproduced is at 300 K NPT case while Si(100) has almost no lithiation, which is in good agreement with experimental results.

However, we have found some problems in the ReaxFF, such as the energy discontinuity, the anomalous lattice constant at high temperature. In addition, the thermostat and barostat controlling time will induce some artificial effect on the dynamical behavior, which might cause some facets other than Si(110) to have the highest lithiation rate. These problems should be solved for further study.

At last, we have tested many other configurations as NPT and 600 K lithiation. However, neither of these conditions really works. In the future study, the lower temperature simulation will be used in order to mitigate the structural instability of silicon induced by high temperature. Because of the low lithiation rate at low temperature, we want to use

doi:10.6342/NTU201703940

the higher Li concentration or lithiation direction compressed NPT ensemble to speed up the lithiation.

CHAPTER 7 Appendix

7.1 Changes in order to make the energy volume curve smoother

The original LAMMPS reaxc program and default bonded and non-bonded cutoff in LAMMPS will generate some break-points. Therefore, we have modified the program in the parameter validation section. This may produce a smoother energy volume curve and therefore a smoother energy surface, which is crucial in molecular dynamics study. The detailed change is listed below:

- **Numbonds criteria**

  In the LAMMPS mailing list, somebody have questioned the same energy volume curve problem as in https://github.com/lammps/lammps/issues/. They have commeted out the if condition in `reaxc_multi_body.cpp:71, 82, 90, 191, 206, 212` like

  ```
  if(numbonds > 0)
  ```

  We have applied this modification to eliminate the break-point in my energy volume curve. However, it has little help in my break-point.

- **Mass criteria in reaxc of ReaxFF**

  This criteria is not found in the original ReaxFF paper by van Duin. We have done some search and found that it is for the correction of first-row elements as C, N, O, F. However, we did not found Li as a correction target. It has the following correction criteria in `reaxc_multi_body.cpp:133` and `reaxc_bond_orders.cpp:579`

  ```
  if( sbp_i->mass > 21.0 ){part I}else{part II}
  ```

  since the criteria is for 1st row-element, which has mass smaller than 21. We want to disable this correction, which means Li will have the same treatment as non-first-row element. Therefore, we commented out the criteria and leaves part I only.

- **Cutoff for bonded and nonbonded calculations.**

  We have found that the default bonded and non-bonded cutoff as 5 Å and 10Å respectively will introduce some break-points in the energy volume curve. Since the 3rd nearest neighbor in Li metal is about 5 Å and its effect can not be ignored, the *bonded* cutoff should be a bit larger than this value. The default non-bonded cutoff of 10 Å will also induce break-points in energy volume curve for *c*-$Li_{12}Si_7$. Therefore, we used the bonded and non-bonded cutoff as 6 Å and 12 Å in my parameter validation study.

7.2 The stress profile in the lithiation

In the following page, we will show the maximal principal stress, hydrostatic stress for reference. It can be observed that in higher temperature, the stress developed in the phase boundary is much lower than the low temperature case.

doi:10.6342/NTU201703940

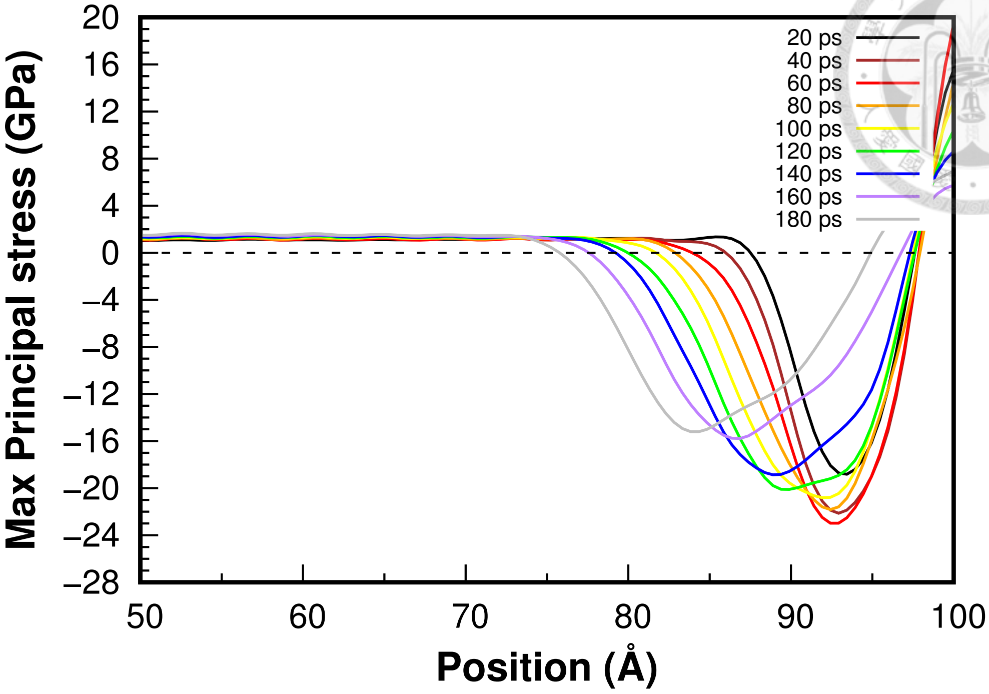

Figure 7.1 The Si(100) maximum principal stress in NVT 800 K

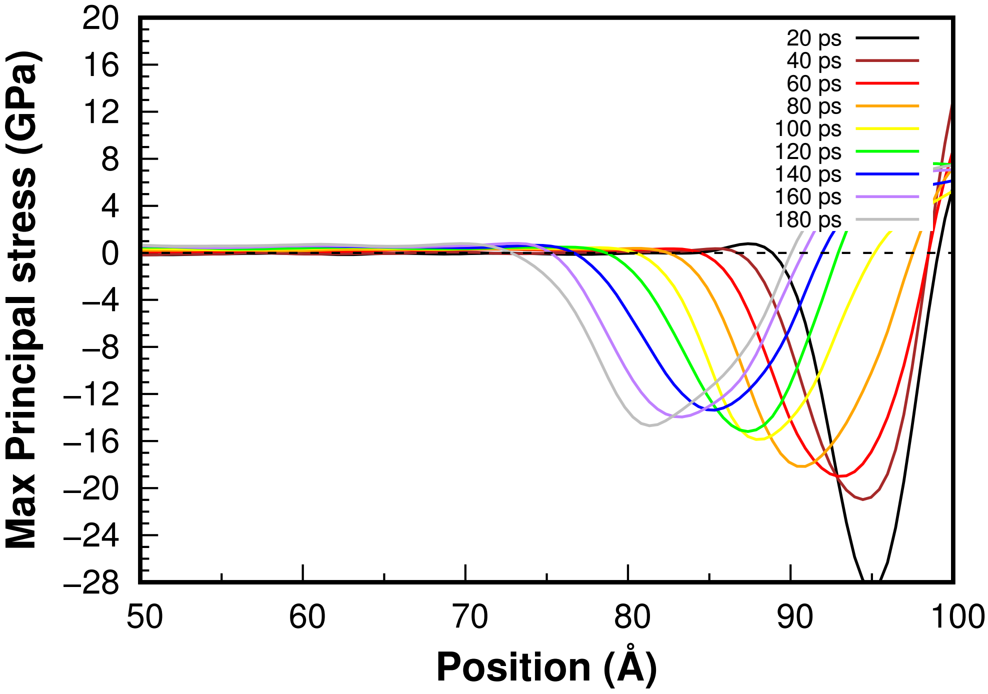

Figure 7.2 The Si(110) maximum principal stress in NVT 800 K

doi:10.6342/NTU201703940

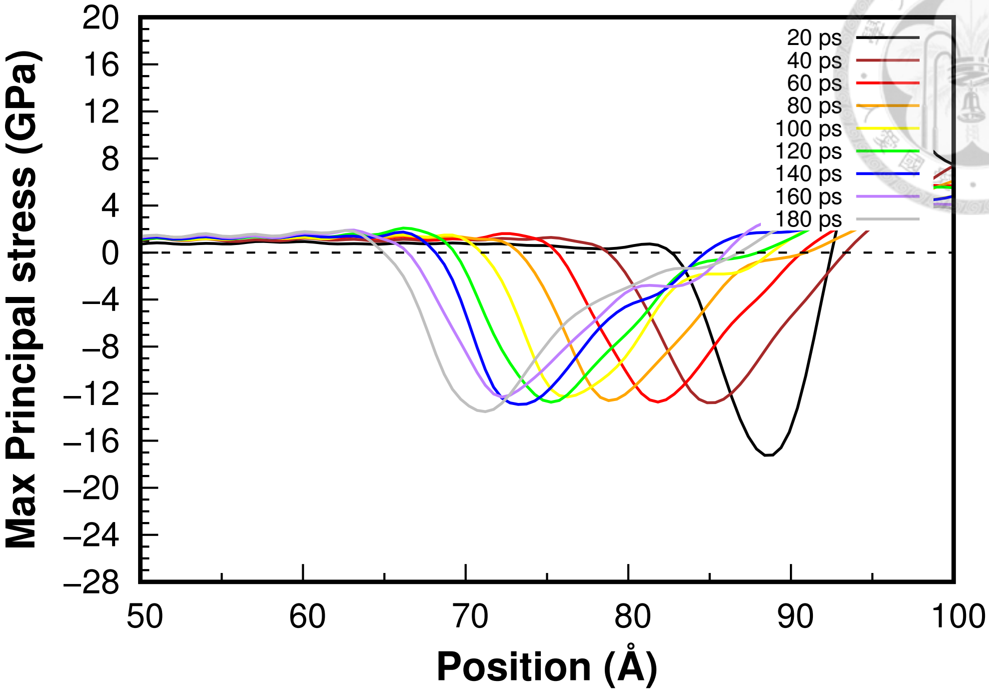

Figure 7.3 The Si(111) maximum principal stress in NVT 800 K

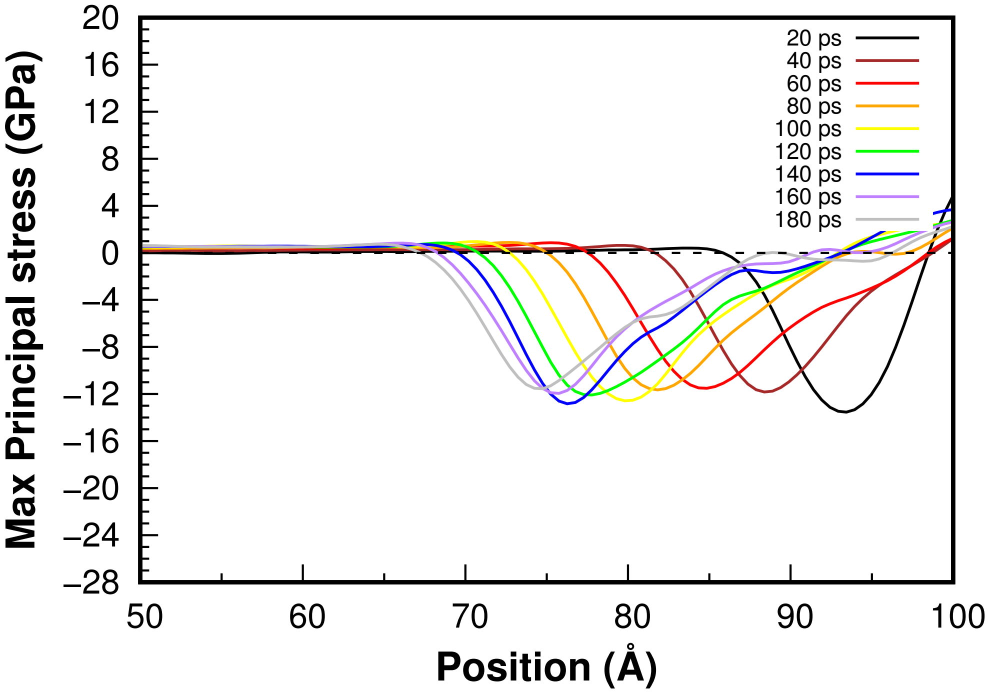

Figure 7.4 The Si(112) maximum principal stress in NVT 800 K

doi:10.6342/NTU201703940

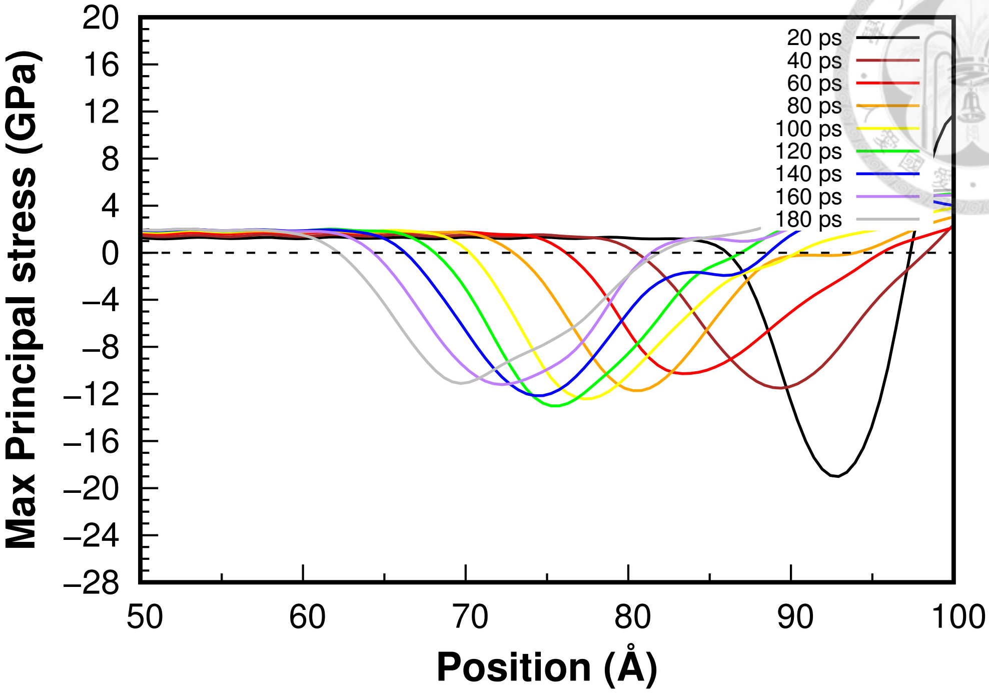

Figure 7.5 The Si(100) maximum principal stress in NVT 1000K

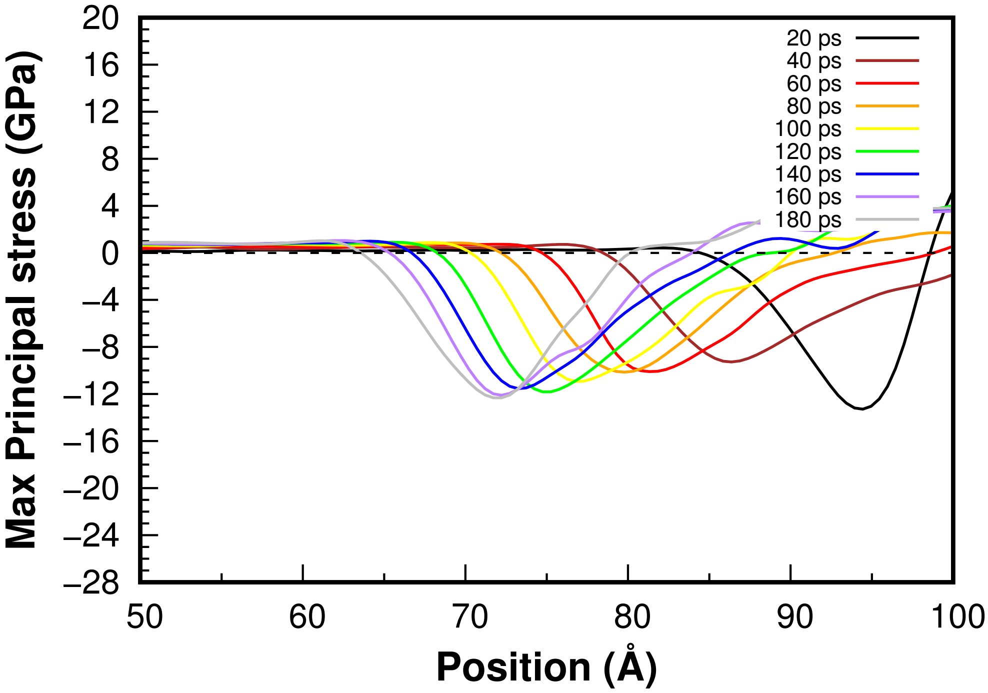

Figure 7.6 The Si(110) maximum principal stress in NVT 1000K

doi:10.6342/NTU201703940

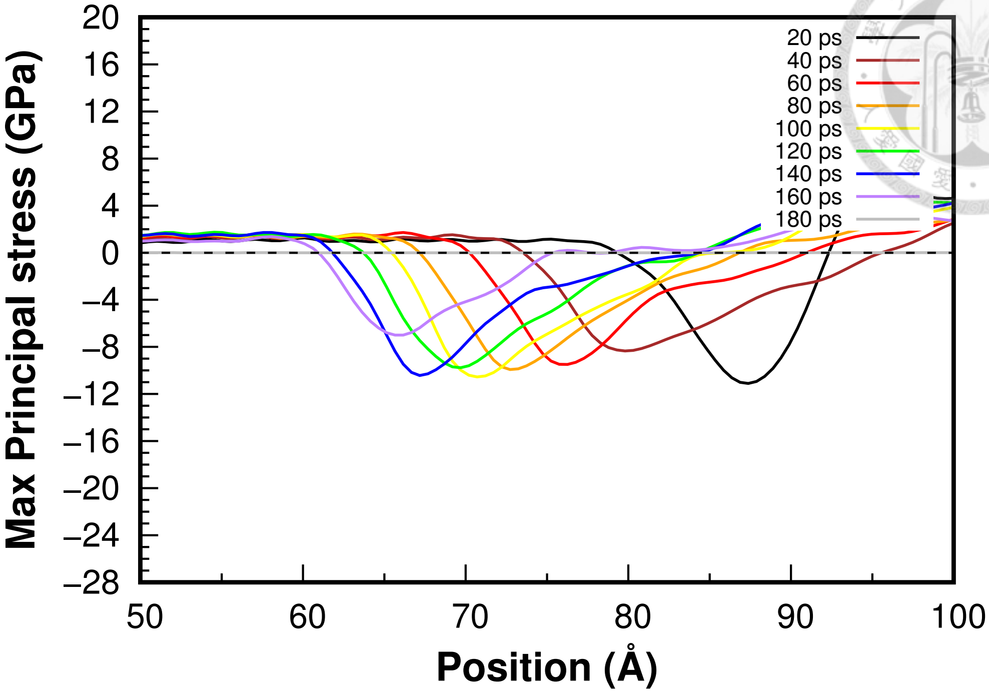

Figure 7.7 The Si(111) maximum principal stress in NVT 1000K

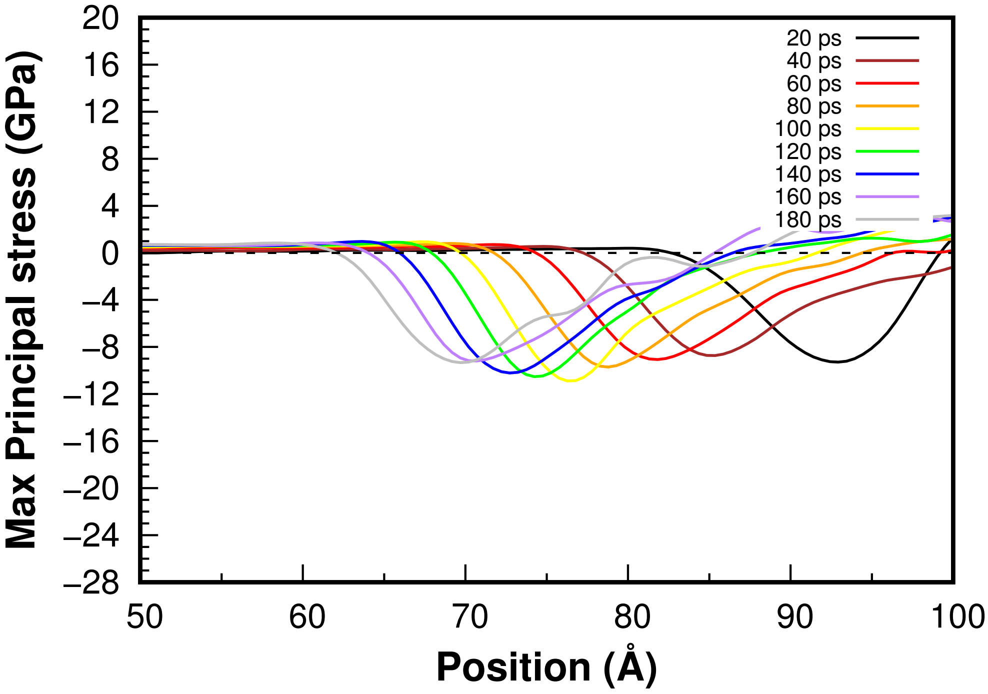

Figure 7.8 The Si(112) maximum principal stress in NVT 1000K

doi:10.6342/NTU201703940

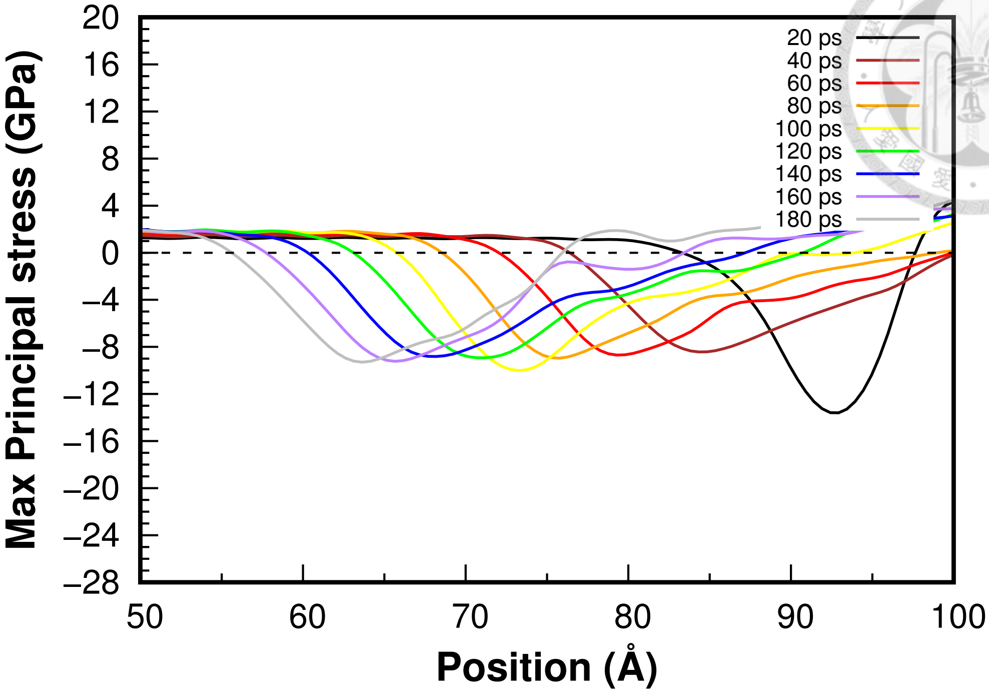

Figure 7.9 The Si(100) maximum principal stress in NVT 1200K

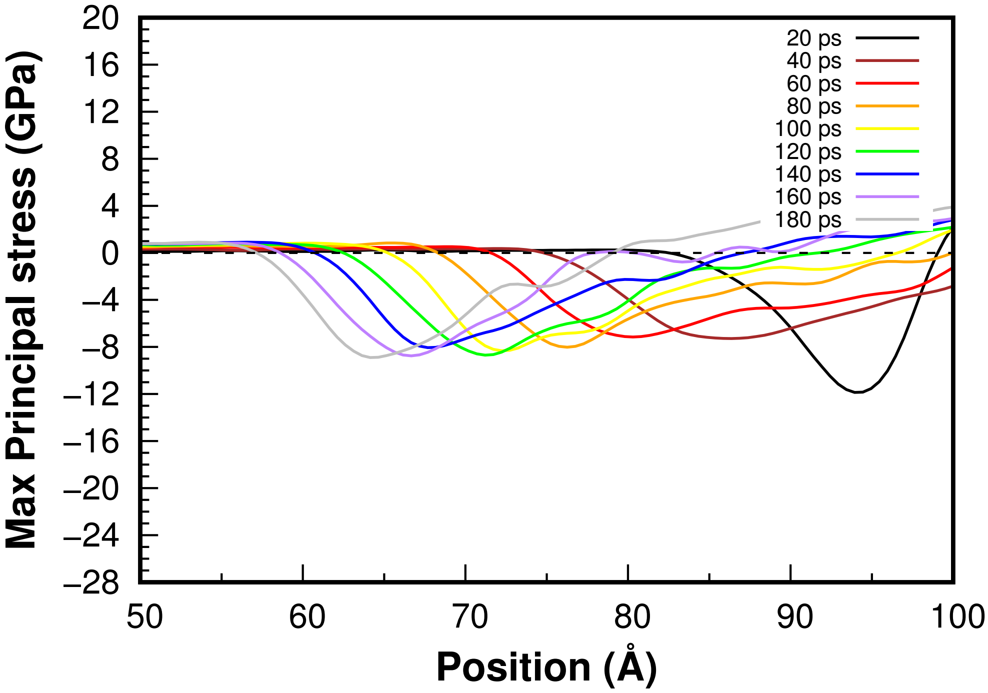

Figure 7.10 The Si(110) maximum principal stress in NVT 1200K

doi:10.6342/NTU201703940

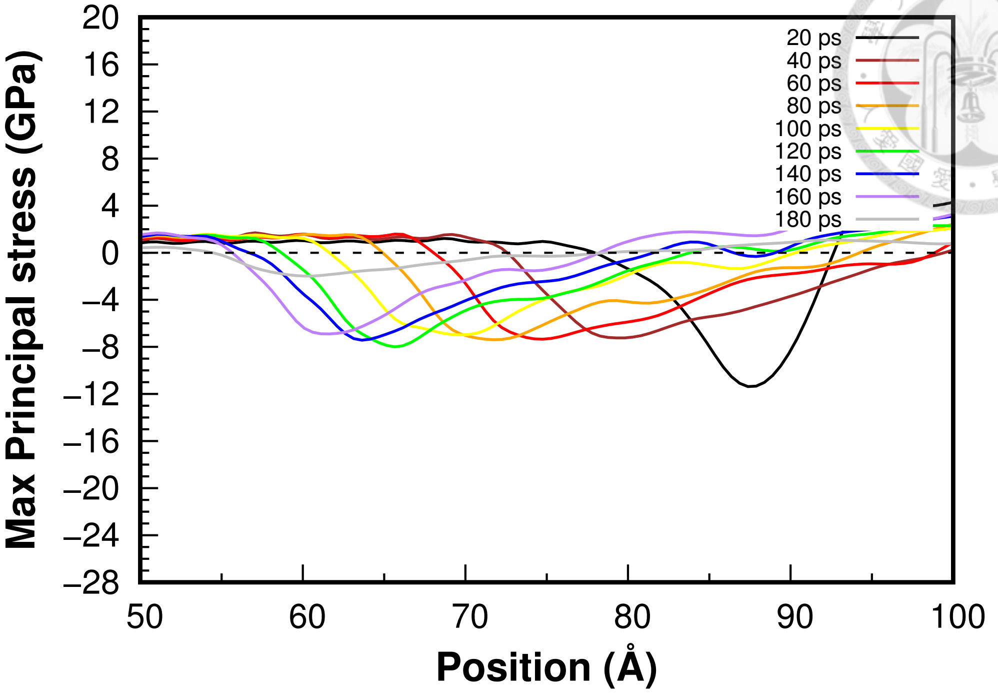

Figure 7.11 The Si(111) maximum principal stress in NVT 1200K

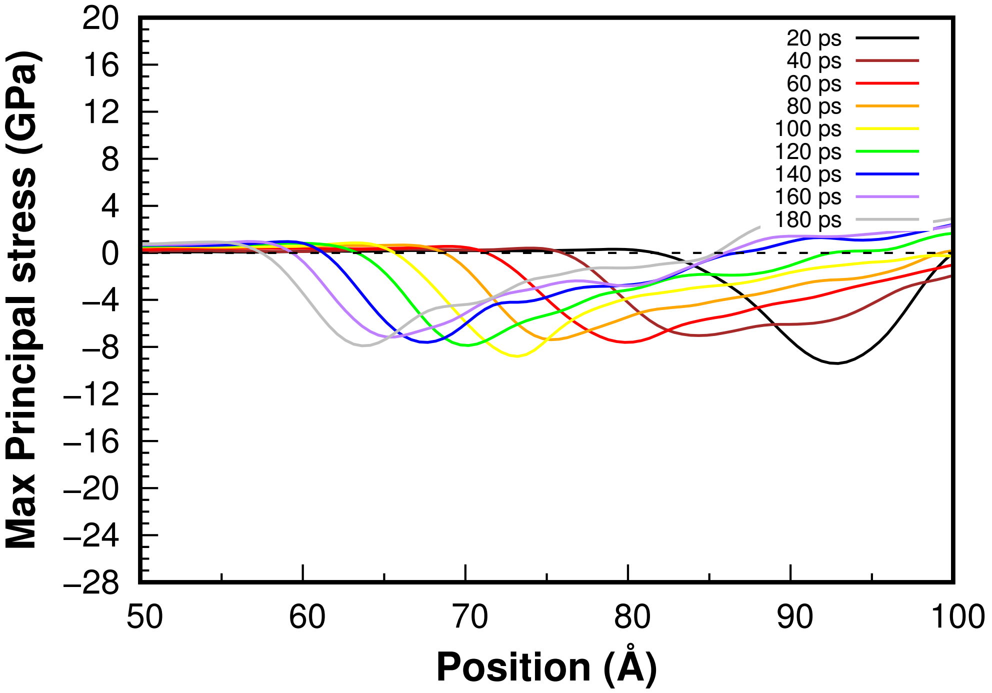

Figure 7.12 The Si(112) maximum principal stress in NVT 1200K

CHAPTER 8 References

1 Mizushima, K.; Jones, P.; Wiseman, P. and Goodenough, J. B. Lixcoo2 (0< x<-1): A new cathode material for batteries of high energy density. *Mater. Res. Bull.* **1980**, *15* (6), 783–789. doi:10.1016/0025-5408(80)90012-4.

2 Goodenough, J. B. and Park, K.-S. The li-ion rechargeable battery: A perspective. *J. Am. Chem. Soc.* **2013**, *135* (4), 1167–1176. doi:10.1021/ja3091438.

3 Liu, X. H.; Zhang, L. Q.; Zhong, L.; Liu, Y. and Zheng, H. *et al.* Ultrafast electrochemical lithiation of individual si nanowire anodes. *Nano Letters* **2011**, *11* (6), 2251–2258. doi:10.1021/nl200412p.

4 Chan, C. K.; Peng, H.; Liu, G.; McIlwrath, K. and Zhang, X. F. *et al.* High-performance lithium battery anodes using silicon nanowires. *Nat. Nanotechnol.* **2007**, *3* (1), 31–35. doi:10.1038/nnano.2007.411.

5 Liu, X. H.; Zheng, H.; Zhong, L.; Huang, S. and Karki, K. *et al.* Anisotropic swelling and fracture of silicon nanowires during lithiation. *Nano Lett.* **2011**, *11* (8), 3312–3318. doi:10.1021/nl201684d.

6 Lee, S. W.; McDowell, M. T.; Choi, J. W. and Cui, Y. Anomalous shape changes of silicon nanopillars by electrochemical lithiation. *Nano Lett.* **2011**, *11* (7), 3034–3039. doi:10.1021/nl201787r.

7 Liu, X. H.; Wang, J. W.; Huang, S.; Fan, F. and Huang, X. *et al.* In situ atomic-scale imaging of electrochemical lithiation in silicon. *Nat. Nanotechnol.* **2012**, *7* (11), 749–756. doi:10.1038/nnano.2012.170.

8 Chan, M. K. Y.; Wolverton, C. and Greeley, J. P. First principles simulations of the electrochemical lithiation and delithiation of faceted crystalline silicon. *J. Am. Chem. Soc.* **2012**, *134* (35), 14362–14374. doi:10.1021/ja301766z.

9 Jung, S. C.; Choi, J. W. and Han, Y.-K. Anisotropic volume expansion of crystalline silicon during electrochemical lithium insertion: An atomic level rationale. *Nano Lett.* **2012**, *12* (10), 5342–5347. doi:10.1021/nl3027197.

10 Cubuk, E. D.; Wang, W. L.; Zhao, K.; Vlassak, J. J. and Suo, Z. *et al.* Morphological evolution of si nanowires upon lithiation: A first-principles multiscale model. *Nano Lett.* **2013**, *13* (5), 2011–2015. doi:10.1021/nl400132q.

11 Rohrer, J.; Moradabadi, A.; Albe, K. and Kaghazchi, P. On the origin of anisotropic lithiation of silicon. *J. Power Sources* **2015**, *293*, 221–227. doi:10.1016/j.jpowsour.2015.05.057.

12 Kim, S.-P.; Datta, D. and Shenoy, V. B. Atomistic mechanisms of phase boundary evolution during initial lithiation of crystalline silicon. *J. Phys. Chem. C* **2014**, *118* (31), 17247–17253. doi:10.1021/jp502523t.

13 Jung, H.; Lee, M.; Yeo, B. C.; Lee, K.-R. and Han, S. S. Atomistic observation of the lithiation and delithiation behaviors of silicon nanowires using reactive molecular dynamics simulations. *J. Phys. Chem. C* **2015**, *119* (7), 3447–3455. doi:10.1021/jp5094756.

14 Ostadhossein, A.; Cubuk, E. D.; Tritsaris, G. A.; Kaxiras, E. and Zhang, S. *et al.* Stress effects on the initial lithiation of crystalline silicon nanowires: reactive molecular dynamics simulations using ReaxFF. *Phys. Chem. Chem. Phys.* **2015**, *17* (5), 3832–3840. doi:10.1039/c4cp05198j.

15 Ding, B.; Wu, H.; Xu, Z.; Li, X. and Gao, H. Stress effects on lithiation in silicon. *Nano Energy* **2017**, *38*, 486–493. doi:10.1016/j.nanoen.2017.06.021.

16 Kim, K. J. and Qi, Y. Vacancies in si can improve the concentration-dependent lithiation rate: Molecular dynamics studies of lithiation dynamics of si electrodes. *J. Phys. Chem. C* **2015**, *119* (43), 24265–24275. doi:10.1021/acs.jpcc.5b06953.

17 Swope, W. C.; Andersen, H. C.; Berens, P. H. and Wilson, K. R. A computer simulation method for the calculation of equilibrium constants for the formation of physical clusters of molecules: Application to small water clusters. *J. Chem. Phys.* **1982**, *76* (1), 637–649. doi:10.1063/1.442716.

18 van Duin, A. C. T.; Dasgupta, S.; Lorant, F. and Goddard, W. A. ReaxFF: a reactive force field for hydrocarbons. *J. Phys. Chem. A* **2001**, *105* (41), 9396–9409. doi:10.1021/jp004368u.

19 Chenoweth, K.; van Duin, A. C. T. and Goddard, W. A. ReaxFF reactive force field for molecular dynamics simulations of hydrocarbon oxidation. *J. Phys. Chem. A* **2008**, *112* (5), 1040–1053. doi:10.1021/jp709896w.

20 Plimpton, S. Fast parallel algorithms for short-range molecular dynamics. *J Comput Phys* **1995**, *117* (1), 1–19. doi:10.1006/jcph.1995.1039.

21 Aktulga, H. M.; Fogarty, J. C.; Pandit, S. A. and Grama, A. Y. Parallel reactive molecular dynamics: Numerical methods and algorithmic techniques. *Parallel Comput.* **2012**, *38* (4), 245–259. doi:10.1016/j.parco.2011.08.005.

22 Gale, J. D. GULP: A computer program for the symmetry-adapted simulation of solids. *J. Chem. Soc., Faraday Trans.* **1997**, *93* (4), 629–637. doi:10.1039/a606455h.

23 Gale, J. D.; Raiteri, P. and van Duin, A. C. T. A reactive force field for aqueous-calcium carbonate systems. *Phys. Chem. Chem. Phys.* **2011**, *13* (37), 16666. doi:10.1039/c1cp21034c.

24 van Duin, A. C. T.; Strachan, A.; Stewman, S.; Zhang, Q. and Xu, X. *et al.* ReaxFF-SiOReactive force field for silicon and silicon oxide systems. *J. Phys. Chem. A* **2003**, *107* (19), 3803–3811. doi:10.1021/jp0276303.

25 Rappe, A. K. and Goddard, W. A. Charge equilibration for molecular dynamics simulations. *The Journal of Physical Chemistry* **1991**, *95* (8), 3358–3363. doi:10.1021/j100161a070.

26 Ostadhossein, A.; Kim, S.-Y.; Cubuk, E. D.; Qi, Y. and van Duin, A. C. T. Atomic insight into the lithium storage and diffusion mechanism of SiO2/al2o3electrodes of lithium ion batteries: ReaxFF reactive force field modeling. *J. Phys. Chem. A* **2016**, *120* (13), 2114–2127. doi:10.1021/acs.jpca.5b11908.

27 Fan, F.; Huang, S.; Yang, H.; Raju, M. and Datta, D. *et al.* Mechanical properties of amorphous LixSi alloys: a reactive force field study. *Modell. Simul. Mater. Sci. Eng.* **2013**, *21* (7), 074002. doi:10.1088/0965-0393/21/7/074002.

28 Evers, J.; Oehlinger, G. and Sextl, G. A unique zintl phase - although stable, it long evaded synthesis.. *Chem. Inform.* **2010**, *29* (13), no–no. doi:10.1002/chin.199813026.

29 Wu, H.; Hartman, M. R.; Udovic, T. J.; Rush, J. J. and Zhou, W. *et al.* Structure of the novel ternary hydrides li4tt2d (tt= si and ge). *Acta Crystallographica Section B Structural Science* **2007**, *63* (1), 63–68. doi:10.1107/s0108768106046465.

30 Axel, H.; Schäfer, H. and Weiss, A. Zur kenntnis der phase li22si5. *Zeitschrift für Naturforschung B* **1966**, *21* (2). doi:10.1515/znb-1966-0204.

31 Zeilinger, M.; Baran, V.; van Wüllen, L.; Häussermann, U. and Fässler, T. F. Stabilizing the phase li15si4 through lithium–aluminum substitution in li15−xAlxSi4(0.4 <x< 0.8)–single crystal x-ray structure determination of li15si4and li14.37al0.63si4. *Chem. Mater.* **2013a**, *25* (20), 4113–4121. doi:10.1021/cm402721n.

32 Zeilinger, M.; Benson, D.; Häussermann, U. and Fässler, T. F. Single crystal growth and thermodynamic stability of li17si4. *Chem. Mater.* **2013b**, *25* (9), 1960–1967. doi:10.1021/cm400612k.

33 Chiang, H.-H.; Lu, J.-M. and Kuo, C.-L. First-principles study of the structural and dynamic properties of the liquid and amorphous li–si alloys. *The Journal of Chemical Physics* **2016**, *144* (3), 034502. doi:10.1063/1.4939716.

34 Hill, R. The elastic behaviour of a crystalline aggregate. *Proc. Phys. Soc. London, Sect. A* **1952**, *65* (5), 349–354. doi:10.1088/0370-1298/65/5/307.

35 Chevrier, V.; Zwanziger, J. and Dahn, J. First principles study of li–si crystalline phases: Charge transfer, electronic structure, and lattice vibrations. *Journal of Alloys and Compounds* **2010**, *496* (1-2), 25–36. doi:10.1016/j.jallcom.2010.01.142.

36 (2017). *CRC Handbook of Chemistry and Physics, 98th Edition*. Taylor & Francis Ltd..

37 Stillinger, F. H. and Weber, T. A. Computer simulation of local order in condensed phases of silicon. *Physical Review B* **1985**, *31* (8), 5262–5271. doi:10.1103/physrevb.31.5262.

38 Astrova, E. V.; Rumyantsev, A. M.; Li, G. V.; Nashchekin, A. V. and Kazantsev, D. Y. *et al.* Electrochemical lithiation of silicon with varied crystallographic orientation. *Semiconductors* **2016**, *50* (7), 963–969. doi:10.1134/s1063782616070022.

國立臺灣大學
敦品勵學・愛國愛人

doi:10.6342/NTU201703940